Technologies to Enhance Operation of the Existing Natural Gas Compression Infrastructure

Quarterly Technical Progress Report

Reporting Period Start Date: 01/01/04
Reporting Period End Date: 03/31/04

Principal Authors:

Anthony J. Smalley
Ralph E. Harris
Gary D. Bourn

March 2004

DOE Award No. DE-FC26-02NT41646
SwRI Project No. 18.06223

Submitting Organization:

Southwest Research Institute®
6220 Culebra Road
San Antonio, TX 78238-5166

DISCLAIMER

"This report was prepared as an account of work sponsored by an agency of the United States Government. Neither the United States Government nor any agency thereof, nor any of their employees, makes an warranty, express or implied, or assumes any legal liability or responsibility for the accuracy, completeness, or usefulness of any information, apparatus, product, or process disclosed, or represents that its use would not infringe privately owned rights. Reference herein to any specific commercial product, process, or service by trade name, trademark, manufacturer, or otherwise does not necessarily constitute or imply its endorsement, recommendation, or favoring by the United States Government or any agency thereof. The views and opinions of authors expressed herein do not necessarily state or reflect those of the United States Government or any agency thereof."

ABSTRACT

This report documents work performed in Phase I of the project entitled: *Technologies to Enhance Operation of the Existing Natural Gas Compression Infrastructure*. The project objective is to develop and substantiate methods for operating integral engine/compressors in gas pipeline service, which reduce fuel consumption, increase capacity, and enhance mechanical integrity. The report describes a number of potential enhancements to the existing natural gas compression infrastructure that have been identified and qualitatively demonstrated in tests on three different integral engine/compressors in natural gas transmission service.

TABLE OF CONTENTS

Page

TABLE OF CONTENTS *(CONTINUED)*

Page

LIST OF FIGURES

Page

LIST OF FIGURES *(CONTINUED)*

Page

LIST OF FIGURES *(CONTINUED)*

Page

LIST OF FIGURES *(CONTINUED)*

Page

LIST OF FIGURES *(CONTINUED)*

Page

LIST OF FIGURES *(CONTINUED)*

Page

LIST OF TABLES

Page

1. INTRODUCTION

This report presents a number of potential enhancements to the existing natural gas compression infrastructure that have been identified and quantitatively demonstrated in tests on three different integral engine compressors in natural gas transmission service.

The gas transmission industry operates over 4,000 integral engine compressors, which play a major role in pumping natural gas through the US pipeline system. Although the use of centrifugal compressors in the US pipeline industry has grown, these integral reciprocating units still represent over 70% of the fleet in numbers, and over half the installed power. These "slow-speed" integral engine compressors have been the workhorses of the industry for over 50 years, providing the reliable gas compression needed by the pipeline system. Figure 1 shows two such units: a 48-year old TLA6 and a 50-year old GMW10.

Figure 1. TLA6 (2000 HP) and GMW10 (2500 HP) in Pipeline Service

Figure 2 shows the age distribution of the current infrastructure. Over half the fleet is well over 40 years old, but replacing all these units with currently available technology would incur a huge cost and disruption to service with insufficient improvement in overall performance of the pipeline system to justify this cost and disruption. For these reasons, wholesale replacement remains unlikely (although selective replacement driven by factors such as environmental regulations can be expected). Growth to a 30-TCF-plus

gas market in the US, anticipated over the next 10 to 20 years, must come on the backs of the existing compression infrastructure; it will, therefore, depend on continued integrity, enhanced capacity, and efficiency of the existing integral engine/compressors under all loads. The industry needs demonstrated technology options and operating methods, which will cost-effectively maximize the capacity of these old units, and reduce their fuel consumption, while respecting or improving their integrity.

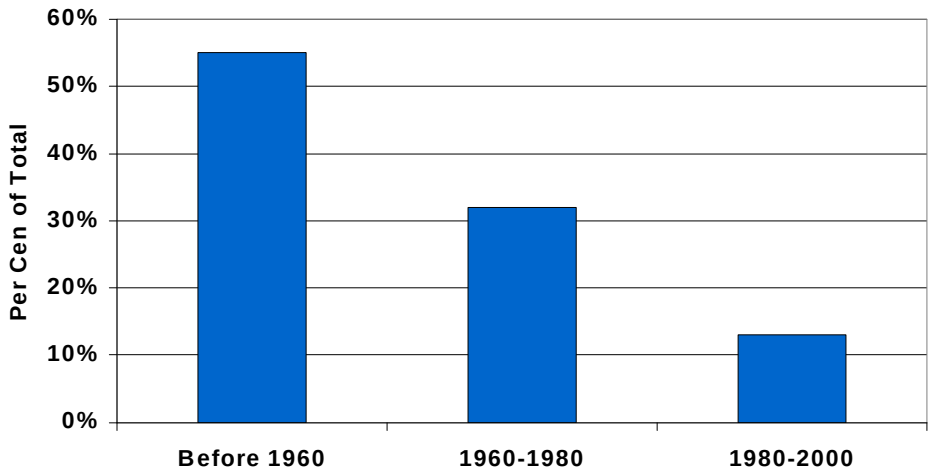

Figure 2. Install Dates: Over 50% of Pipeline Compressors Exceed 40 Years Old

Figures 3, 4, and 5 exemplify these needs of the existing infrastructure.

Figure 3 shows how annual fuel consumption at individual compressor stations in the pipeline system varies with the number of horsepower hours delivered by the engine to the compressor cylinders at that station. Points on the high side of the mean slope represent stations which are burning more than the industry average. In addition, with a regressed slope of 7.7 CF/BHP-hour for Figure 3, the industry burns significantly more fuel than the most efficient current technology natural gas engines (as little as 6 CF/BHP-hour). As a slightly different performance measure for the industry, Smalley et al [1] calculate an industry average (ratio of total fuel volume to total BHP-hours) of 8.25 SCF/BHP-hr.

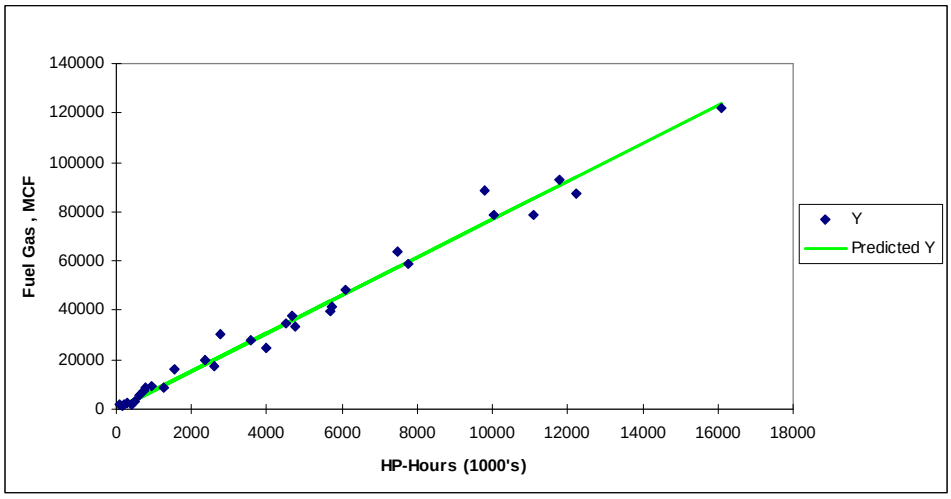

Figure 3. Industry Fuel Consumption
(~7.7 MCF/HP-Hr. +/-20% - Need to Lower the High Values)

Figure 4 presents a distribution of compressor thermal efficiency for the industry created by GMRC from a quantitative survey a number of years ago. This is the efficiency with which the compressors convert HP-hours to useful compression. The width of the range and the 12 points by which the 79% median lies below the best achieved (91 to 92%) represents not only gas which is burnt rather than delivered, but also engine capacity which must overcome losses rather than deliver useful compression of the transported gas.

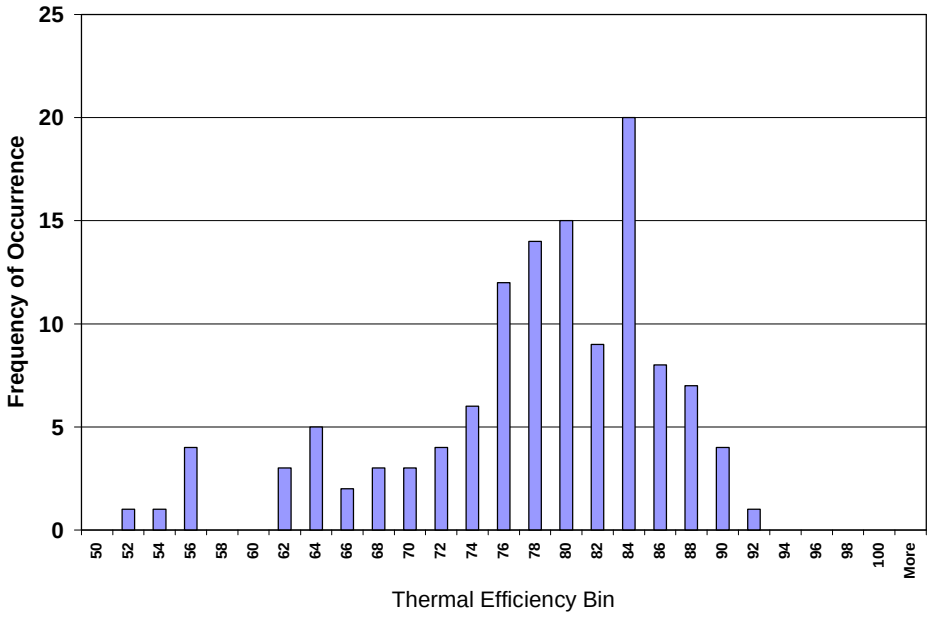

Figure 4. Compressor Thermal Efficiency Histogram based on GMRC Survey

Figure 5 shows a number of failed crankshafts. This problem continues to occur at an undesirable rate for the pipeline industry as a whole (about one failure per thousand engines per year). This rate may not seem excessive, but for the compressor station and company which incurs such a failure, the disruption, cost, and loss of capacity at the time is significant. The chance of this rate increasing as a penalty for improved performance and increased capacity must be avoided, as well as any increase in problems such as bearing failure, or damage caused by detonation, or unintended overload.

Figure 5. Integrity: Crankshaft Failure Examples – Need Methods of Avoidance

Three years ago, the US Department of Energy (DOE) initiated a Natural Gas Infrastructure (NGI) program, whose goals include increasing capacity of the current pipeline infrastructure (10%), and reducing operational costs (50% by 2010). As a part of this program, SwRI is undertaking a project entitled "Technologies to Enhance the Existing Natural Gas Compression Infrastructure". The project is managed for DOE by the National Energy Technology Laboratory (NETL). The project objective is:

To develop and substantiate methods for operating integral engine/compressors in gas pipeline service which reduce ***fuel consumption***, increase ***capacity***, and enhance mechanical ***integrity***.

To support this objective, SwRI has assembled a suite of instruments for measuring key performance parameters on these engine/compressors, and has integrated the data channels from these instruments into a powerful Data Acquisition System (DAS). On the widely accepted premise that effective improvement depends first on accurate measurement, the project has established the capability to concurrently measure and record a range of parameters (including cylinder pressure, fuel flow, torsional vibration, lateral vibration, crankshaft strain, manifold dynamic pressures, and global equivalence ratio). Using these measurement capabilities, the project has performed tests on a number of integral engine compressors. Data analysis capability has been added to provide operational measures such as efficiency of engine, compressor, and the system they form, cycle-to-cycle variance statistics, cylinder-to-cylinder variation in peak-firing pressure, and measures of crankshaft cumulative damage.

The general approach for the project has been to design a test program which links integrity, capacity, and efficiency to operation and balance; to acquire data by test on operational engine compressors; to analyze data and develop relationships; to apply these relationships and identify methods to optimize capacity and/or efficiency (subject to integrity constraints); and to evaluate optimization methods and benefits.

With this approach and the measurement capability described, the program has already accomplished the following:

- A new method of achieving balanced combustion across the cylinders has been invented and demonstrated.

- The need for improved cylinder-to-cylinder air balance has been documented. An investigation to accomplish this through control of manifold dynamic flow modulations has been proposed.

- The relationship between engine balance and crankshaft integrity has been shown.

- Knock detection capability has been evaluated and demonstrated as a means to allow more efficient engine operation, while protecting engine integrity.

- The use of closed-loop global air fuel ratio control has been identified and is to be evaluated as a means to maintain consistent engine operation as ambient and operating conditions change, subject to knock protection.

- The use of system efficiency to measure the conversion of fuel energy to useful compression of transported gas has been demonstrated and used to create benchmarks for the industry.

- Further benchmarks in component efficiency for engine and compressor have been documented.

- The relationship between system mechanical efficiency for transmission of engine power to compressor power and oil temperature has been quantified for two engines.

- High-pressure fuel injection, in combination with turbo-charging, has been shown to allow leaner operation and to achieve both lower heat rate, lower emission of NOx,

and to improve engine integrity by lowering crankshaft strain for a given compression power.

- Guidelines for achieving the benchmarks have been extracted from the data and its analysis.

- A means of directly monitoring and controlling compressor cylinder load by measurement of rod load variation has been tested and refined during the program. While still needing some final refinements, this technology has the potential to maintain the engine at its most efficient full load condition, while protecting against overload and the associated threat to integrity.

Based on these demonstrations, the project is bringing forward technology options that promise to increase capacity, and reduce operating costs in the following ways:

- Improving efficiency of power transmission, and of the compression process, makes more of the installed engine power available for useful compression.

- Enhancing integrity increases availability and capacity by avoiding forced downtime for maintenance.

- Enhancing integrity also reduces operating costs required for maintenance.

- Improving system efficiency reduces fuel consumption and associated fuel use costs, and makes more of the gas entering the pipeline system available to the end consumer.

Thus, project results are very consistent with DOE's goals of increasing capacity and reducing operating costs.

The tests and analyses have been performed so far on two different two-stroke engine models from two manufacturers: a Cooper GMW10 with three compressor cylinders, and a Dresser-Clark HBA-6T with four compressor cylinders. The HBA is a straight six with turbocharger. The GMW is a V-10, and has been tested both with and without the combination of a turbocharger and high-pressure fuel injection system. The engine selection was based on detailed quantitative analysis of the engine population using a database prepared for the pipeline industry, which shows both models are in the top six, measured by horsepower installed or by number of units installed. Thus, marked diversity has been achieved in the process of testing two widely deployed engine models.

2. EXPERIMENTAL

2.1 SENSORS AND DATA CHANNELS

Sensors and data acquisition capability have been assembled to record the following data on large integral engine compressors.

- *Dynamic Pressure in the Compressor Cylinders* – these measurements are used for compressor horsepower and flow determination. Both ends of each compressor cylinder have been instrumented for dynamic pressure in each test series. The sensors are Sensotec piezo-restrictive transducer). They are calibrated prior to each test by deadweight loading to generate known force per unit area in the test fluid applied to the sensing element.

- *Dynamic Pressure in the Engine Cylinders* – these measurements are used for engine horsepower determination, engine balancing, and to calculate engine statistics. All power cylinders have been instrumented for dynamic pressure in each test series. The sensors are Kistler quartz piezoelectric transducers. Being dynamic sensors, they are calibrated prior to each test by suddenly applied deadweight loading to generate known force per unit area in the test fluid applied to the sensing element.

- *Dynamic Pressure in the Engine Air Intake Manifold* – these measurements are used to correlate dynamic effects in the manifolds, which deliver air for each cylinder with the dynamic statistics within each cylinder. They also provide the time-averaged value for air manifold pressure whose influence on engine heat rate and emissions is assessed. Air manifolds have been instrumented in each test series. The sensors are Kistler piezo-resistive pressure transducers with factory provided calibration.

- *Dynamic Pressure in Engine Exhaust* – these measurements are used to determine dynamic variation of pressure in the manifolds, which capture hot exhaust gas from each cylinder, and to correlate these dynamic pressure variations with the dynamics

within each cylinder. The sensors are Kistler piezo-resistive transducer with factory provided calibration; they are water-cooled to reduce uncertainty resulting from temperature influence on the sensor readings.

- *Torsional Vibrations (IRV)* – This measures the dynamic variation in speed of rotation of the flywheel. The sensor is a BEI 512 pulse encoder driven through a flexible coupling by a shaft connected by a friction drive to the flywheel. The frequency of its output pulse train directly reflects instantaneous flywheel angular velocity, which varies within each cycle of the engine as a result of dynamic load variation. Rather than digitally time the variation in period between pulses (which imposes unrealistic period discrimination requirements), a frequency to voltage analog circuit is used to determine the continuous variation in flywheel speed. The speed variation is assessed as a surrogate for mechanical integrity. The frequency-to-voltage measurement is calibrated by supplying the analog circuitry with a pulse train of known frequency from a signal generator. The torsional vibration has been measured in this way on all tests. The torsional vibration data has been assessed as a potential indicator of engine dynamic loading severity.

- *Data Acquisition Triggering* – The BEI encoder signal is also used to trigger acquisition of samples from all dynamic transducers. The phasing of the pulse train to top dead center is important. A pre-established top dead center mark for power cylinder #1 is used as a reference, and the angular setting within the DAS corresponding to cylinder #1 TDC is adjusted, as the engine runs, until a strobe light triggered by the DAS at this angle shows the mark on the flywheel coincides with the stationary mark.

- *Bearing Centerline Vibration* – This measurement is assessed as an indicator of engine dynamic loading severity. The sensors are PCB velocimeters with factory provided calibration. The sensors have been located to measure lateral vibration at each end of the engine/compressor frame.

- *Crankshaft Dynamic Strain* – This measurement is used as a direct indicator of shaft loading, and to provide a link between engine statistical quantities and potential for crankshaft fatigue damage [2]. The strain gage is placed on the crankshaft web as close as possible to the crank pin – at the point most sensitive to opening and closing of the crank throw faces under load from engine and compressor rods. Data is acquired by the Strain Data Capture Module (SDCM), which rides on the shaft within the engine during each day of testing, and from which data is downloaded at the end of each day. This is calibrated using a calibration resistance. The SDCM has worked with complete reliability for all tests so far.

- *Engine Fuel Flow* – Used to document overall engine efficiency. The sensor is an Emerson Flobas 103 transmitter which implements the AGA3 flow measurement based on a differential pressure measurement, and is factory calibrated with a certificate. This sensor is connected to taps on the already installed engine fuel flow orifice, which has been available on all engines tested so far. The fuel flow, coupled with a gas analysis, provides the basis for determining fuel energy consumed by the engine, and for determining heat rate and overall system efficiency. At the first test, the flow measurement functioned, but the flow range was not properly matched to the engine, and satisfactory data was not obtained. At subsequent tests, the fuel flow has been successfully measured and used for the intended purposes.

- *Suction Header and Discharge Header Pressures and Temperatures* – These measurements are used for installation efficiency determination. Pressures are measured with Sensotec piezo-restrictive transducers.

- *Engine Exhaust O_2 Level* – This measurement is used to determine global equivalence ratio, both as an independent variable influencing engine performance, and where the loop is closed to the turbocharger waste-gate for active control. The sensor used is an NGK fast-response transducer, which provides a continuous variation of voltage with exhaust oxygen level. It is calibrated against a standard.

- *Engine Exhaust NOx Level* – This measurement is used to provide comparative emissions data. The sensor used is an NGK fast-response transducer, which provides a continuous variation of voltage with exhaust NOx level. It is calibrated against a standard.

- *Compressor Rod Load* – This measurement is used for both mechanical integrity and loading optimization. The sensor uses a pair of strain gages mounted on either side of the rod, which are bridged additively to cancel bending and produce a signal proportional to axial load on the piston rod. The signal is transmitted using RF from a moving antenna to a stationary antenna. The strain gage and signal transmission can be powered by a battery, or by a generator driven by rod motion. The battery power is adequate and simpler to set up for short term tests, but for continuous monitoring and control self-powering is needed. Calibration issues are not fully resolved yet for this device (termed the "rod load monitor" (RLM)). So far, the horsepower measurement from the compressor cylinder, based on cylinder pressure transducer, has been used for calibration.

3. DATA ACQUISITION

Figures 6 and 7 show photographs of the Data Acquisition System (DAS). The system comprises an industrially hardened computer, a flat screen for display, and a separate box with connectors to which cables from individual sensors are connected. The DAS box has analog-to-digital converters of appropriate speed for over 50 different channels.

Figure 6. Front View of Data Acquisition System (DAS)

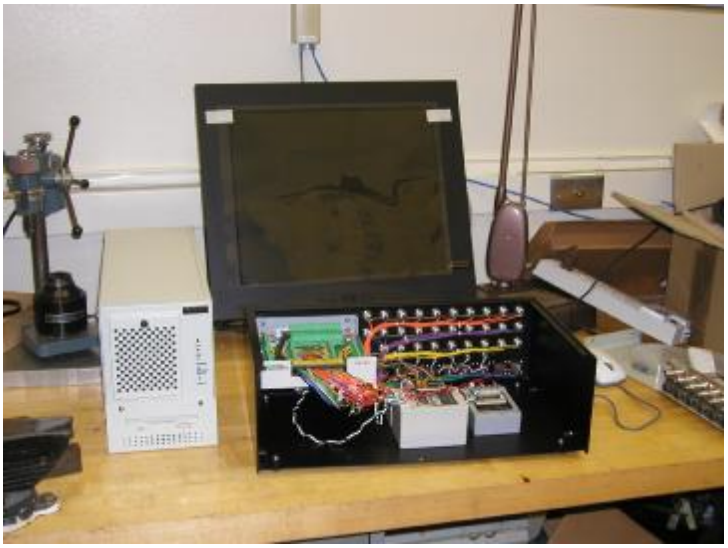

Figure 7. Rear View of Data Acquisition System (DAS)

The individual power cylinder transducers (up to 10) are connected to a box with connectors on the deck near the cylinders. A single cable from this box carries the signals from all the power cylinder transducers to the main data acquisition box. A similar approach is used for the compressor cylinders. In this way, the complexity of the cabling and system checkout is minimized. Signals from rod load monitors, from other system pressures, and from temperature sensors are acquired by the DAS, concurrently, and a database of the sensor values throughout each test is created by the DAS.

3.1 TRANSDUCER INSTALLATION

Figure 8 shows a compressor cylinder with pressure transducers installed on head and crank end. As discussed above, these are Sensotec piezo-resistive sensors.

Figure 8. Compressor Cylinder and Pressure Transducers on each End

Figure 9 shows the details of the power cylinder pressure transducer installation on one cylinder of the first GMW10 tested. Close examination reveals two pressure transducers installed – the one nearest the cylinder was already installed at test time as part of the high-pressure fuel injection system; the one further removed from the cylinder provided the data for SwRI's test on the engine with high-pressure fuel. This separation and associated effects with loss of information in the measurement channel leads to some uncertainty in the measurement of power cylinder pressure for this test.

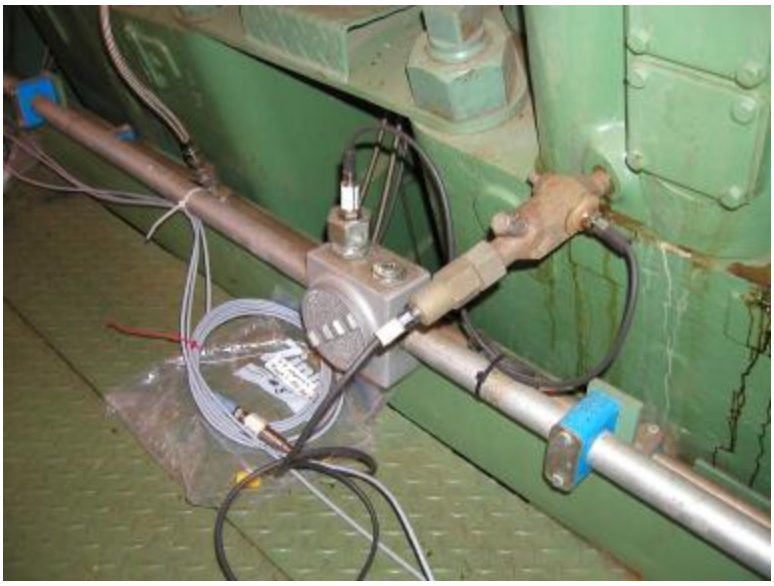

Figure 9. Details of Power Cylinder Pressure Transducer Installation

Figure 10 shows the unit tested at El Paso's Station 823. Close examination reveals the pressure transducer located in its air manifold. Figure 11 shows rather more clearly the pressure transducer in the air manifold for the GMW10 with high-pressure fuel injection.

Figure 10. Initial Site Test
(HBA-6T, TGP Kinder Station)

Figure 11. Pressure Transducer in Air Intake Manifold (GMW10, Williams Sour Lake Station)

Figure 12 shows the pressure transducer in the exhaust manifold of the GMW10 at Williams' Station 40. Close examination also shows the tubes carrying cooling water to the transducer.

Figure 12. Pressure Transducer in Exhaust Manifold (GMW10, Williams Sour Lake Station)

Figures 13 and 14 show an overview and close-up of the installation for the encoder. As discussed above, the encoder provides the multiple functions of torsional vibration measurement and triggering of data acquisition for all dynamic channels. The bracket holding the encoder is mounted on the tripod shown in Figure 13, and the shaft connecting the encoder to the flywheel is also apparent in both figures. The cable evident in these figures connects the encoder to the DAS.

Figure 13. Encoder, Outboard of Flywheel on Mounting Tripod (GMW10, Williams Sour Lake Station)

Figure 14. Detailed View of Encoder and Connection to Flywheel (GMW10, Williams Sour Lake Station)

Figure 15 shows one of the velocity probes mounted on the back of the compressor to measure lateral vibration of the frame; there are two such installations, one at each end of the compressor.

Figure 15. Accelerometer Mounted on Frame (GMW10, Williams Sour Lake Station)

Figure 16 shows an installation of the crankshaft Strain Data Capture Module (SDCM). The data acquisition system dedicated to one channel of crankshaft strain is seen in this figure mounted on the unstressed flat part of the crank throw. The lead from the strain gage is seen attached to the face of the crank web. The strain gage itself is hidden by the rod, since it is pushed so far up into the space between rod and web face. As previously described, the strain gage, cable, and single channel data acquisition system represent a standalone system with battery power which captures data unattended throughput a day of testing.

Figure 16. Strain Data Capture Module Installed (GMW10, Williams Sour Lake Station)

Figure 17 shows the SDCM installed on two throws at the Kinder Station (El Paso Station 823) – one throw with power rod only connected, and one throw with both power and compressor cylinders attached.

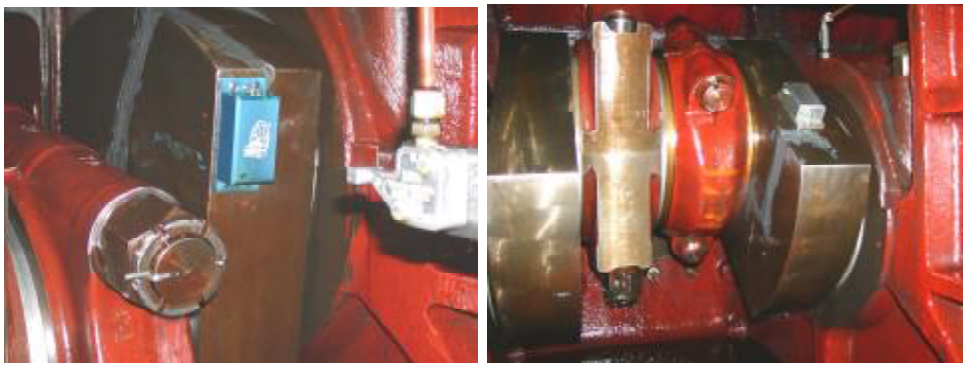

Throw 3
(Power & Compressor)

Throw 2
(Power Only)

Figure 17. SDCM Installation for Crankshaft Strain Measurements (HBA-6T, El Paso Kinder Station)

Figure 18 shows the flow transmitter connected to the orifice taps in the fuel flow gas flow line.

Figure 18. Flow Transmitter Connections to Orifice in Fuel Gas Line (GMW10, Williams Sour Lake Station)

Figure 19 shows the NGK combined O_2/NOx sensor connected to a pipe already installed, which connects to the exhaust stack.

Figure 19. O_2/NOx Sensor and Connection to Line from Stack (GMW10, Williams Sour Lake Station)

Figure 20 shows installations of the rod load monitor on the HBA-6T tested, and on the GMW10. These installations are visible with the "dog-house" cover removed for installation. Once the installation is checked out and the cover re-installed, Figure 21 shows that only the antenna connection remains visible. The antenna connection is then cabled to the DAS. Both installations photographed show the rod load monitor in a battery powered version, which is satisfactory for short term testing. As a device for long term monitoring, however, the rod load monitor must be self-powered. Figure 22 shows the self-powered Rod Load Monitor (RLM) configured specifically for an HBA-6T crosshead, which has been assembled for the follow-up test at El Paso Station 823 (Kinder Louisiana).

For the first test at TGP's Kinder, Louisiana station (April 15-17, 2003), the majority of these channels were successfully acquired as a coherent data set for every test condition. All channels were calibrated prior to the tests. In addition to the channels listed above, a portable emissions analyzer (an ECOM A+) was used to measure concentration of NO, NO_2, NOx, O_2, and CO in the exhaust.

Figure 20. Installations of the RLM on HBA-6T and GMW10

Figure 21. Cable from RLM Antenna (GMW10, Williams Sour Lake Station)

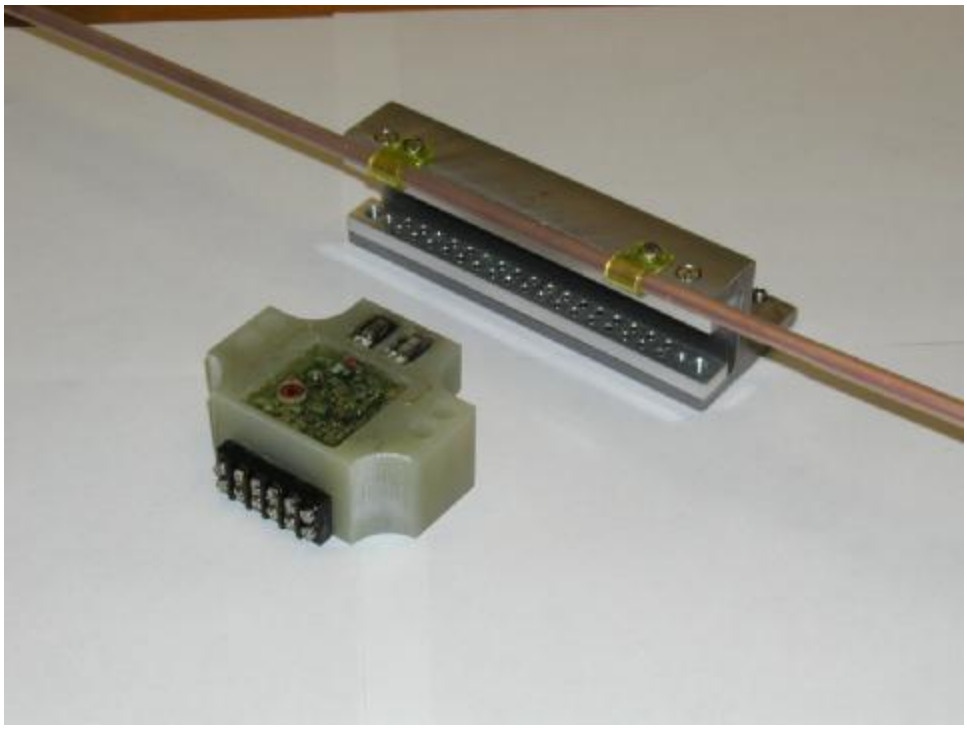

Figure 22. Self-Powered Rod Load Monitor (RLM)

However, a few of the channels listed above gave problems at the first site. The engine fuel flow meter was calibrated prior to the test, but it was discovered during the test that it was set for a much higher flow rate than was needed, and did not give useful data. The rod load monitor RF transmitter drifted too much. This is a development device and the underlying problem has now been corrected. The power cylinder #1 pressure transducer gave suspect data, and this has proved more elusive than expected! The problem has finally been traced to an artifact of the data acquisition circuitry. The multiplexor was found to inject a charge, which most strongly influenced the power cylinder #1 channel. Addition of a unity gain isolation amplifier was found to correct the problem.

At the second test site (Transco Station 40, Sour Lake, Texas, August 26-28, 2003), the fuel flow was successfully measured throughout the test series, and the problems obtained with fuel flow measurement at the first site should not reoccur. The rod load monitor worked successfully, although as subsequent results will show, a small amount of temperature drift was still encountered at the second test site. Exhaust manifold

dynamic pressure was acquired, as well as air manifold pressure. Station records were used for suction and discharge pressure and temperature for the compressor.

3.2 SELECTION OF TEST ENGINE MODELS

The two engines tested in Phase I have been an HBA-6T and a GMW10. Data to guide this selection was obtained from an industry database of engines and compressors in gas transmission service, supported by PRCI. Tables 1 and 2 were obtained by appropriate sorting of the database to show the top 10 engine models in terms of number installed (Table 1), and in terms of horsepower installed (Table 2). It may be seen that the GMW has the highest count (336) and the second highest installed power (708,336 HP). The HBA is in the top six for both count (6^{th} with 223) and installed power (5^{th} with 372,414 HP). Thus, these two engines rank highly in terms of pipeline industry deployment. They also achieve diversity; one is made by Cooper, and one by Clark; one is a straight six and one is a V-10. The HBA-6T is turbocharged; two different GMW units have been tested – one has a turbocharger and high-pressure fuel injection; the other has no turbocharger and standard fuel pressure.

Table 1. High Count Engines in Gas Transmission – Sorted by Number
(from 1998 Coerr Database)

Model	Sum of Rated HP	Count	Cumulative			Comments
GMW	708336	336	336	Top 6 by HP or #	Top 10 by HP or #	Just GMW - No GMWA, GMWC
KVG	330918	296	632		Top 10 by HP or #	
TLA	672085	280	912	Top 6 by HP or #	Top 10 by HP or #	
GMV	270489	269	1181		Top 10 by HP or #	Just GMV - No GMVB, GMVH
KVS	441455	233	1414	Top 6 by HP or #	Top 10 by HP or #	
HBA	372414	223	1637	Top 6 by HP or #	Top 10 by HP or #	
GMVH	302242	179	1816		Top 10 by HP or #	
TCV	872106	155	1971		Top 10 by HP or #	Includes TCV Thru TCVD
L-7042	154528	150	2121			Small High-Speed Waukesha
BA	207271	140	2261			Old & Small

Table 2. High Count Engines in Gas Transmission – Sorted by Horsepower
(from 1998 Coerr Database)

Model	Sum of Rated HP	Count	Cumulative HP			Comments
TCV	872106	155	872106		Top 10 by HP or #	High HP
GMW	708336	336	1580442	Top 6 by HP or #	Top 10 by HP or #	
TLA	672085	280	2252527	Top 6 by HP or #	Top 10 by HP or #	
KVS	441455	233	2693982	Top 6 by HP or #	Top 10 by HP or #	
HBA	372414	223	3066396	Top 6 by HP or #	Top 10 by HP or #	
V-250	335450	93	3401846			
KVG	330918	296	3732764		Top 10 by HP or #	
W-330	315656	56	4048420			High HP, Recent
GMVH	302242	179	4350662		Top 10 by HP or #	
GMV	270489	269	4621151		Top 10 by HP or #	
Note: If we total all GMW, GMWA, through GMWS, we get 1,189,736 HP and 511 units.						

4. RESULTS AND DISCUSSION

4.1 TYPICAL DATA FROM THE FIRST TEST ON AN HBA-6T

Figure 10 has already shown the HBA-6T tested at El Paso's Station 823 (Kinder, Louisiana). The next nine figures are initial data for the HBA-6T tests and some preliminary data summaries or expressions are presented. These are followed by focused analyses aimed at developing relationships from the data.

Figure 23 shows a sample of pressure data from both the power cylinders (on the left of the figure) and from the compressor cylinders (on the right). There are six traces in the power cylinder plot, but the cylinder #1 pressure transducer was suspect. These traces are averaged over 32 cycles. Even when discounting the possibly suspect trace of cylinder #1, the spread between highest and lowest peak pressure is clear. The PFP spread in this example is 190 PSI (1.3 Mpa). This plot simply presents representative data at some stages in the test program and represents neither highest nor lowest spread. Though not shown by this figure, the cycle-to-cycle variation for any cylinder is also significant for this two-stroke engine. Because cylinder pressure varies with time and across cylinders, it is important to distinguish how spread is expressed. Subsequent report sections will refer to the "average instantaneous spread," which is the difference between the maximum and minimum peak-firing pressure across the cylinders in one engine revolution averaged over many cycles. These sections will also refer to the average peak-firing pressure spread, which is the difference between maximum and minimum pressure as shown by the time averaged pressure in each cylinder.

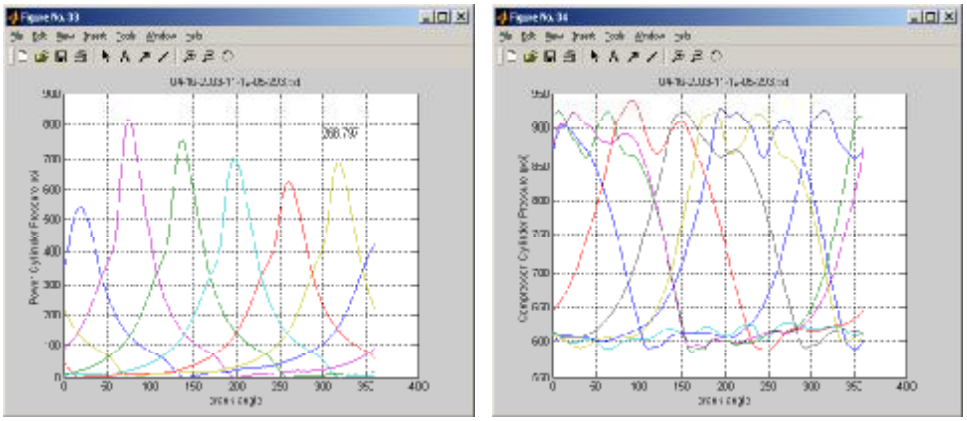

Power Cylinder Pressures Compressor Cylinder Pressures

Figure 23. Typical Data Sets – HBA-6T – Test #1

The compressor cylinders exhibit less spread between highest and lowest peak pressure. This is, in part, because discharge pressure pegs the highest cylinder pressure quite closely, and possibly because closer attention is paid to control of compressed gas acoustic pulsations outside the compressor cylinders than to air pulsations outside the power cylinders. Close examination shows seven compressor traces – this represents head and crank end from three cylinders and head end only for one cylinder. The crank end of one cylinder was deactivated, which is one convenient means of capacity control.

Further typical data is shown in Figure 24. Here, we see the inlet air manifold pressure (on the left) and the crankshaft rotational velocity (on the right). Both these quantities are presented in the upper frames as the variation with crank angle from zero to 360 degrees, and in the lower frame as a spectrum showing variation with engine order from one to one hundred. The inlet air manifold pressure clearly varies quite widely over one revolution (1.8 PSI or 12.4 Kpa peak-to-peak variation out of about 7.8 PSI or 53.8 Kpa). The spectrum shows significant content out to at least the 13th order. This specific measurement was taken at the flywheel end of the air manifold (as shown in Figure 10).

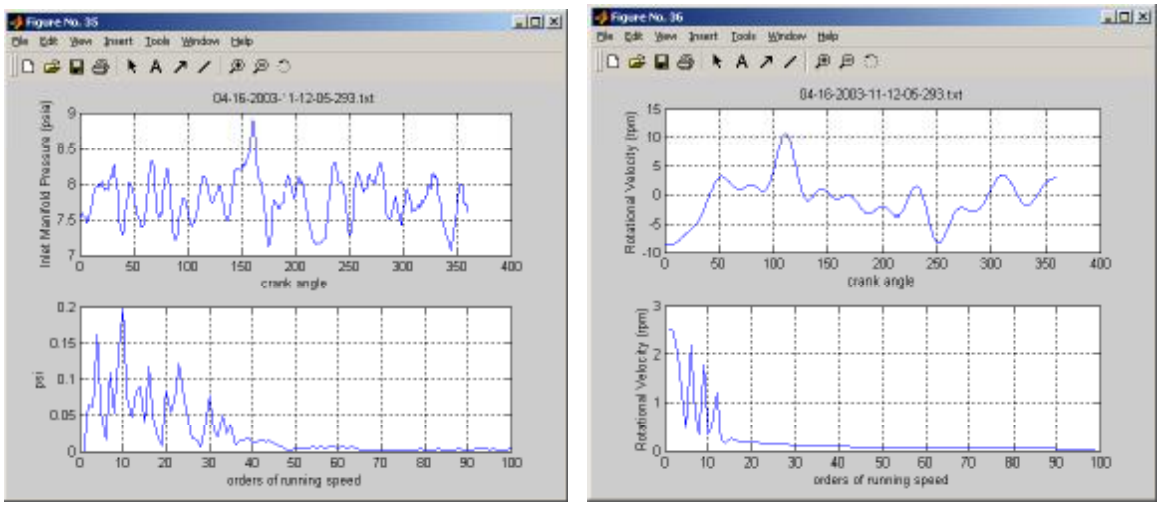

Inlet Air Manifold Pressure Rotational Velocity

Figure 24. Typical AMP and IRV Data Sets – HBA-6T - Test #1

The crankshaft velocity varies in one revolution by over 18 RPM peak-to-peak out of an average of about 300 RPM (6% variation). The spectral content of this variation is mainly concentrated in the first 12 orders.

Figure 25 presents further quantification of air manifold pressure (AMP or MAP) variation over 36 successive data sets acquired with different engine balance conditions. The average peak-to-peak variation is about 25% of the average, and it ranges from 22.6% to 26.9%. This AMP variation could be a significant contributor to imbalance or spread between cylinders, as will be subsequently discussed.

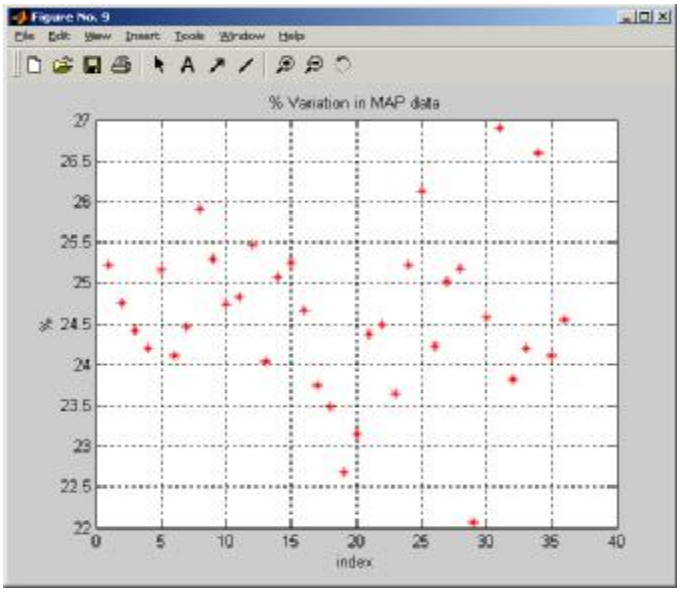

Figure 25. AMP Variation Summary – HBA-6T – Test #1

Figure 26 shows compressor Differential Indicated Power (DIP) for head and crank ends of the compressor in percent of indicated power. DIP is a measure of the cylinder power lost to flow resistance; thus, low DIP leads to high thermal efficiency, and based on these DIP values between 3.5 and 5.5%, the efficiency would be expected to be high.

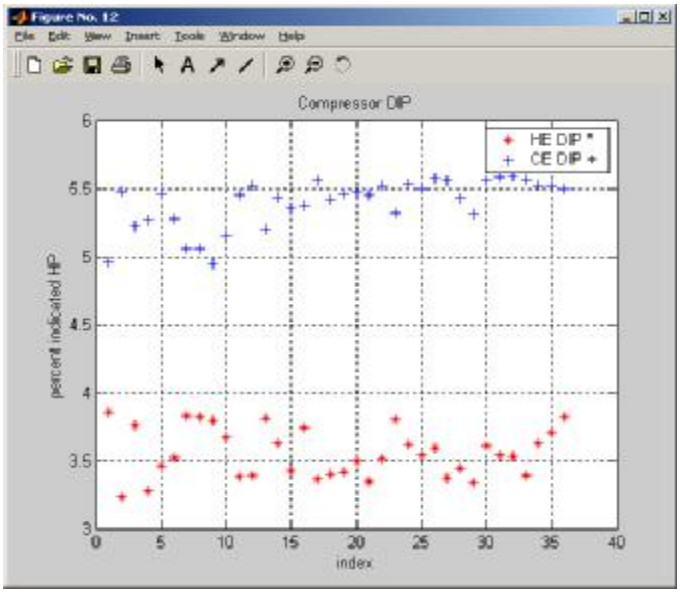

Figure 26. Compressor Performance Data – HBA-6T – Test #1
(Head and Crank End DIP)

Figure 27 confirms – efficiencies across 36 data sets range from a low of 90.7% to a high of 91.5%. A compressor thermal efficiency survey conducted by SwRI for GMRC a few years ago, based on measured enthalpy rise, showed that 91 or 92% was about the best achieved on any pipeline industry compressor. The median thermal efficiency for the pipeline industry, based on this survey, was about 79%.

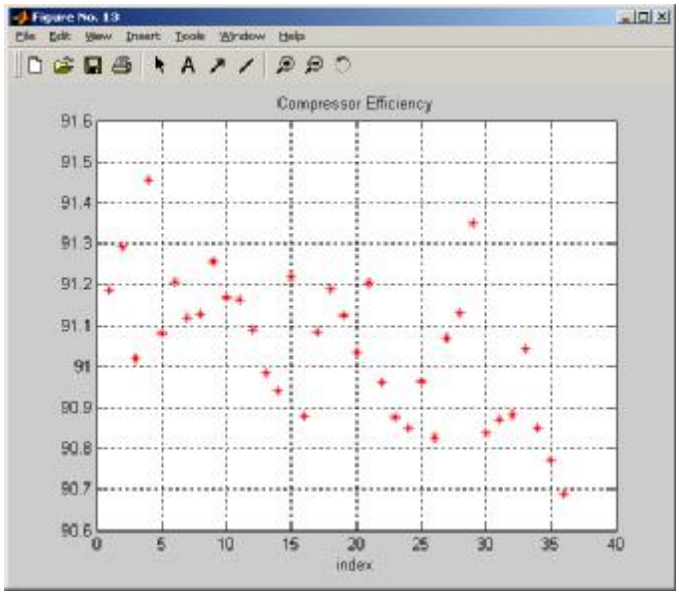

Figure 27. Compressor Efficiency Data – HBA-6T – Test #1

Thus, based on the cylinder pressure data and differential power, the compressor tested is operating at a high percentile efficiency for the industry. This is a significant, positive result for several reasons: 1) it represents efficient use of fuel gas; 2) it helps lower the ratio of emissions to useful compression power; 3) it leads to high available capacity; if at any time a compressor's capacity is limited because the load on the engine is at the safe limit for that engine, then any losses in the compressor represent engine capacity, which is unavailable as useful energy to be imparted to the transported gas. This compressor has maximized the engine capacity available for gas energy. The result is significant also because it sets a benchmark for the industry; if all compressors could consistently reach this level of compressor efficiency, a significant increase in industry-wide capacity would be achieved.

Figure 28 shows typical waveforms of crankshaft dynamic strain from the strain data capture module– one from a crank throw with both power and compressor cylinders acting on its crank pin, and one from a crank throw with only a power cylinder acting on its crank pin. Figure 17 has shown how the SDCM was installed on these two throws. The two second data snapshots in this figure cover about 10 revolutions and show significant differences, by almost a factor of two in the magnitude of the peak-to-peak variation for the throw with both power and compressor rods attached when compared to the throw with power rod only. This represents significant nonuniformity along the crankshaft in the potential for fatigue damage as the crankshaft transmits power to the compressor cylinders.

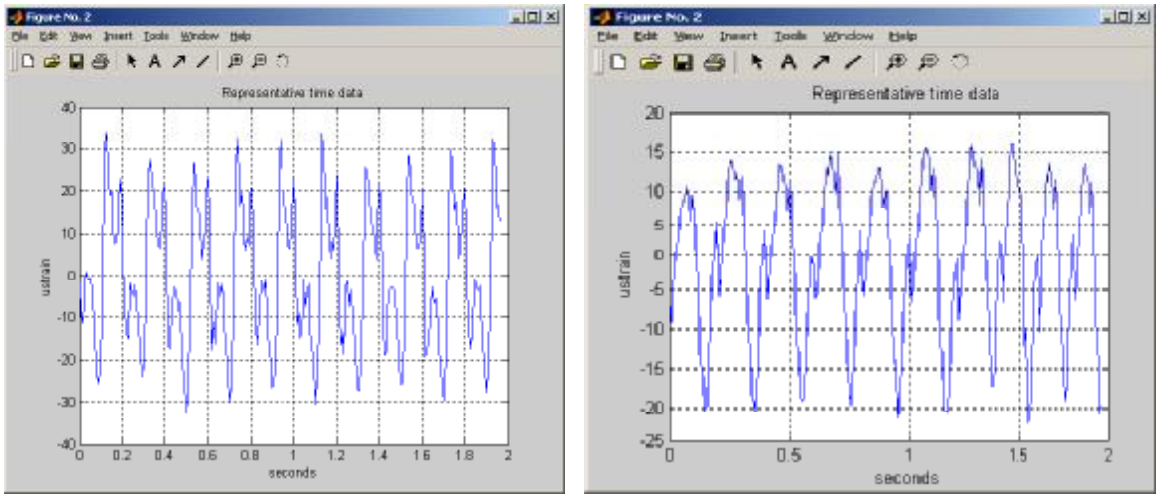

Throw 3 (Power & Compressor)

Throw 2 (Power Only)

Figure 28. Typical SDCM Waveform – HBA-6T – Test #1

Figure 29 shows the variation in peak-to-peak microstrain from the SDCMs on the same two throws over a 10-hour test period. Here, a further difference between the power and compressor throw and the power only throw becomes apparent – the throw which drives a compressor throw directly, experiences pronounced spikes in the strain, which differ in magnitude from the normal variation. The throw, which carries a power cylinder connecting rod, does not exhibit such distinct "spikiness".

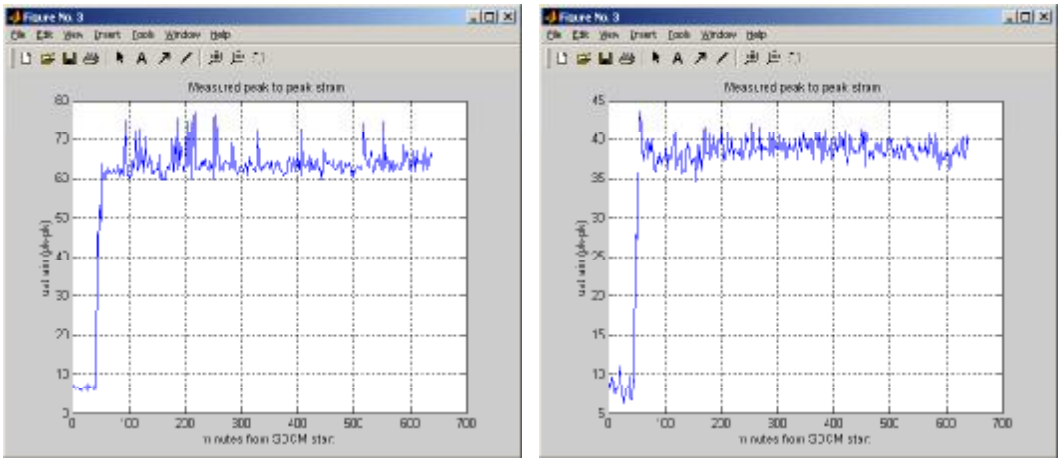

Throw 3
(Power & Compressor)

Throw 2
(Power Only)

Figure 29. Overall Peak-to-Peak Strain Summary – HBA-6T – Test #1

Figure 30 shows the variation in strain spectra (first to eighth orders) from these two throws over the period of the test. Of primary interest, here, is the higher relative magnitude of second and third orders in the strain from the combination throw as opposed to the power only throw.

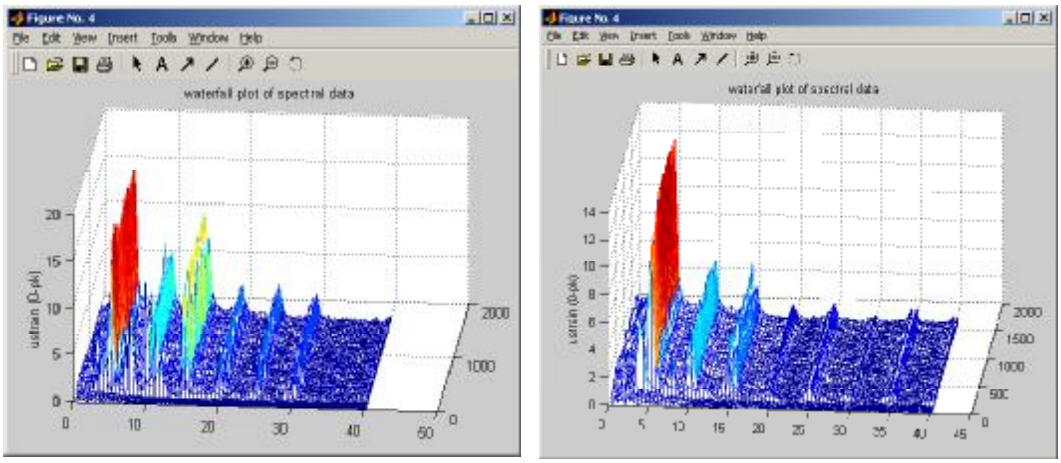

Throw 3
(Power & Compressor)

Throw 2
(Power Only)

Figure 30. Raster Plots of SDCM Data – HBA-6T – Test #1

Figure 31 compares the first eight orders in the strain spectra from these two throws over the period of the test. Again, this figure shows higher relative magnitude of second and third orders in the strain from the combination throw when compared to the power only throw.

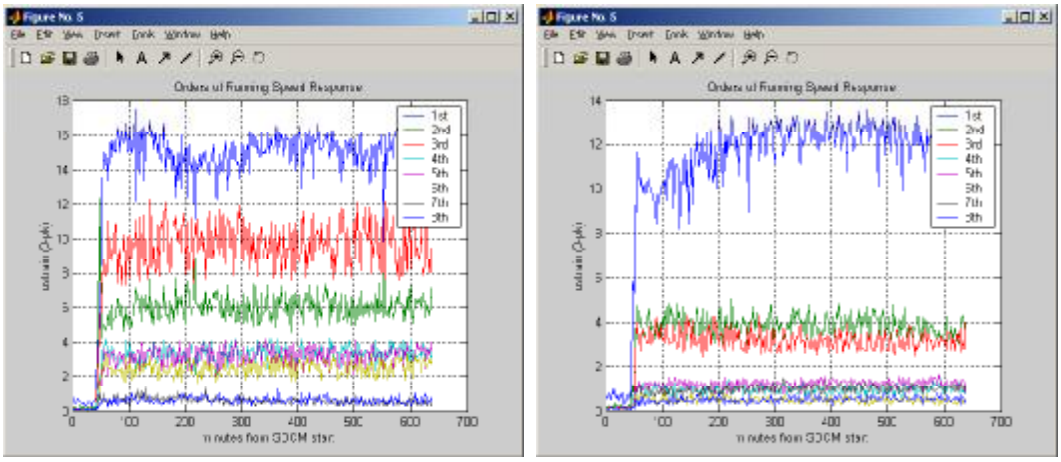

Throw 3
(Power & Compressor)

Throw 2
(Power Only)

Figure 31. Order Summary of SDCM Data – HBA-6T – Test #1

4.2 SUPPLEMENTARY ANALYSIS OF DATA FROM HBA-6T, TEST #1

4.2.1 Relating Crankshaft Strain Characteristics to Life

The significance of crankshaft strain variation is difficult to define on an absolute basis, because laboratory fatigue data does not exist for crankshaft materials out anywhere close to the number of cycles to which a crankshaft is exposed over its lifetime (over 4.5×10^9 revolutions for a 250,000-hr. crankshaft). In essence, the long life crankshafts are the fatigue testers! The simple assumption in classical fatigue analysis is that an endurance limit exists – according to this assumption, if dynamic strains are below the endurance limit, then the component in question will last forever. Data makes it clear for most materials that the variation of cyclic stress amplitude with cycles to failure at that amplitude (the SN diagram) becomes flatter when the number of cycles exceeds about 10^7, but whether it is truly flat or just has a gradual slope is not so clear. One explanation

for the observed fact that some high hour crankshafts eventually fail is the existence of a gradual slope in the SN diagram. If an endurance limit existed, the crankshaft should not fail unless the loads it experiences have changed, or it has accumulated damage from occasional loads substantially higher than it sees under normal operation.

To calculate possible life implications of the measured strain data, Figure 32 shows histograms of stress level for the two measured throws. These histograms give the frequency of occurrence, using a method called "rainflow counting" of different strain ranges in a two-second sample. The power/compressor combination throw clearly produces several stress cycles at nearly twice the highest stress level compared to the power only throw.

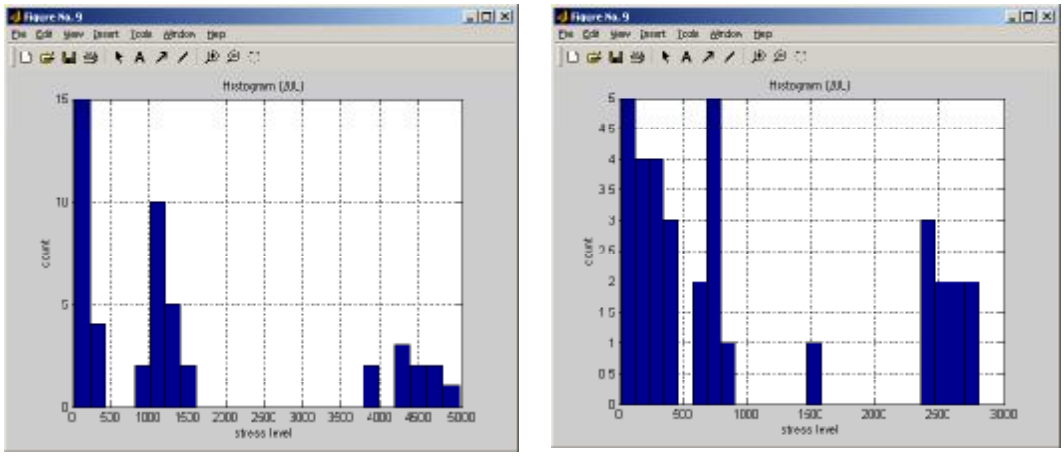

Throw 3
(Power & Compressor)

Throw 2
(Power Only)

Figure 32. Sample Histogram of Stress Reversals
(2-Second Interval)

Figure 33 seeks to show the potential implication in life of the stress level and occasional spikes from the combination throw compared to the "power only" throw. It assumes a gradual slope to the long life portion of the SN diagram with slope guided by experience on a few long life shafts. It is emphasized that this figure does not provide absolute information, just comparison. The hours to failure for the power-only throw are projected at least one thousand times the hours to failure for the power/compression

combination. The spikes produce momentary damage accumulation, such that, if the engine were always to run under this momentary condition, life would be reduced by a factor of more than 10. Thus, the potential life implications of the observed stress levels could be significant, but are not in themselves conclusive.

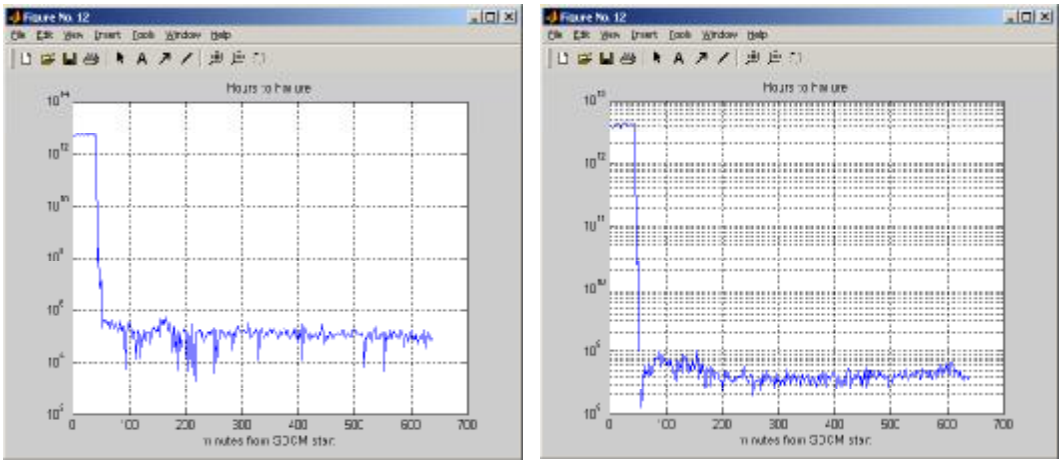

Throw 3
(Power & Compressor)

Throw 2
(Power Only)

Figure 33. Comparative Life Estimate – HBA-6T – Test #1

4.2.2 Relating Crankshaft Integrity to Combustion Balance

This subsection explores the relationship of possible cyclic strain damage to the state of engine balance. As background, Figure 34 shows the changes in average peak-firing pressure spread and the variation in average instantaneous spread during a six-hour test period in which various balancing strategies were investigated. The various timing and balancing approaches (Peak-Firing Pressure (PFP) balancing and Coefficient of Variance (COV) balancing) are noted. Conventional PFP balancing, starting just after 10:09 AM, reduces the average PFP spread almost by a factor of two, but has a smaller (20%) relative influence on reducing the average instantaneous spread. Increasing the timing to 13 degrees BTDC enabled further reduction in average PFP spread to about 80 PSI. Turning all fuel valves open 100% increased both measures of spread to 250 and 300 PSI, respectively. PFP balancing from this condition, now with timing at 14 degrees BTDC, reduced average PFP spread to about 75 PSI. Starting at 1:14 PM, COV balancing

(increasing fuel flow to the cylinders with highest COV for cycle-to-cycle variation) increased both measures of spread, but reduced the difference between them.

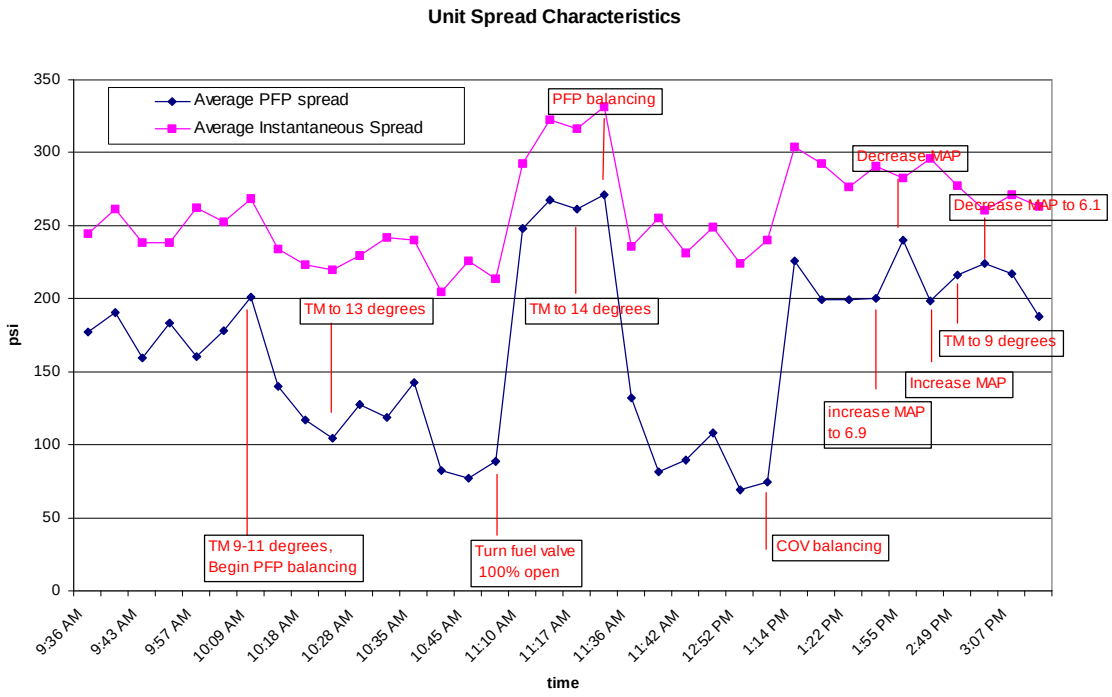

Figure 34. Unit Peak-Firing Spread Test Characteristics – HBA-6T – Test #1

In Figure 35, a measure of the "smoothness" of the crankshaft dynamic stress variation is plotted against time. This measure, referred to as T70, equals the time in minutes since the previous crankshaft dynamic strain above 70 microstrains was observed. Also in Figure 35 is the difference between instantaneous and average PFP spread values, which provides an intuitive measure of the smoothness of operation. Both PFP and COV balancing lead to evidence of increased time between high strain events.

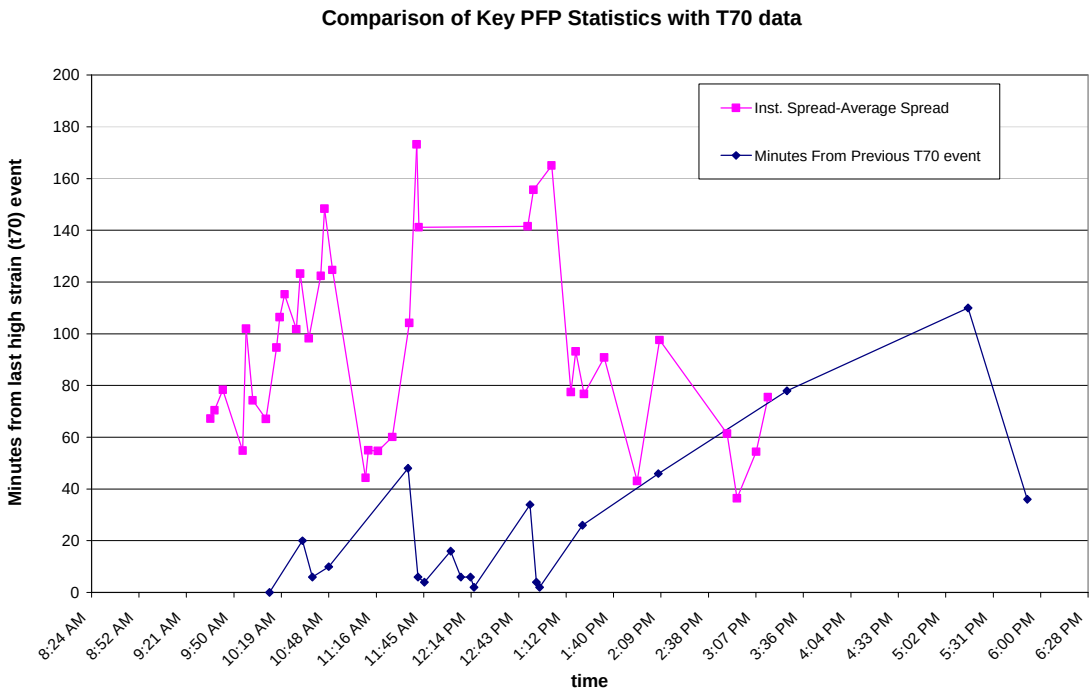

Figure 35. Comparison of Key PFP Statistics (Instantaneous Speed – Average Spread); and Time from Last 70+ Microstrain Event – HBA-6T – Test #1

COV balancing provides clear evidence of an improvement in engine smoothness. Unfortunately, the ability to pursue COV balancing was limited by the available range in fuel valve adjustments coupled with air imbalance, which will be discussed further below after vibration is discussed.

4.2.3 Relating Operational Severity to Torsional and Lateral Vibration

Figures 36 and 37 presents bearing centerline vibration at the flywheel and oil pump ends of the unit as raster plots (throws 1 and 6). The signals stay remarkably constant during the changes in balance approach and spread discussed previously and, therefore, do not appear promising as measures of severity of operating conditions.

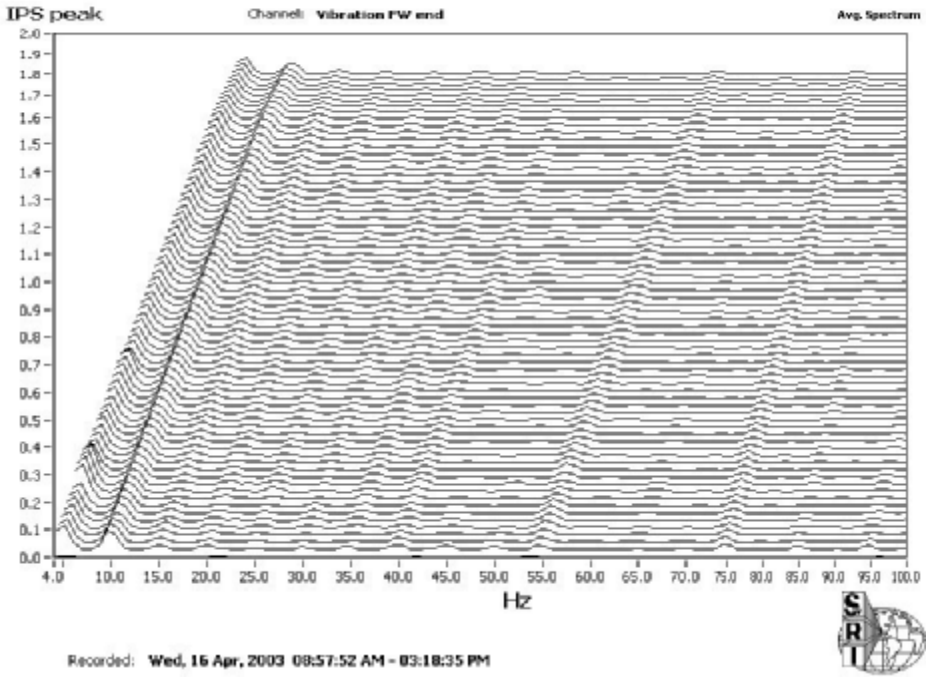

Figure 36. Vibration Bearing Centerline (Throw 1)

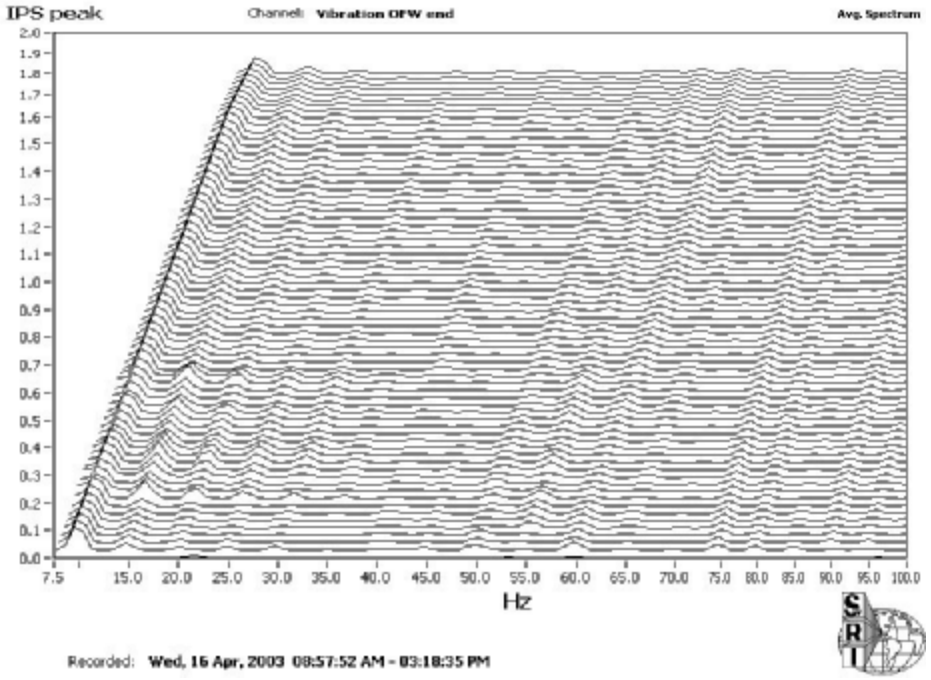

Figure 37. Vibration Bearing Centerline (Throw 6) – HBA-6T – Test #1

Figure 38 presents the peak-to-peak variation in crankshaft instantaneous rotational velocity (IRV) expressed in RPM during the changes in balance condition. It will be difficult to extract a distinguishing measure of severity from the peak-to-peak IRV variation.

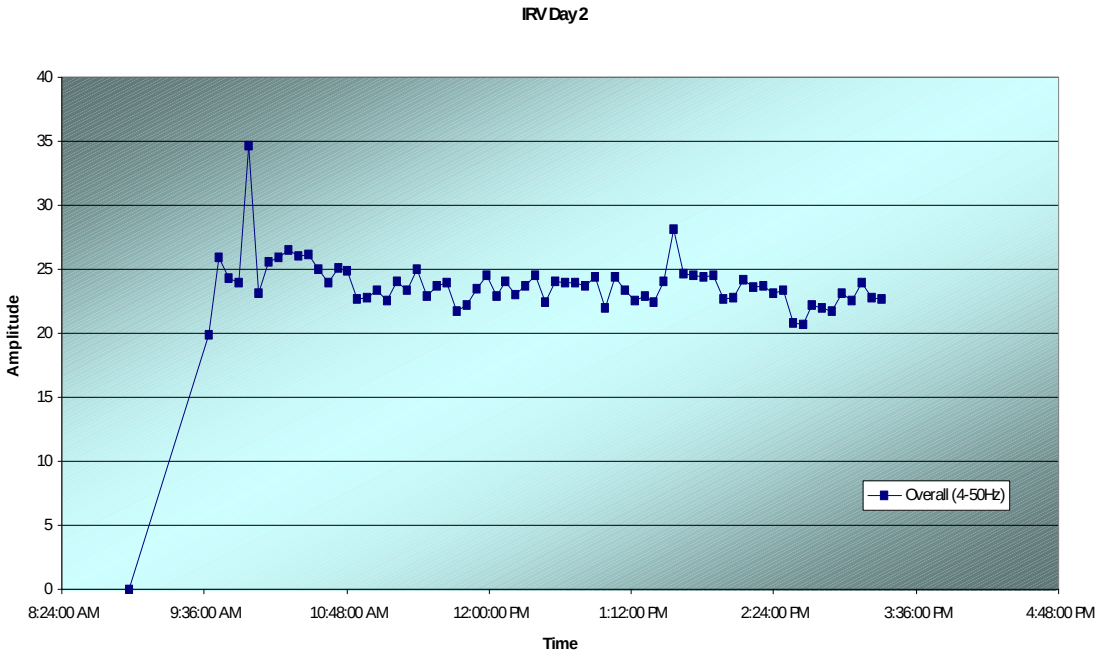

Figure 38. Summary Crankshaft Rotational Velocity

By comparison to the vibration and IRV data, the strain data capture module results clearly provide a more sensitive measure of severity of dynamic loading and potential damage.

4.2.4 Air Imbalance

Close review of the power cylinder pressure plots during balancing revealed a spread between the "compression pressure" values. This is the pressure developed prior to ignition as a result of compression of trapped air and fuel by piston motion following port closure. A spread in this pressure implies a different mass of trapped air (air imbalance)

in the power cylinder, and also represents a different point from which pressure builds as a result of heat release after ignition. Figure 39 shows traces from power cylinders #2 through #5, and makes clear the spread of 10% or more in compression pressure. Figure 39 also shows how the PFP spread is greater than the compression pressure spread, and how the PFP does not necessarily correlate with compression pressure.

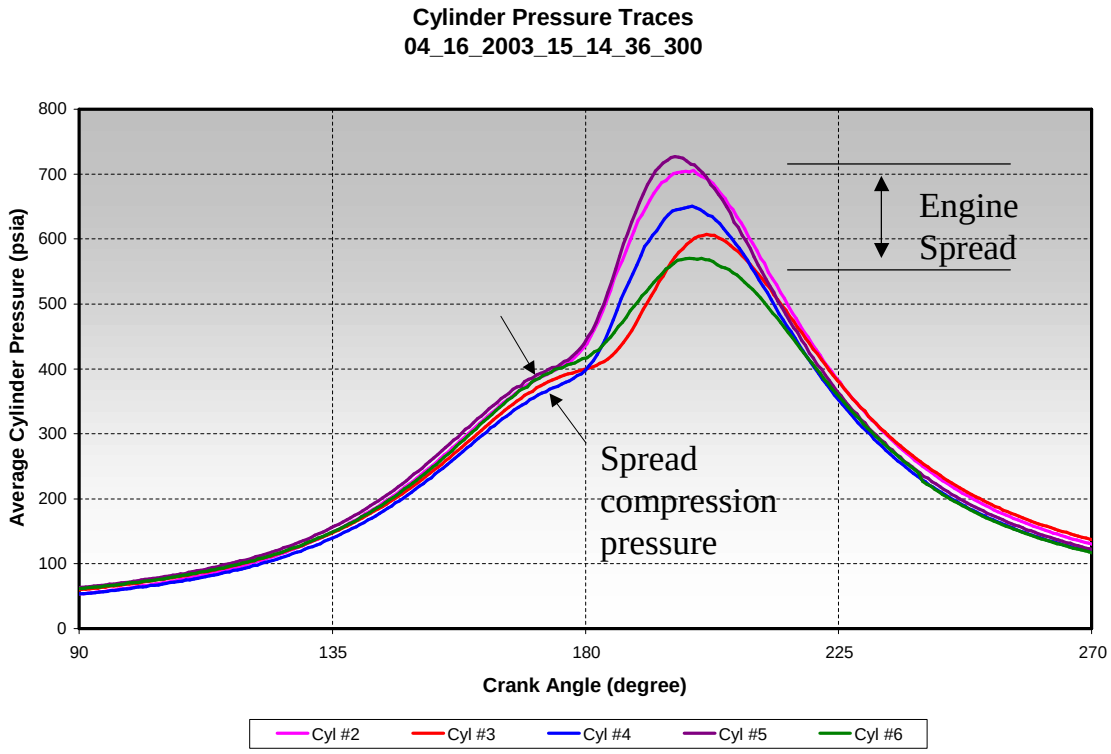

Figure 39. Sample HBA-6T Cylinder Pressure Data

Figure 40 shows the compression pressure for five power cylinders (without cylinder #1) and its variation through 36 samples covering more than six hours of testing with different balance conditions. The cylinders clearly track each other closely in compression pressure. Although not explicitly shown in Figure 40, the data shows that compression pressure does not exhibit the cycle-to-cycle variation that the PFP shows. The compression cylinder spread is a repeatable characteristic of the engine. Balancing to achieve equal PFP has to compensate in fuel flow for these inherent differences between cylinders.

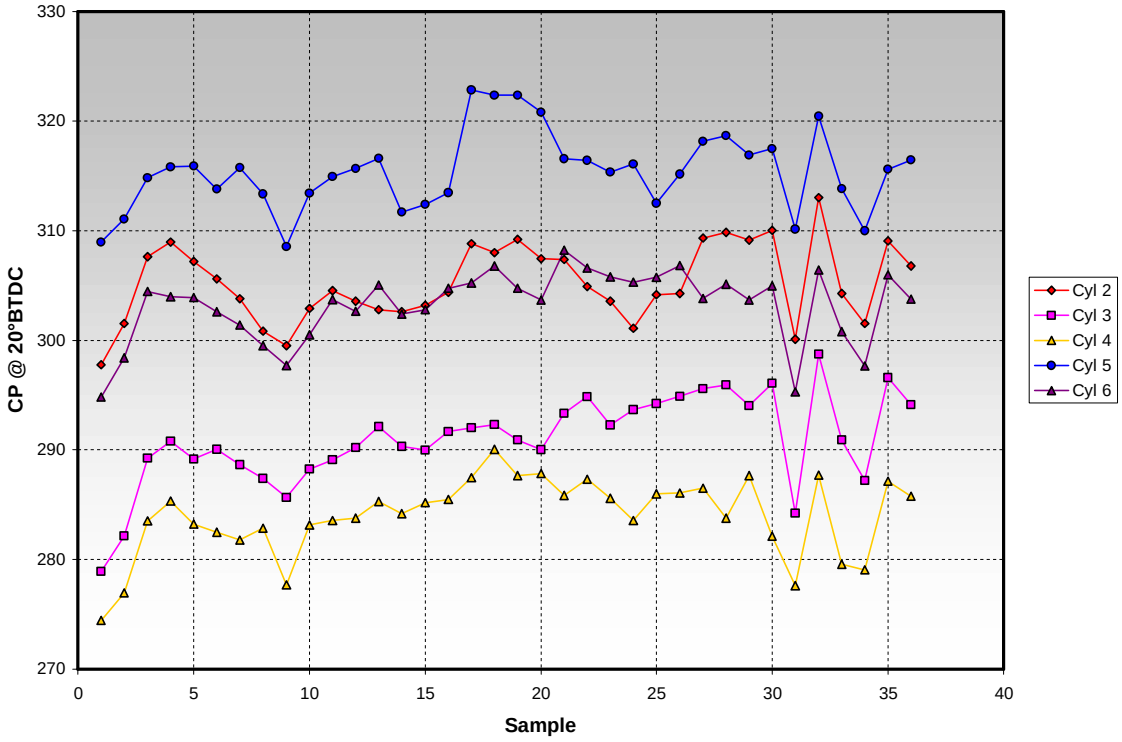

Figure 40. HBA-6T Test Data, Cylinder Pressure 20 Degrees Before TDC (Compression Pressure)

4.2.5 Relating Air Imbalance to Manifold Flow Dynamics

The potential reasons for the cylinder-to-cylinder variation in compression pressure include:

- Manifold Dynamics
- Differences in Liner Port Flow Area or Coefficient
- Compression Ratio Variation Due to Dimensional Differences in Pistons, Heads, and Liners
- Excessive Blow-by
- Variations in Crankshaft Rotational Velocity Over the Cycle

These all need to be assessed. However, it will be recalled that air manifold pressure at the measurement location exhibited a 25% variation over each revolution, as shown in Figure 25. This implies a similar spatial variation in air manifold pressure. The local air manifold pressure drives air flow through the ports into the cylinder. Inevitably, air flow is a significant contributor to the cylinder-to-cylinder variability in trapped air mass, and therefore in compression pressure, so air manifold dynamics are a likely candidate for the primary cause of compression pressure difference.

Based on this relationship, an investigation has been proposed which will seek to reduce air imbalance by redesign of the manifold (air exhaust) to reduce sensitivity to manifold flow dynamics in a laboratory engine.

4.2.6 Engine Simulation

To assist understanding of engine characteristics observed during the tests, a single cylinder combustion model (virtual engine) was applied to this and adjusted to fit observed burn rate characteristics of the average cylinder. The cycle simulation model utilized is based on prior models developed specifically for two-stroke spark-ignited integral engines [3].

This model was then applied to assess the sensitivity of fuel consumption and emissions to changes in trapped air in the cylinder. These changes in trapped air were achieved by changing air manifold pressure in the model. A constant pressure ratio (intake/exhaust) was assumed. While no exhaust pressure measurements were taken, previous data on another straight six indicated a closely constant pressure ratio at a constant engine speed. Empirical relationships for burn rate and combustion efficiency were based on the HBA-6T data.

The NOx model is based on a rate formation model and tuned to the HBA data. The heat transfer model is based on the correlation by Woschni, and also tuned to the HBA data. With these tuned models, the first law of thermodynamics is used to determine cylinder temperature, then pressure.

The single cylinder data was used to predict performance of a six-cylinder engine in which the air manifold pressure driving air into the cylinders was assumed to have an evenly distributed range from high to low across the six cylinders. The fuel flow (or air fuel ratio) was adjusted to achieve constant peak-firing pressure in this engine. The performance and effects of balancing with this engine condition will be compared to the engine condition in which the air manifold pressure is constant across all cylinders, the air fuel ratio is also constant, and as result of this desirable condition peak-firing pressure is constant across the cylinders.

As a starting point, Figure 41 shows the pressure distribution in which a random imbalance in air fuel ratio of about 15% is superimposed on air imbalance caused by manifold pressure spread of 10% across the engine. This air manifold spread is assumed uniformly distributed from low to high. The compressor pressure spread is 35 PSI and the peak pressure spread is 180 PSI.

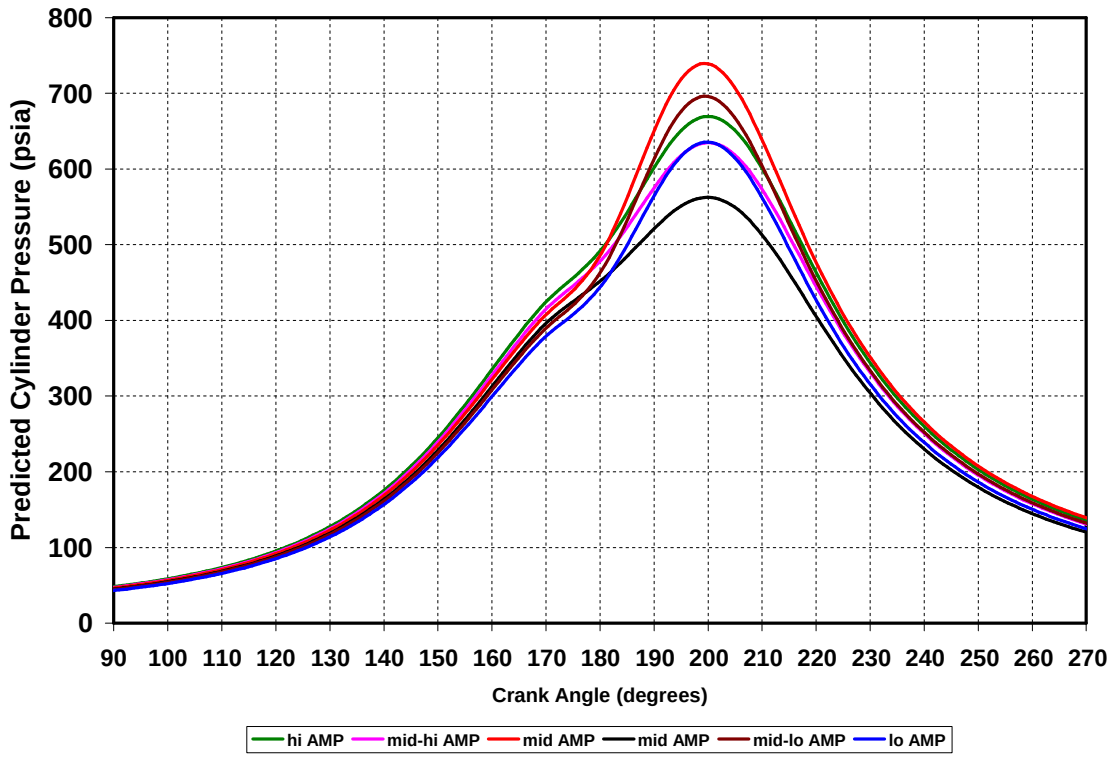

Figure 41. Unbalanced Engine Simulation - Spread in Compression Pressure Induced by Even Increment Spread in AMP - 15% Random Spread in A/F Ratio

4.2.7 Using the Engine Simulation Model to Relate Combustion Balancing to Engine Performance with Air Imbalance

Figure 42 shows the predicted cylinder pressure variation for the engine balanced to achieve equal peak-firing pressure across all six cylinders.

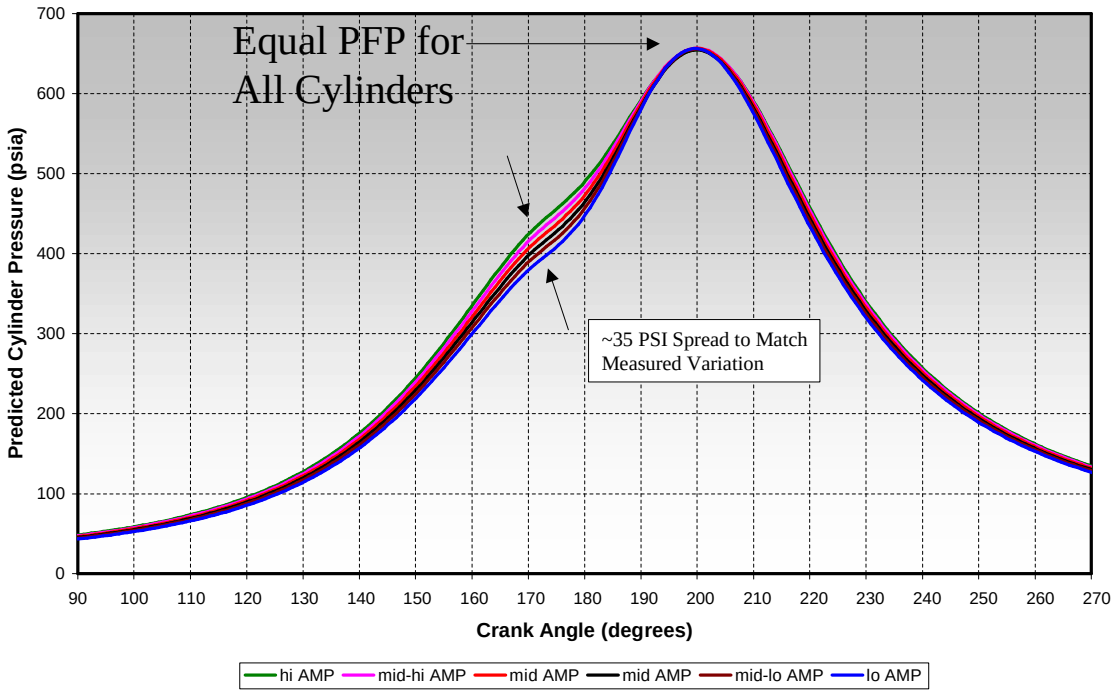

Figure 42. Predicted Cylinder Pressures – Simulation with Evenly Distributed Variation of Air Manifold Pressure

Figure 43 then shows the distribution of trapped air fuel ratios required to achieve the constant peak-firing pressure exhibited in Figure 42. The required trapped air fuel ratios range from 23.8 to 25.9.

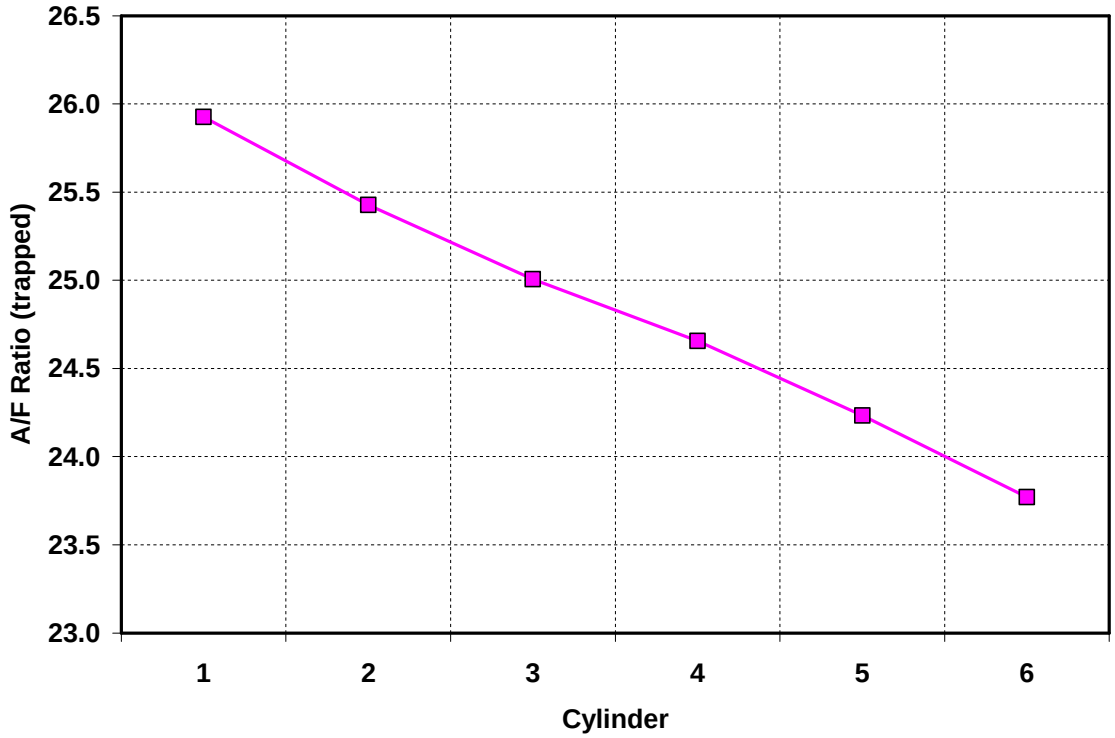

Figure 43. Variation of A/F Ratio Across Cylinders to Achieve Balanced Peak-Firing Pressure with Spread in Compression Pressure

This spread in trapped equivalence ratios will not only cause NOx emissions to be increased from that expected from the mean equivalence ratio, but also reduce the operating range of the engine. This is illustrated in Figure 44 below showing an operating map for a typical Lean-Burn Spark-Ignited (LBSI) gas engine. At a constant engine speed and load, the major control parameters are spark timing and equivalence ratio. These can be adjusted to meet either a NOx emissions or efficiency target, or both. Limits to operation of a LBSI gas engine are the lean flammability limit and the knock (detonation) limit. A specific NOx emissions level is typically a linear function of spark timing and equivalence ratio, as illustrated in Figure 44. There is typically an "island" of best efficiency for a moderately lean equivalence ratio and advanced timing. Depending on the combustion chamber and engine load, this "island" will be near the knock limit or some distance below it. An optimum operating point for a given NOx emissions level will be at as lean an equivalence ratio and as advanced a timing as possible with acceptable margins from knock and lean instability. An engine with widely varying

equivalence ratios per cylinder, group A in Figure 44, will result in a somewhat rich mean equivalence ratio and require retarded spark timing to operate within the limits. The lean cylinder(s) will be prone to misfire and the rich cylinder(s) will be prone to knock, reducing the margins of operation. The engine-out NOx emissions will be abnormally higher, and the efficiency will not be as good for a given NOx limit. The same engine with balanced air and fuel, group B in Figure 44, provides a much greater operating range that can allow adjustment for either increased efficiency at a given NOx or lower NOx for a given efficiency, with increased margins from knock and lean limits. This balanced engine will be less sensitive to changing ambient conditions, temperature and humidity, due to the increased margins.

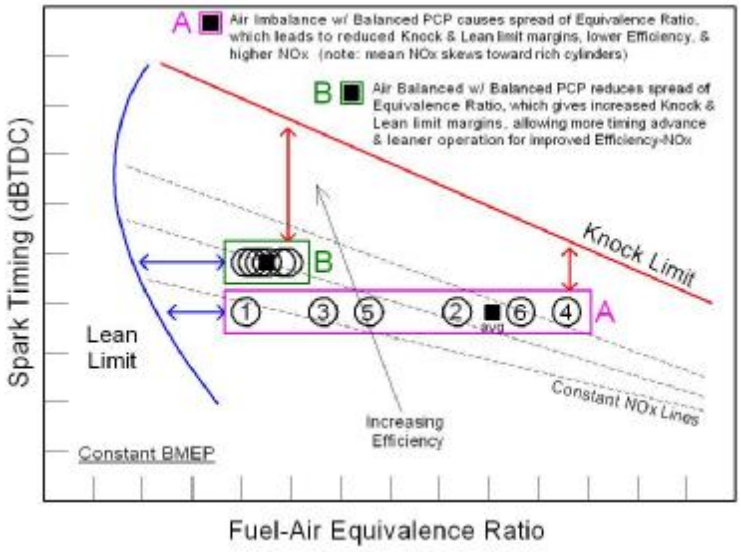

Figure 44. Typical Lean-Burn Spark-Ignited Gas Engine Operating Boundaries

Figure 45 compares predicted NOx and BTU/HP-hr. for three conditions:

- With air manifold imbalance leading to 35 PSI compression spread and a random additional 15% spread in A/F ratio.
- With air manifold imbalance leading to 35 PSI compression spread and air fuel ratio adjusted to achieve equal values for peak-firing pressure in all cylinders.

- With no air manifold imbalance and zero compression pressure spread balanced to achieve constant PFP across the cylinders.

Figure 45 shows predicted benefits of balancing to achieve equal peak-firing pressure: 57.6% reduction in NOx and a 12 BTU/HP-hr. reduction. Further balancing of the air and achieving equal air fuel ratio is predicted to achieve a further 27.1% NOx reduction, and a further 3 BTU/HP-hr. reduction. The predicted benefits of balancing peak-firing pressure and air fuel ratio have not been confirmed by specific testing. The contributions of improved mixing and other in-cylinder technology enhancements are also critical factors in reducing emissions and fuel consumption. Their benefit should, however, be maximized for cylinders with optimized air balance.

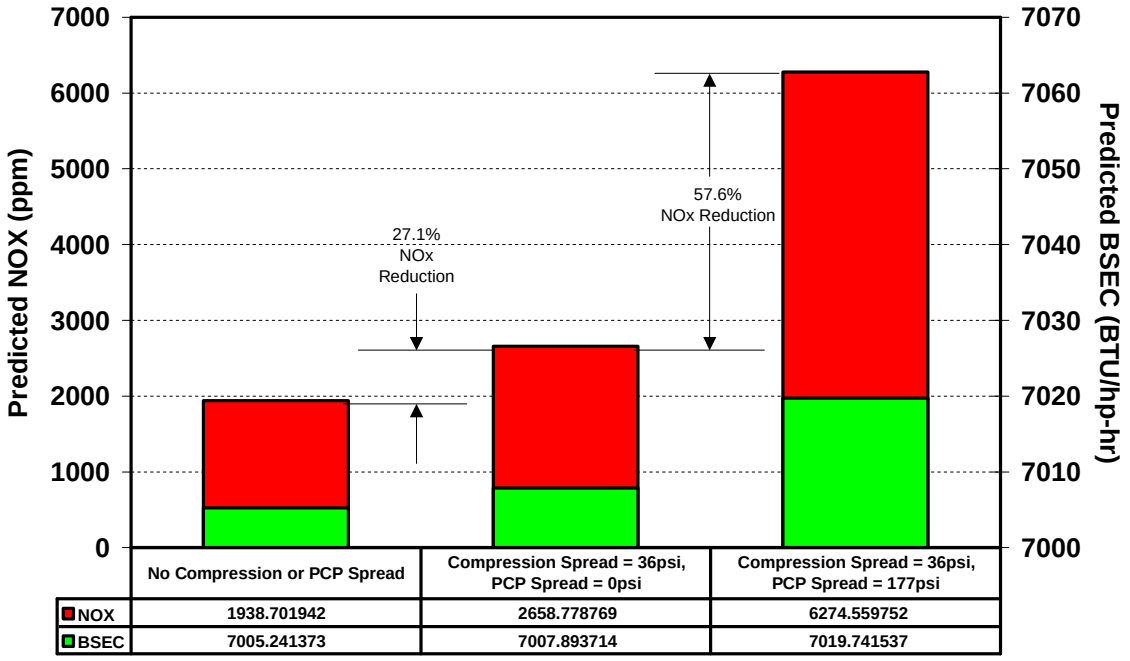

Figure 45. 6-Cylinder Engine Simulation Comparison - Balanced and Unbalanced Peak Cylinder Pressure

4.2.8 Relating Combustion Balancing to Trapped Air Fuel Ratio

Figure 46 shows the pressure distributions which result from imposing constant trapped air fuel ratio in each cylinder for the engine with 10% air manifold spread, causing 35 PSI compression pressure spread-out. The predicted NOx and fuel consumption, which this condition achieves, is the same as that with the air manifold spread eliminated. The qualification with this is that there may be insufficient fuel adjustment range on cylinders with excessively high trapped air mass. Also, the load distribution along the crankshaft may not be optimum for crankshaft integrity.

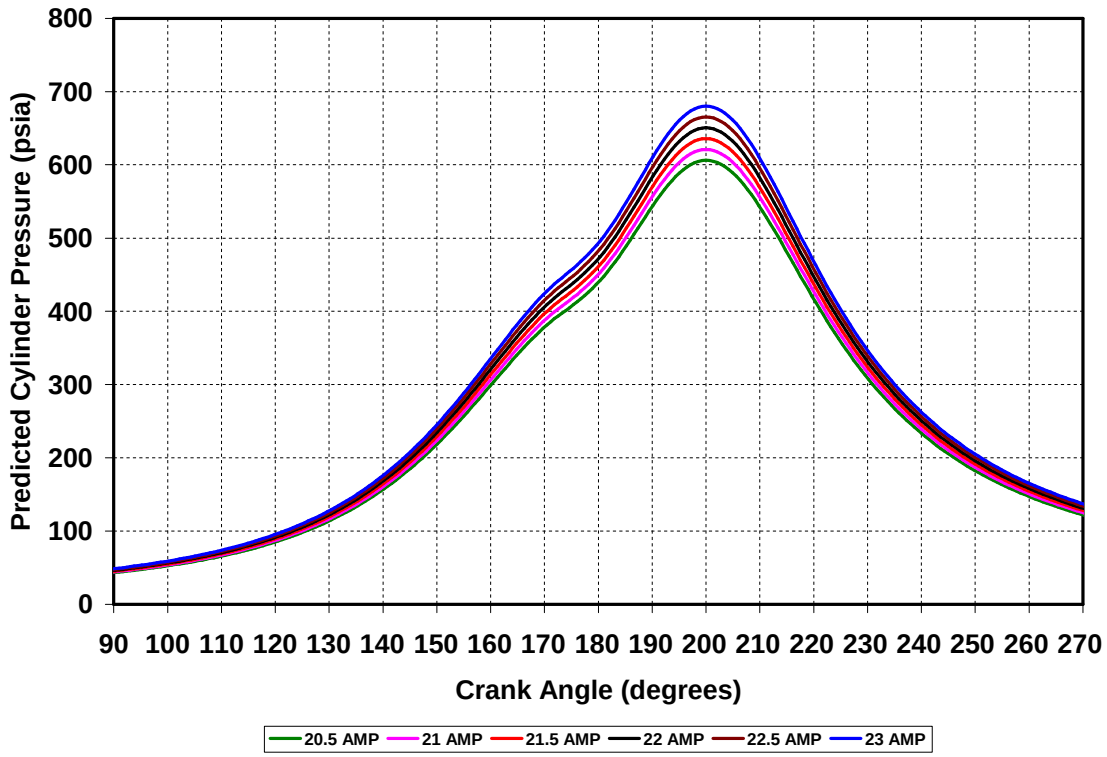

Figure 46. Engine Simulation - Pressures for Constant Equivalence Ratio with Spread in Compression Pressure

Figure 47 shows the distribution of peak pressure normalized with respect to pressure 20 degrees before top dead center for three conditions of an engine with 10% air manifold spread:

- Air Fuel Ratio (Equivalence Ratio) Balanced (AF Balance)
- Unbalanced
- Peak-Firing Pressure (PFP) Balanced

The results of Figure 47 are revealing. If we refer to the ratio of peak-firing pressure to compression pressure as Combustion Pressure Ratio (CPR), Figure 47 shows that only if the air fuel ratio is the same for all cylinders, is the predicted CPR equal for all cylinders of an engine with air imbalance. Peak-Firing Pressure (PFP) balancing causes the CPR to vary from cylinder-to-cylinder in proportion to the amount of air imbalance. Of course, an unbalanced engine has neither equal CPR nor equal PFP. This set of results provides, as a corollary, a new procedure with which to pursue combustion balancing. Specifically, if we compute CPR and make fuel adjustments to equalize CPR rather than PFP, we should more closely equalize air fuel ratio across the cylinders.

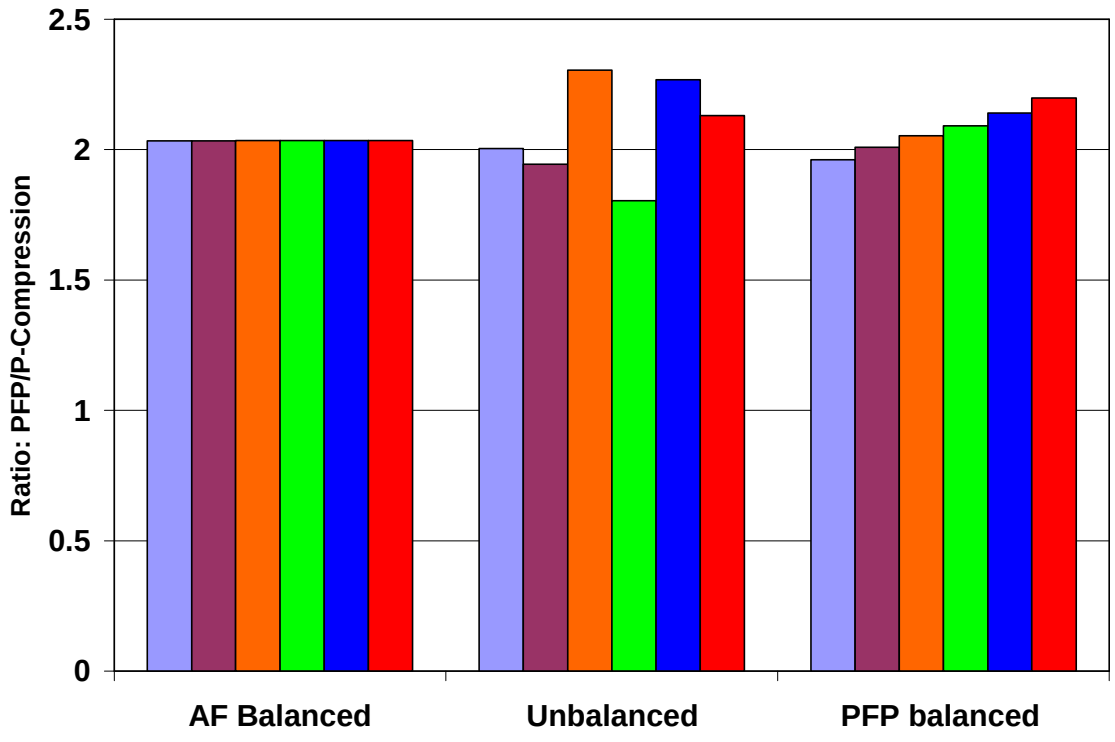

Figure 47. Ratio of PFP to Compression Pressure for Three Different Balancing Situations

On the basis of this result, an invention disclosure was prepared, and SwRI subsequently filed for a utility patent in early September 2003.

4.2.9 Relating System Mechanical Efficiency to Oil Temperature and Time

The term "system mechanical efficiency" is used in recognition that the mechanical efficiency, used as common practice by the industry for relating BHP delivered to the crosshead to power at the compressor piston face, may in concept include fewer losses than in the mechanical efficiency between power piston face and compressor piston face. Figure 48 shows for the HBA-6T engine tested how compressor piston power, engine piston power, and their ratio ("inferred system mechanical efficiency") varied over six hours of testing. The ratio of compressor piston power to engine piston power increased (with a few momentary reversals of this trend) from the start of the test series.

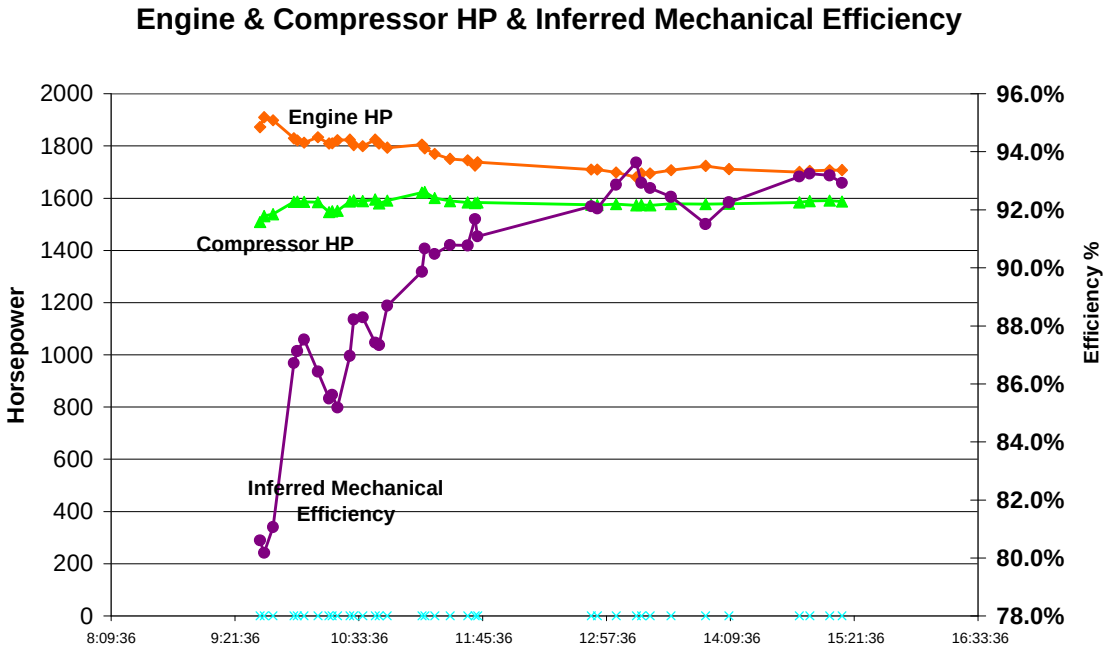

Figure 48. Engine HP, Compressor HP, and Inferred Mechanical Efficiency

Figure 49 uses station records to provide some supportive evidence that the engine heat rate (BTU/HP-hr.) dropped over the same period. The change is 4 to 5%. This is not as large as the apparent increase in system mechanical efficiency, but an effect that would

partially explain this is the influence of engine load on brake thermal efficiency. This efficiency tends to reduce as engine load reduces, so reducing the impact on fuel flow in comparison to a proportional relationship.

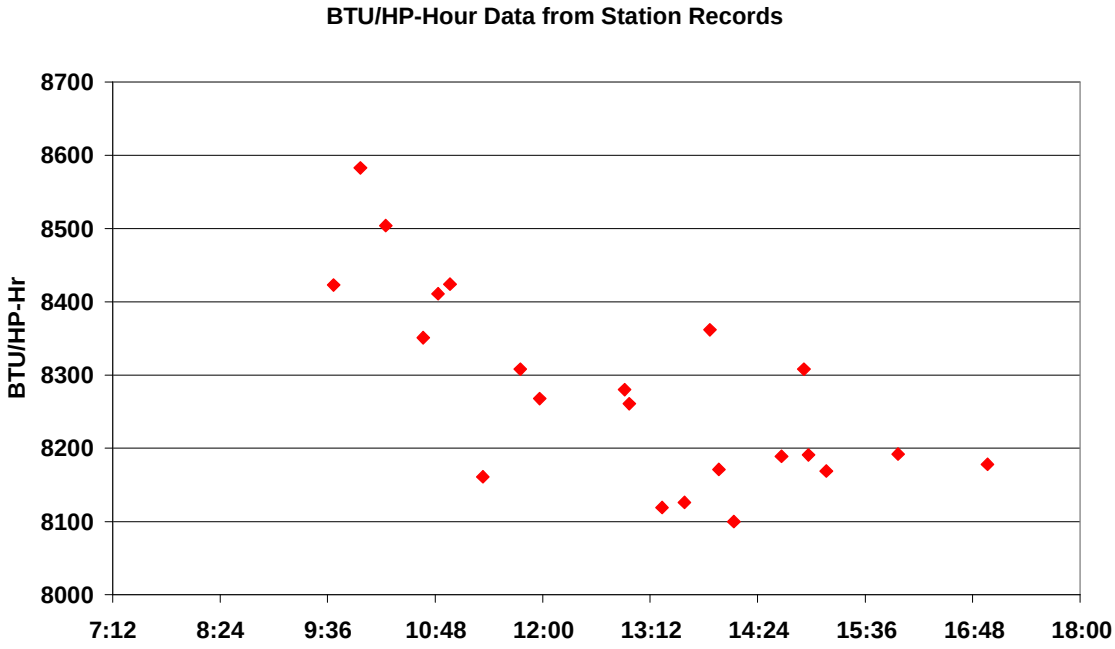

Figure 49. BTU/HP-Hr. Data from Station Records

The most obvious parameter which might be changing after start-up, and which would influence system mechanical efficiency is oil temperature – the period might seem long for oil temperature to stabilize, but records show that, at least for the HBA engine, oil sump temperature is surprisingly slow to reach a stable operating temperature. Data recorded in 1984 on a PRCI project [4] related to crankshaft alignment (reproduced in Figure 50) indicate that sump oil temperature continues to rise for as many as five hours after a start-up, starting at 80 to 90 degrees and reaching 145 to 150 degrees. There is a daily temperature cycle for sump oil temperature, in addition to the increase in temperature following start-up. Sump oil temperature is an indicator of the oil temperature, which reaches the crosshead bearings, main bearings and pin bearings through the crankshaft, and the temperature of oil reaching the rider bands. This temperature has a direct influence on the viscosity of the oil being sheared in the

bearings, and at other close clearances between moving parts. For the recent tests, data is not available for the sump temperature, but in Figure 51, lube oil outlet temperature is plotted as a function of time, and clearly has a shape remarkably similar to the mechanical efficiency curve. Oil temperature, at inlet to the bearing, will be lower than this, and so there is a credible hypothesis that mechanical efficiency is a strong function of oil inlet temperature, since viscosity is also a strong function of oil temperature.

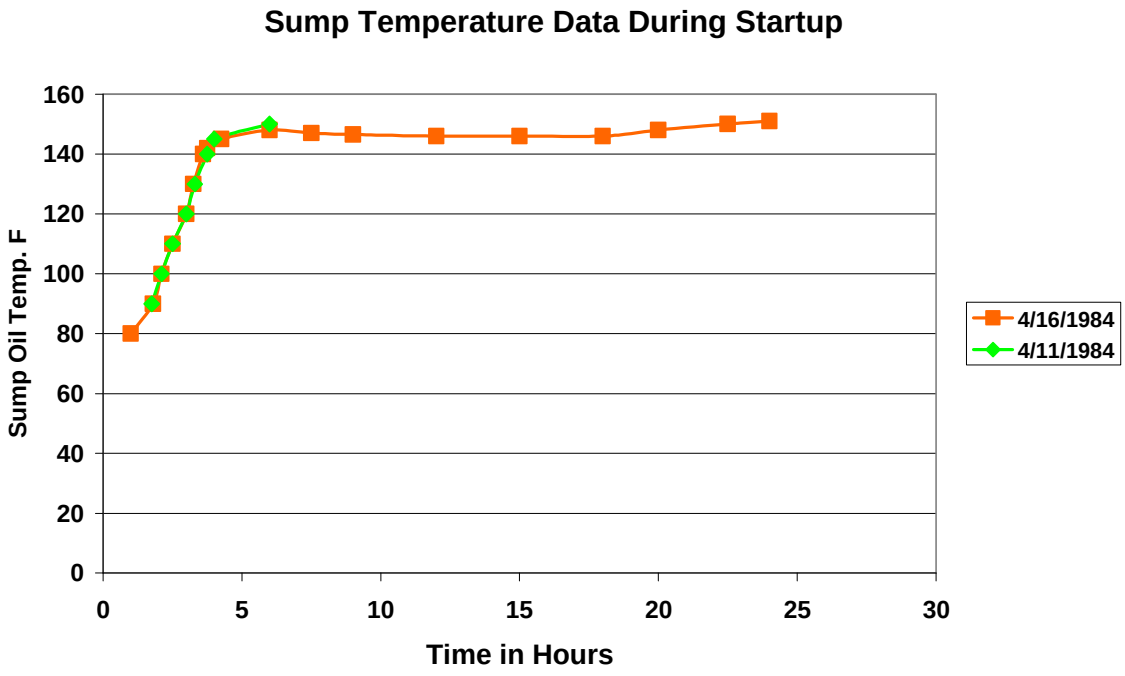

Figure 50. HBA8 Sump Temperature Data (1984)

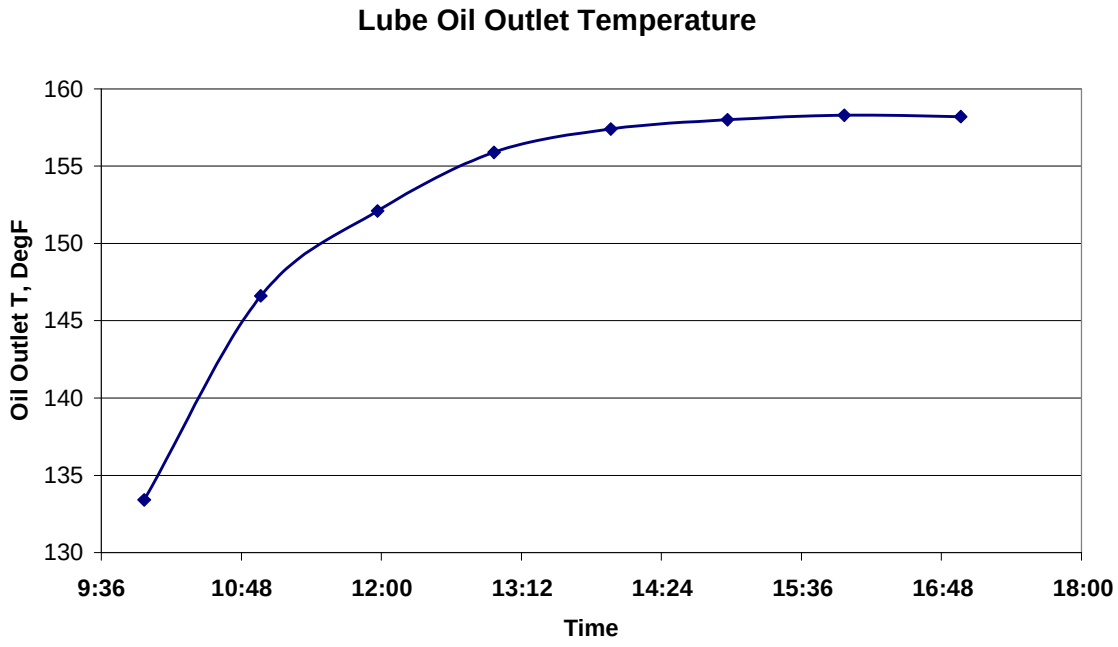

Figure 51. Oil Outlet Temperature *versus* Time from Station Records
(Note Increase Over 5 Hours Matches Mechanical Efficiency Trend)

4.2.10 Relating Engine-Compressor Efficiency Definitions to each Other and to the Data from the First HBA-6T Test

The Engine/Compressor System Thermal Efficiency – the purpose of introducing system thermal efficiency is to focus on the overall efficiency of fuel use in providing useful compression energy to the transported gas. This addresses the complete function of the compressor and combines several measures of component efficiency commonly discussed in relation to integral engine compressors, as defined below.

The Engine Brake Thermal Efficiency – the ratio between power available to the crossheads of the compressor and power consumed as fuel gas energy by the engine.

The Compressor Mechanical Efficiency – the ratio between power available at the compressor piston faces and power available to the crossheads.

The Compressor Thermal Efficiency – the ratio between the ideal (lossless) power to raise the pressure of the gas from suction to discharge pressure, and the actual power consumed in the compressor cylinders.

Engine/compressor system thermal efficiency is the product of these three component efficiencies. Because of the incomplete measurement set at the first test site, the following discussion uses data with several inferences and assumptions in it, but is intended to provide some approximate trends, and to illustrate expectations of what may be better inferred with a more complete instrumentation set.

For this test, the only available fuel flow measurement available was from the station instrumentation. Figure 49 has shown that the inferred BTU/BHP-hr. from the station data dropped over six hours of testing from 8500 to 8200. It should be noted that this efficiency relates power at the crosshead to fuel power. Expressed as a brake thermal efficiency, this data implies an increase over six hours from 29.9% to 31.0%. Combined with an assumed constant compressor mechanical efficiency of 95% and compressor thermal efficiency of 91% (see Figure 27) the engine compressor system thermal efficiency appears to vary from 25.8% to 26.8%.

The inferences and assumptions mainly apply to the BHP in the BTU/HP-hr. calculation. This is obtained from a model of the compressor gas horsepower as used by the host company. In this model, a standard compression exponent is used to calculate from suction pressure, suction temperature, and discharge pressure an ideal compressor gas horsepower. This ideal is then corrected (increased) for flow resistance losses and pulsation effects. The resultant gas horsepower is then translated to an inferred brake horsepower by dividing by a value for compressor mechanical efficiency (95% is used in this calculation). Comparison of station BHP to the data obtained during the test indicates the station BHP numbers were 3 to 5% below those based on measured cylinder pressure. Thus, the 25.8% to 26.8% discussed above for system thermal efficiency might be corrected to record 26.8% to 27.8% based on the cylinder pressure measurements.

Reference [5] provides a typical heat balance for a compressor station, suggesting that 26 to 29% of the fuel energy is delivered to gas discharged from the compressor. Thus, the present data is comparable to this assessment.

The limited GMRC compressor efficiency survey indicates a median of 79% rather than the 91% obtained in these tests – thus, with median thermal efficiency, the industry is also likely to exhibit lower system thermal efficiencies (as low as 23% to 24%).

As has been discussed, the system mechanical efficiency in this test started low and increased as the oil heated up over several hours. Thus, immediately after start-up and for the next few hours, even lower system efficiencies may be expected than the range inferred above.

Limited data is available on brake thermal efficiency norms for the industry. Smalley et al [1] shows that as a global average, the industry burns 8.25 SCF per BHP-hr. At an assumed lower heating value (LHV) of 1050 BTU/SCF, the implied industry brake thermal efficiency is 29.4% – just below the low end of the range for the HBA-6T engine during the tests (29.9 to 31%). Of course, this industry average is a very coarse number and includes turbines as well as four-stroke engines – both separable and integral.

In summary, the compressor tested provides a data point indicating 26.8% to 27.8% system thermal efficiency for an integral engine compressor, once thermally stable operation is established. Industry averages for engine thermal efficiency and compressor thermal efficiency suggest that the average system thermal efficiency for the industry may be lower than this. Engine start-up transients will further lower system thermal efficiency for recently started engines.

4.2.11 Relating DIP-Based Efficiency to Enthalpy-Based Efficiency

Figure 52 shows a comparison between compressor thermal efficiency based on enthalpy rise, and that based on DIP. The close agreement is clear since the total range of

Figure 52 is one percentage point and covers all the data from the first HBA-6T test; the enthalpy-based efficiencies are in the middle of this range.

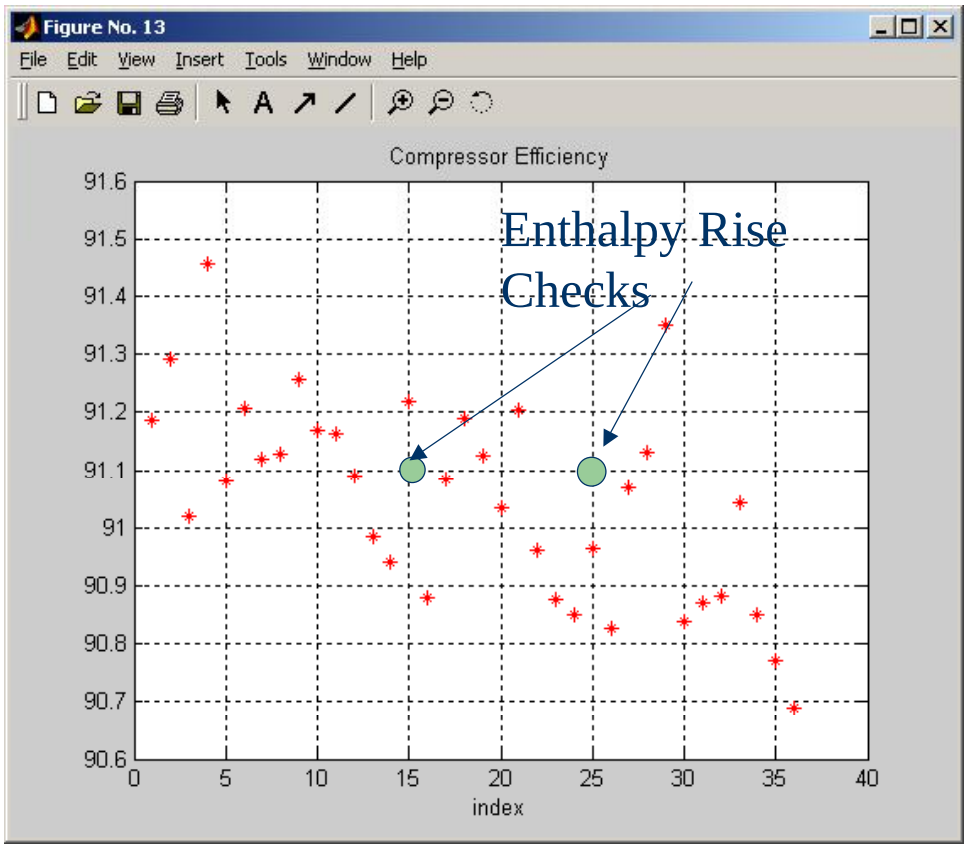

Figure 52. Compressor Performance Data for DIPs (HBA-6T)

4.2.12 Relating Performance to Timing

During the testing, advance in timing were investigated. Unfortunately, the fuel flow measurement was not available to measure the impact. However, it was stated that station practice tended to keep timing less advanced as a precaution against detonation. Some form of detonation detection and active protection would allow timing advance as an option.

4.2.13 Relating Compressor Efficiency to Available Industry Norms

Figure 53 shows where the HBA-6T compressor thermal efficiency lies in comparison to the survey performed by GMRC about 10 years earlier, based on about 120 individual compressor data sets. It is clear that the HBA-6T, on the day tested, was achieving a thermal efficiency at the very top end of industry standards. Informal discussions with industry representatives provides the opinion that 91 to 92% is about the highest thermal efficiency which can be expected from a reciprocating compressor. As such, it is three to four percentage points higher than the most efficient centrifugal compressor.

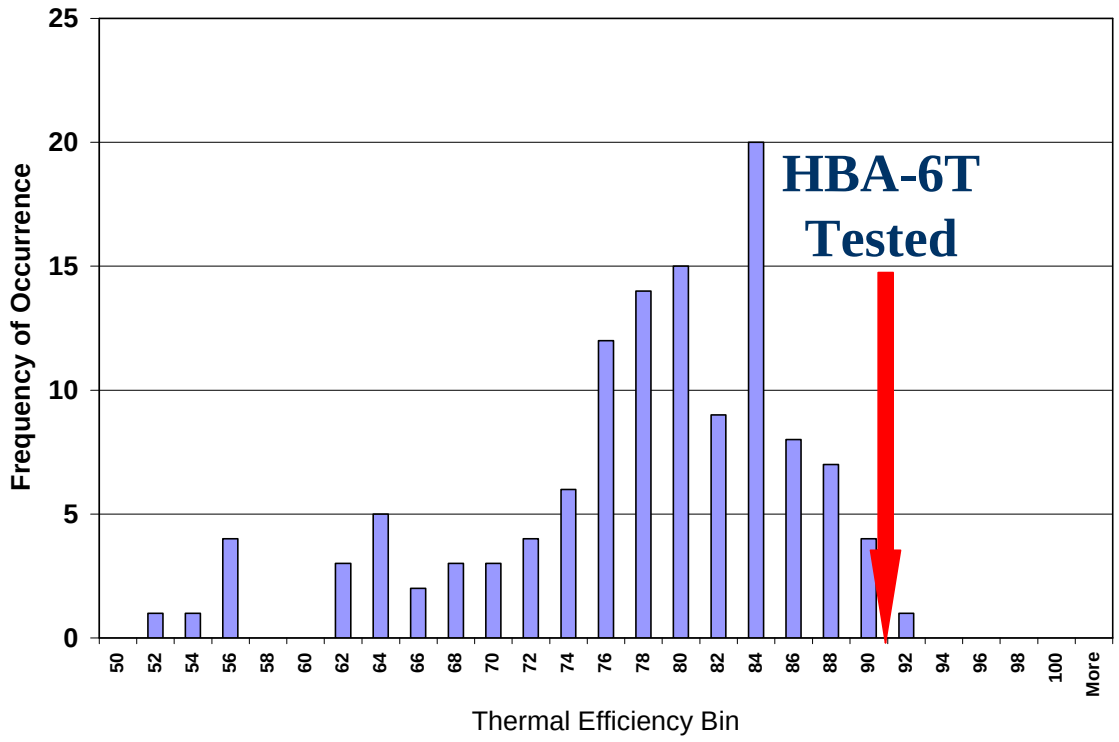

Figure 53. Compressor Efficiency *vs.* Industry Distribution

4.3 TYPICAL DATA FROM THE FIRST TEST ON A GMW10

The first tests on a GMW10 were performed at Williams Transco Station 40, near Sour Lake, Texas. Figure 54 shows the three compressor cylinders. Figure 55 shows the power cylinders, left bank. The unit has high-pressure fuel injection installed

(Enginuity's HPFI^{TM} system) with a turbocharger. Tests were conducted August 25-28, 2003. Tests conducted included a successful demonstration of CPR balancing and a comparison of CPR balancing with PFP balancing, tests on the influence of timing and air manifold pressure on performance, and tests to evaluate the influence of load step and load on engine performance.

Figure 54. Williams Sour Lake Station, Unit 6

Figure 55. Power Cylinder, Left Bank

Figure 56 presents the tabular screen used to display snapshot information relating to both the compressor and engine cylinders. For the ten power cylinders, the top half of the screen shows in columns the instantaneous peak-firing pressure, the instantaneous angular location (after TDC), the pressure at 20 degrees before TDC ("compression pressure"), the average peak-firing pressure, the standard deviation in peak-firing pressure, the indicated horsepower, the instantaneous indicated mean effective pressure (IMEP), the average HP, the standard deviation in horsepower, and the compression pressure ratio (CPR) – defined as the instantaneous ratio of peak-firing pressure to compression pressure. The averages in Figure 56 are rolling averages (FIFO).

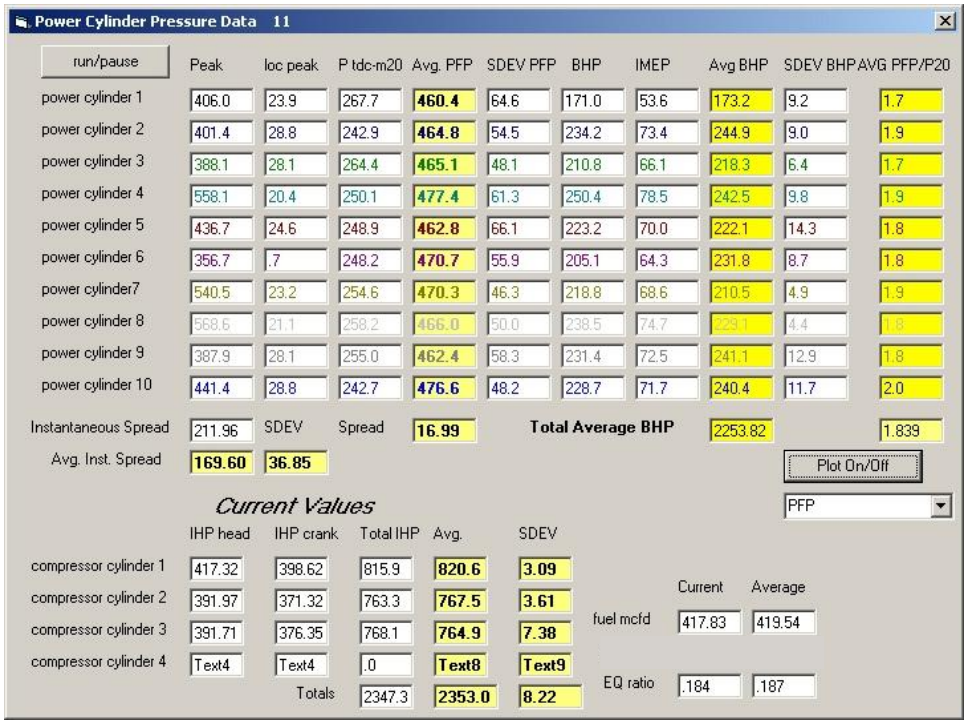

Figure 56. Snapshot of On-Site Real-Time Calculations

It is noted that the standard deviation in peak-firing pressure varies from 46.3 to 66.1 PSI – a 20 PSI difference in standard deviation between cylinders. Standard deviations are about 13% of the average peak-firing pressure.

Below, the cylinder data columns are various averages, totals, and spreads from this typical snapshot:

- The Instantaneous Spread (211.06)
- The Average Instantaneous Spread (169.6)
- The Standard Deviation in Peak-Firing Pressure Instantaneous Spread (36.85)
- The Spread in Average Peak-Firing Pressure (16.99)
- The Total Average Horsepower (2253.82)
- The Average CPR (1.839)

Under the data for the ten power cylinders are the indicated horsepowers for the two ends of each of the three compressor cylinders, together with the total of the two ends for each cylinder. These instantaneous value columns are followed by the average and the standard deviation of the cylinder's horsepower (2353, 8.22).

The exceptionally low (17 PSI) spread in average PFP in this snapshot is attributable to the automated balancing system installed as part of HPFI™. This system is designed to constantly adjust the bias in pulse width on individual fuel injectors in order to minimize the spread in cycle averaged peak-firing pressure. Although disabled during the tests, the biases from prior automated balancing clearly remained close enough during the test program to keep this spread very low.

The total instantaneous indicated horsepower for the compressor cylinders (2347) and the average total indicated horsepower are also shown (2353), with the total standard deviation in horsepower across all the cylinders (8.22). Also on this screen are the current and rolling average values for fuel flow (417.83/419.54) and global equivalence ratio (0.184/0.187). This is a low global equivalence ratio. The influence of the air and injection system appears to be to allow operation acceptably close to the lean limit at a low equivalence ratio.

It may be observed that the power for the power cylinders is measured as about 100 HP below the compressor cylinders. This, of course, is not realistic. The sensors are well calibrated, but the required power cylinder sensor installation shown in Figure 9 is undoubtedly a factor in reducing the apparent horsepower. Because the required piggy-backing separates the SwRI transducers from the cylinder chamber by an additional length, the channel distortion is exaggerated. The filtering induced by the flow passage geometry attenuates the higher frequency dynamic variation, and thereby lowers the observed horsepower. The channel attenuation phenomenon has been well documented [6, 7]. The similarity of installation for the 10 transducers and the similarity in form of the power cylinder traces makes it strongly arguable that the distortion induced in each cylinder is the same for each cylinder and, therefore, that trends observed in horsepower

and peak pressure are valid. The very low spread observed by both the SwRI instruments and the HPFI™ system makes it very likely that the cylinder pressure measurements are consistent with those of the HPFI™ system (upon which they are piggy-backed).

Figure 57 shows typical averaged pressure traces for the 10 power cylinders. These include a numerical value for the current average spread in average peak-firing pressure of about 60 PSI for this condition. This higher spread (and higher peak pressures) probably corresponds to a test condition (e.g., increase in timing advance), which caused both PFP and spread to increase. The similarity of the traces is notable, and even 60 PSI is a relatively low spread in average peak pressure – not above about 12 or 13% of PFP.

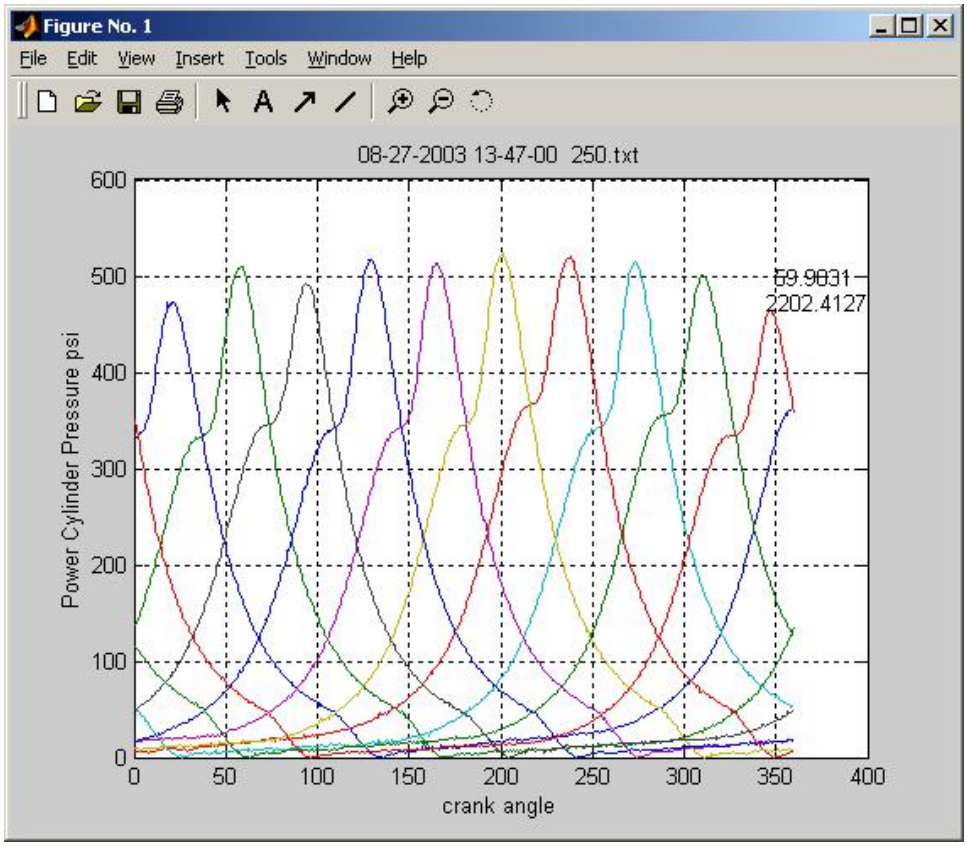

Figure 57. Typical Power Cylinder Pressure Data

Figure 58 shows the corresponding compressor cylinder pressure traces. The header pressures are superimposed. The pulsations in the cylinder pressure, which reflect dynamic response to cylinder/valve dynamics in the attached piping, are apparent in the

cylinder traces. The piping normally includes pulsation control features, which filter out pulsations above a relatively low cut-off frequency with minimum flow resistance. However, the reflections of lower order pulsations in the cylinder pressure traces and the small, but non-zero flow resistance associated with pulsation control filters and choke tubes can influence the unproductive horsepower in the compressor cylinders, and thereby can influence cylinder thermal efficiency.

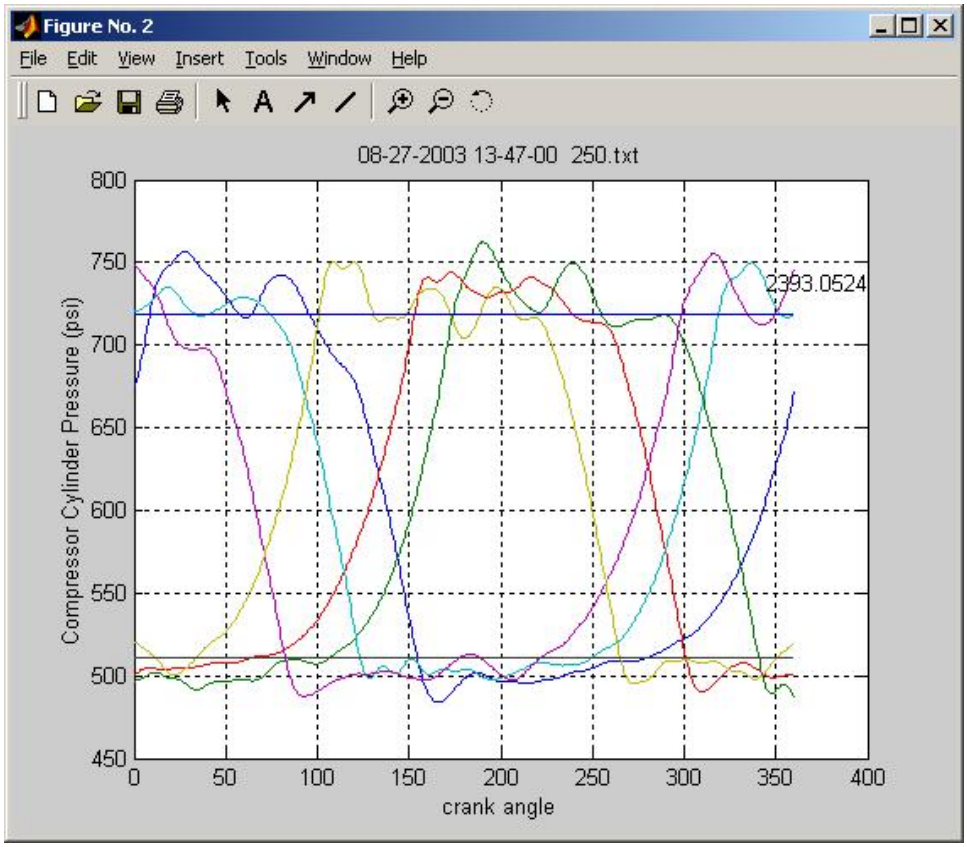

Figure 58. Typical Compressor Cylinder Pressure Data

Figure 59 shows the dynamic variation in inlet air manifold pressure at the location of measurement. The top trace presents the pressure as a function of crank angle over one engine cycle (360 degrees). The lower trace shows the result of transforming the upper trace to the frequency domain, presenting zero-to-peak pressure variation as a function of orders of rotational speed. The upper trace indicates a range from about 4.6 to 5.7 PSIA; i.e., close to 20% of the average, with a series of reversals in the trace within one

revolution. The lower frame of Figure 59 shows that there are peaks at about 3rd, 10th, 16th, and 25th orders, and action to the 40th order.

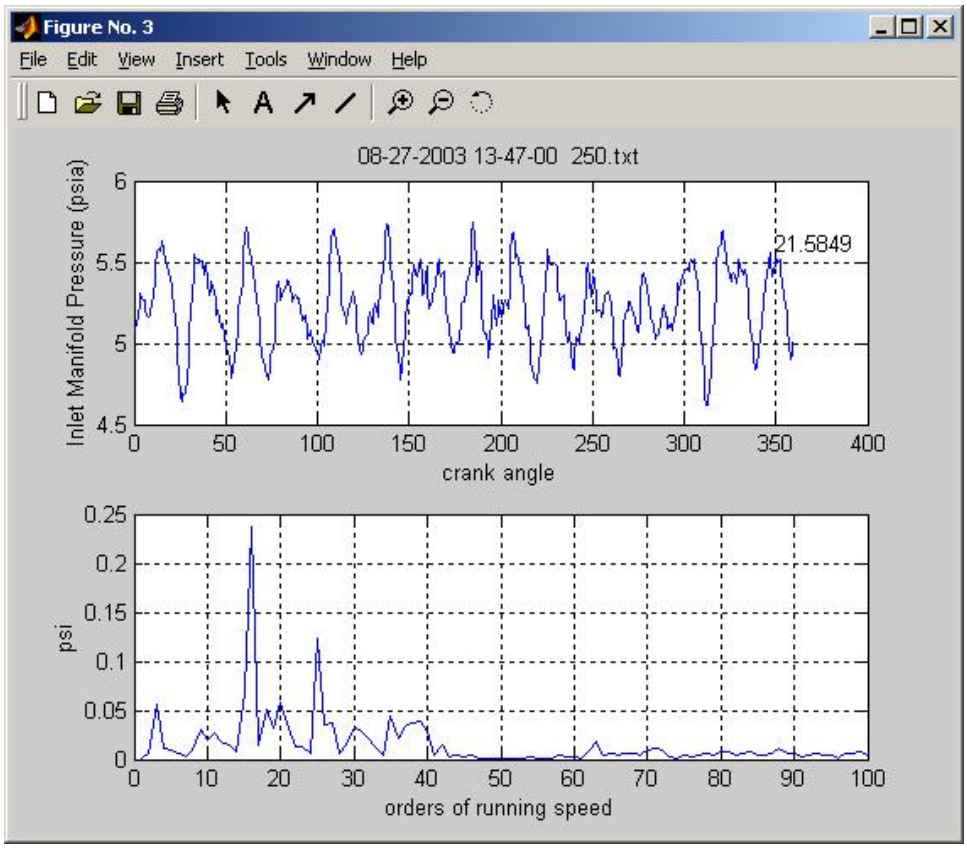

Figure 59. Typical Inlet Manifold Pressure Trace and Order Spectrum

Figure 60 makes a similar presentation to Figure 59 for exhaust manifold pressure. The range shown in the upper trace is from 3 PSI to 4.9 PSI; i.e., close to 50% of the average. The lower trace shows peaks at the 4th, 9th, 11th, and 22nd orders of running speed.

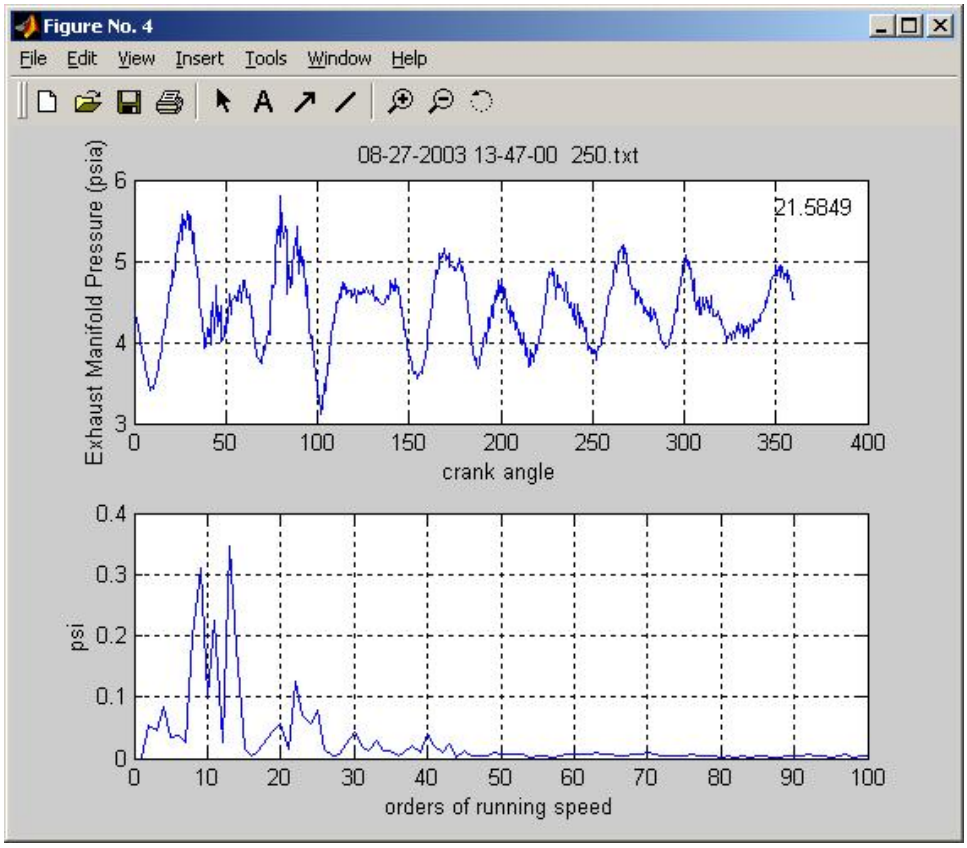

Figure 60. Exhaust Manifold Pressure Trace and Order Spectrum

Figure 61 summarizes the range of variation - typical in the manifold pressures - throughout a day of testing. In general, the inlet air manifold dynamic range lies just below 20% of its average, although a few points exceed 20%. The exhaust manifold dynamic range lies generally just over 50%, ranging from 45 to 70%. These are cycle-averaged pressures indicating both time variation and variation along the manifolds. Since flow into and out of the cylinder is directly influenced by these pressures, the trapped air would be expected to vary from cylinder-to-cylinder as a result of the time/space variation, as previously discussed with respect to data from El Paso Station 823.

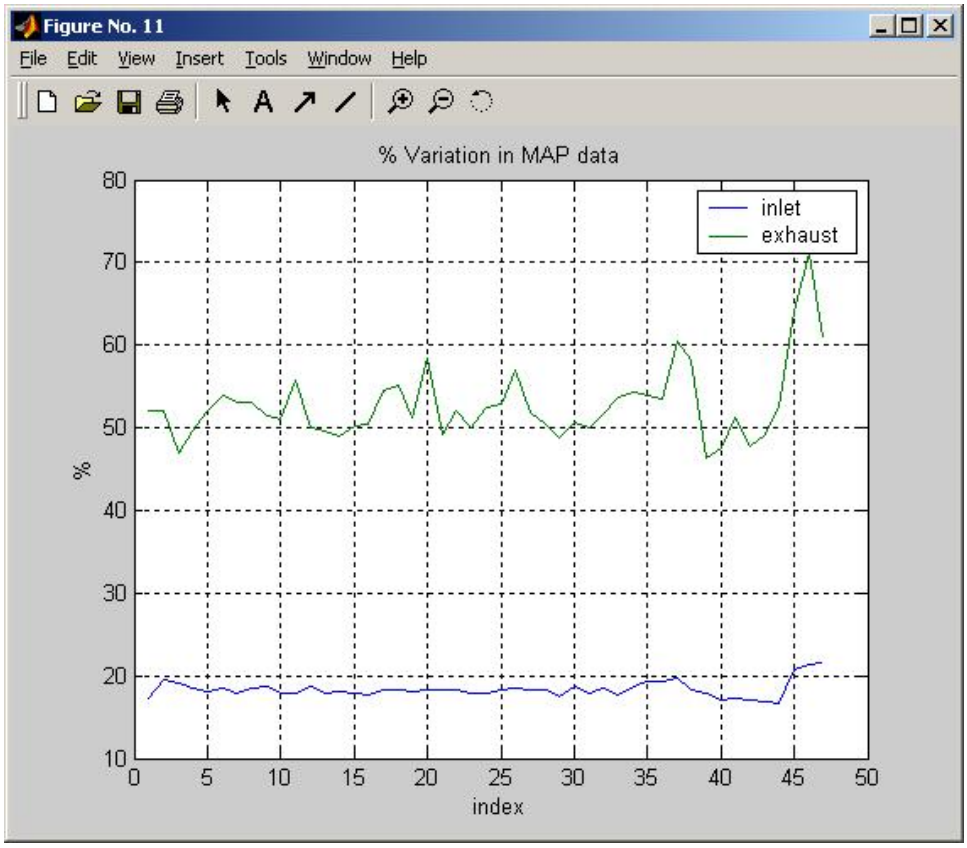

Figure 61. Variation in Inlet and Exhaust Pressures at Point of Measurement

Figure 62 shows the cycle-averaged output of the rod load sensor in the format of rod load *versus* crank angle over a single revolution (360 degrees). The inferred rod load ranges from -47,000 lb. to +55,000 lb. — a total range of 102,000 lb. The variation reflects the difference between head-end pressure force and crank-end pressure force, together with the inertia force resulting from acceleration and deceleration of the piston. Further analysis in conjunction with piston kinematic analysis will yield horsepower data from the rod load measurement.

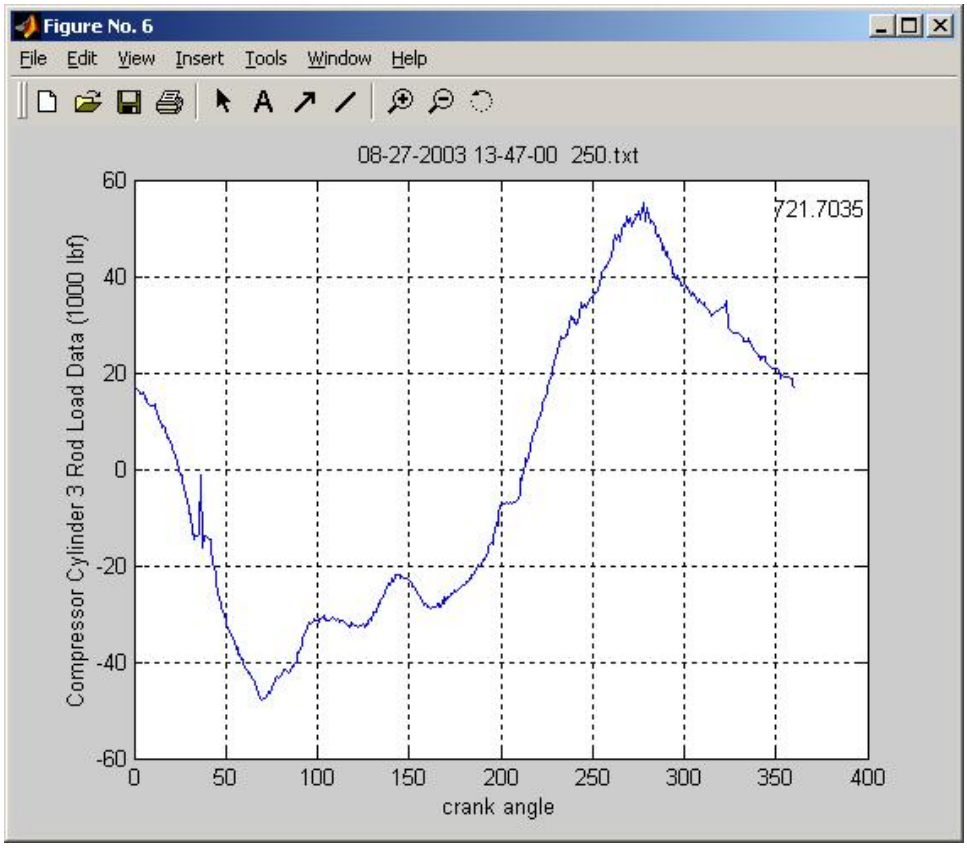

Figure 62. Typical Rod Load Variation Over One Revolution

Figure 63 shows the variation of compressor and engine horsepower indicated by the cylinder pressure transducers as a function of test record number (index). It will be seen that the indicated compressor power remains rather constant over the day's testing at an average of about 2375 HP, with a scatter range of about 50 HP about this average value. The indicated engine power appears to drop gradually during the day from an initial average around 2275 HP to about 2225 HP. There is, again, a range of about 50 HP about the average, but the reducing trend in engine power, by 2 to 2.5% over the day, is clear. The measured engine power lying below compressor power on this engine reflects a long measurement channel attenuating fast changing signals.

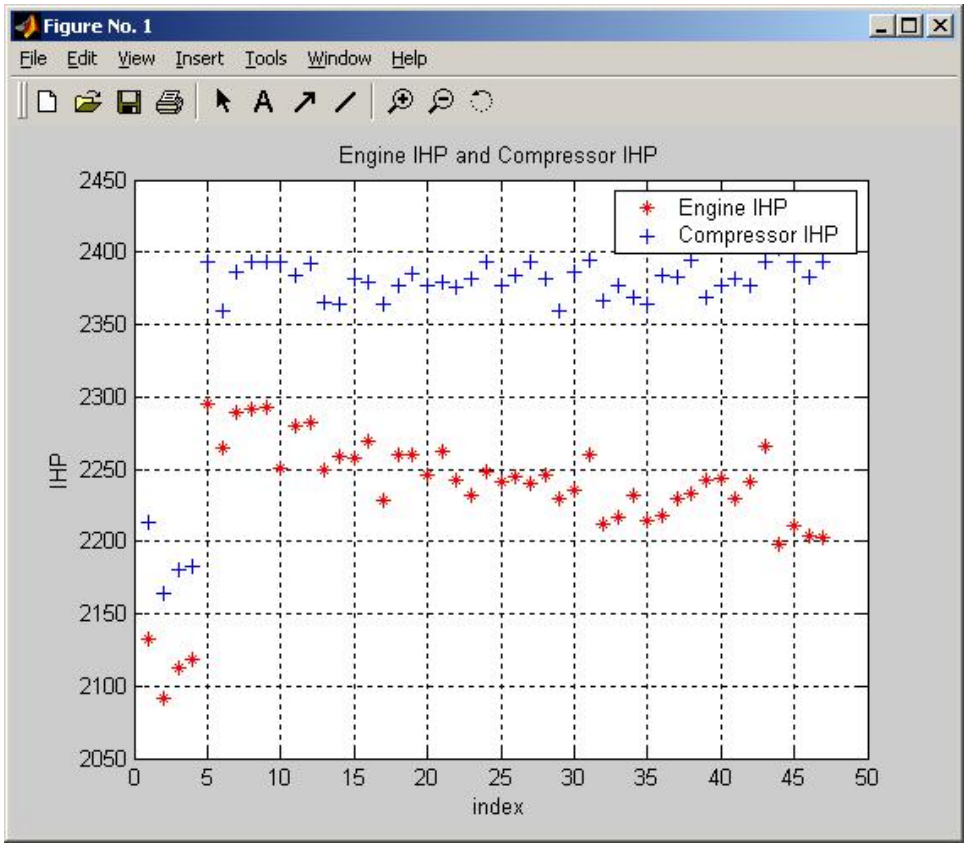

Figure 63. Indicated HP Over Test Day

A similar trend was seen in the data at the first test site (which will be discussed further below) - an apparent reduction in the losses between engine and compressor pistons over a 5- to 6-hour period following the start of the day's tests.

The first four data sets in Figure 63 show much lower power for both compressor and engine – reflecting the transients immediately following start-up.

Figure 64 shows how the ratio of indicated compressor power to indicated engine power varies over 47 test data sets. Discounting the first four part load conditions, the ratio runs from 104.1 to about 106.5 for test series 5 through 43. Test series 44 through 47 reflect some substantial changes in engine conditions (timing and air manifold pressure), and indicate a higher ratio of compressor to engine power (108 to 109%). Thus, the main body of data indicates an increase in the ratio of compressor to engine power - consistent with the reduction in engine power discussed with reference to Figure 63. The artifact of

higher compressor power than engine power has been discussed and explained previously.

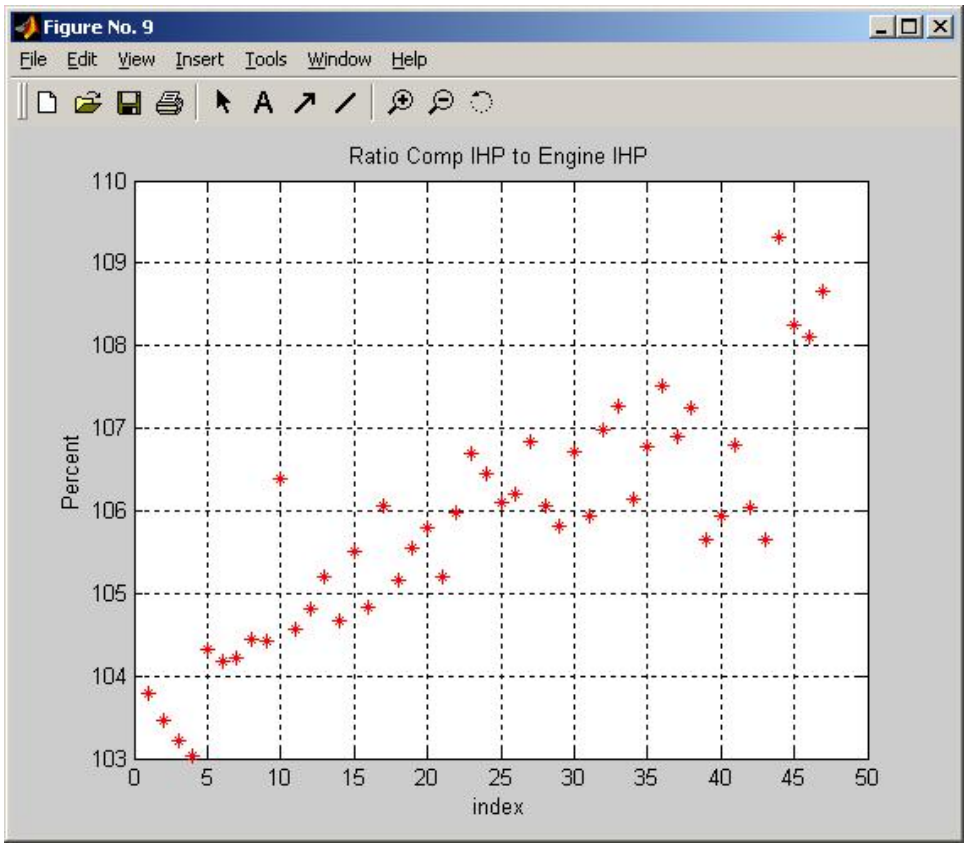

Figure 64. Ratio of Indicated Compressor HP to Engine HP during Test Day

Figure 65 shows how compression pressure in the power cylinder (defined for these data sets as the pressure 20 degrees before top dead center) varies over the test data series. The spread in compression pressure reflects a potential difference in trapped air mass in the different cylinders, and over the test series, the profile of compression pressure across the ten cylinders has a clear and repeatable pattern. With minor qualification, when one cylinder's compression pressure goes up or down, the compression pressure for all cylinders goes up or down by a similar amount. A reasonable interpretation is that trapped air in each cylinder remains linked to the other cylinders through the air and exhaust manifold flow dynamics, even when global behavior of the engine cylinders changes. This suggests the importance of these manifold flow dynamics in determining engine behavior as influenced by air balance across the cylinders.

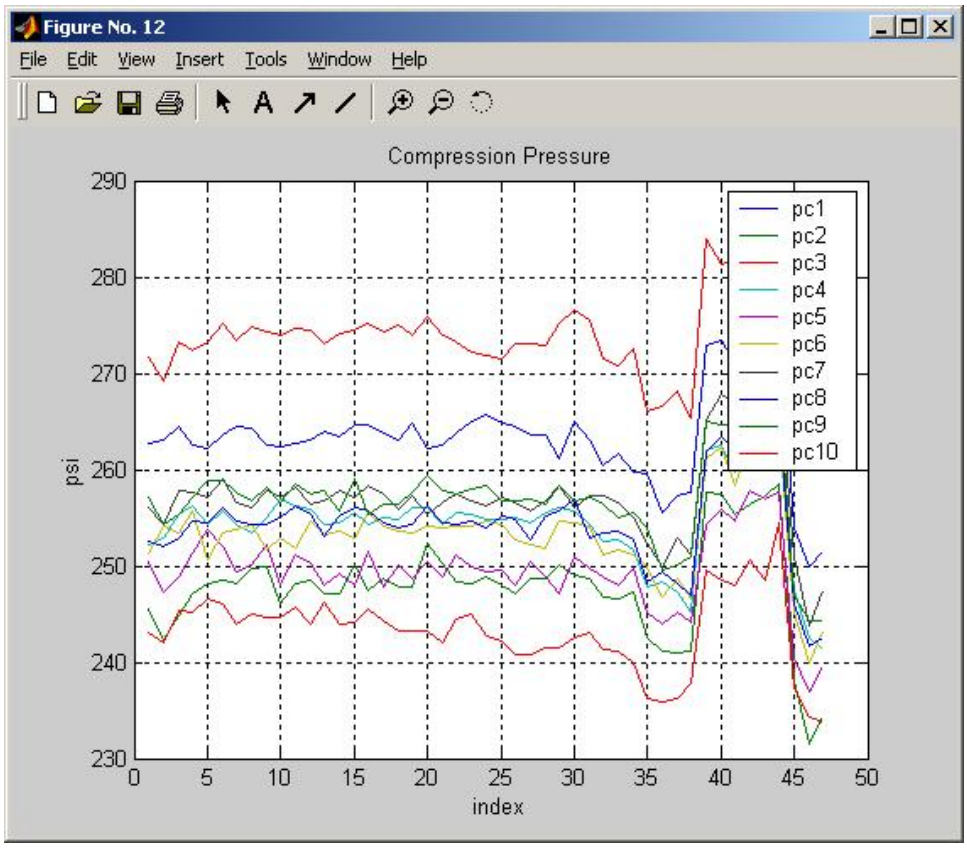

Figure 65. Power Cylinder Compression Pressure

Figure 66 shows how compressor thermal efficiency varies during the test series. Even including the first four part load data sets, the efficiency covers a rather small range from 85 to 86.8%. With these first four points removed, the thermal efficiency for the complete compressor has a range of one point from 85 to 86%. This is a very consistent data set, reflecting in part the consistency of conditions under which the compressor was operating. Consistency can also be seen between efficiencies calculated using differential indicated power based on the toes of the PV card, and the thermal efficiencies based on header conditions. In general, the header-based thermal efficiency is slightly lower than the cylinder pressure based efficiency, but only by typically 0.2 percentage points. As discussed relative to earlier figures, the first four data sets in this chart reflect start-up transients.

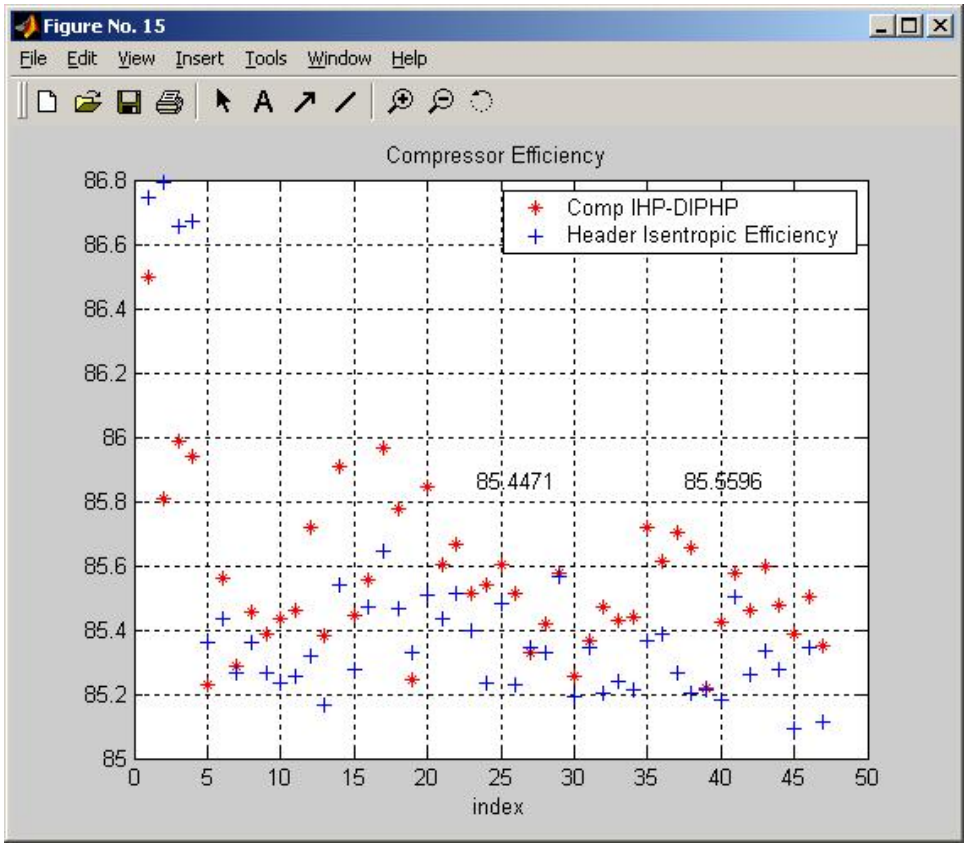

Figure 66. Compressor Efficiency

Figure 67 shows the waveform from the strain data capture module (SDCM) over eight engine revolutions. There is some variation from one revolution to the next, which could well correspond to the variation from cycle-to-cycle in combustion, as reflected in peak-firing pressure variations from cycle-to-cycle.

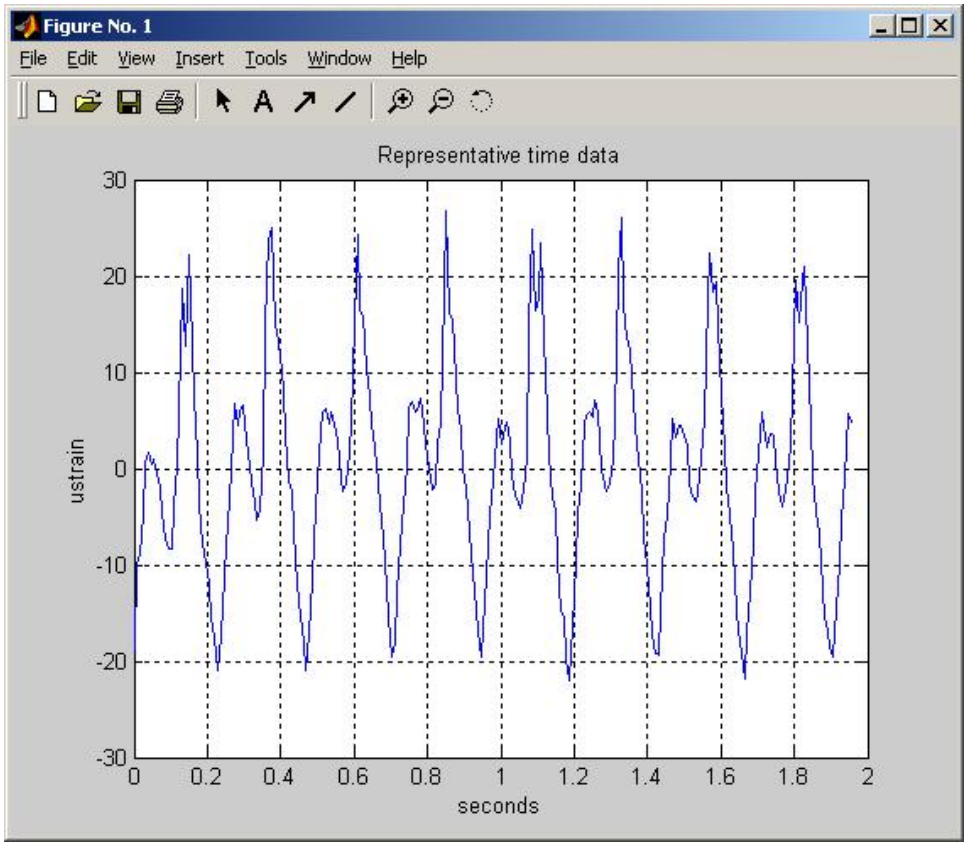

Figure 67. Typical Waveform (PC34)

Figure 68 shows the variation of strain data capture module output (expressed as peak-to-peak microstrain) throughout the approximately 7-hour test series. The start of the unit can be identified by sharp continuous increase from below 10 microstrain to above 50 microstrain at about 50 minutes, and the stop is identifiable by a drop with similar range at about 415 minutes. The SDCM is installed and starts recording data every five minutes. Then, the covers are installed and preparations are made to start the unit, which occurred in this case after about 50 minutes. The short-term variation after start-up shows a gradual increase from about 50 to 57 microstrain – probably reflecting the final speed increase and loading of the unit after start-up, which covered about 30 minutes. The level of microstrain generally decreased from 57 microstrain to about 50 over the next 250 minutes (4 hours) – matching the trend in steadily reducing engine load over this similar period, as reflected in Figure 63. In the last two hours of testing, some short-term timing and air manifold pressure changes were included in the testing, which may have resulted in the short-term increase in peak-to-peak microstrain seen at about 345

minutes in Figure 68. Data indicating how timing advance can increase crankshaft strain will be discussed again with reference to the second test on a GMW10 later in this report.

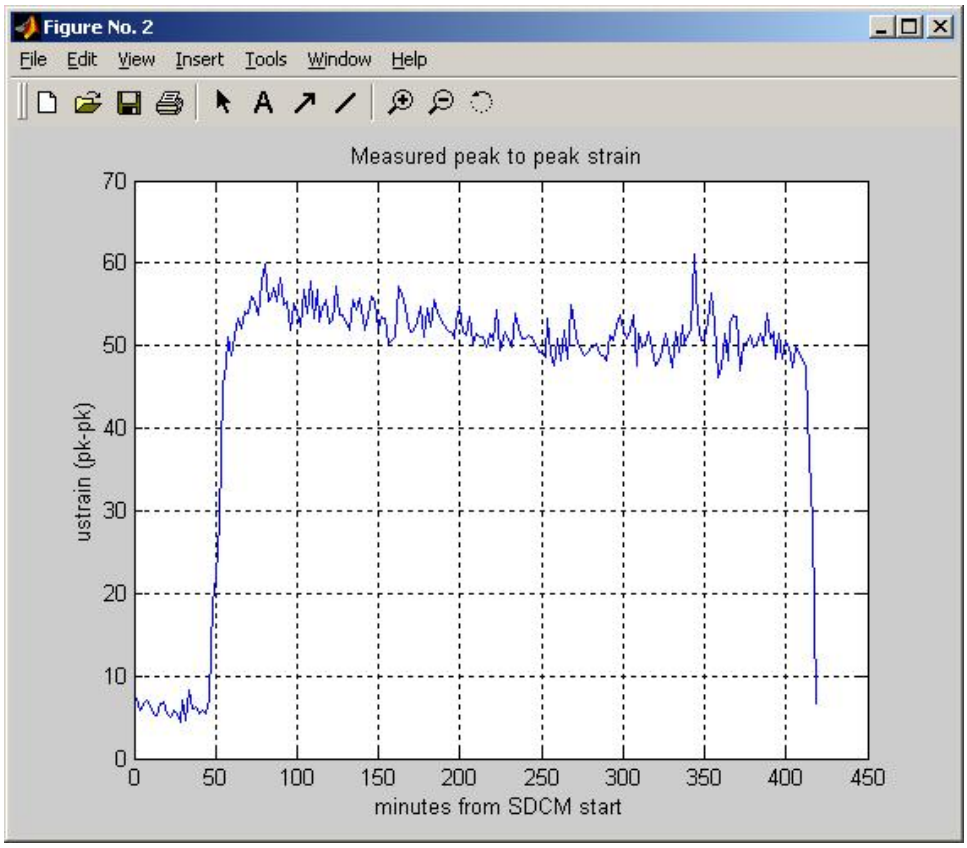

Figure 68. Peak-to-Peak Variation in Crankshaft Web Bending Stream (PC34)

The cycle-to-cycle variation is illustrated in 20 cycles of continuous pressure recording from power cylinder #2, presented in Figure 69. Clearly, this sort of cycle-to-cycle variation in power cylinder load could be the cause of the cycle-to-cycle variation in SDCM data, shown in Figure 67.

Figure 70 shows the power cylinder standard deviation throughout the day's testing, averaged across cylinders. Its nominal value is 58 PSI.

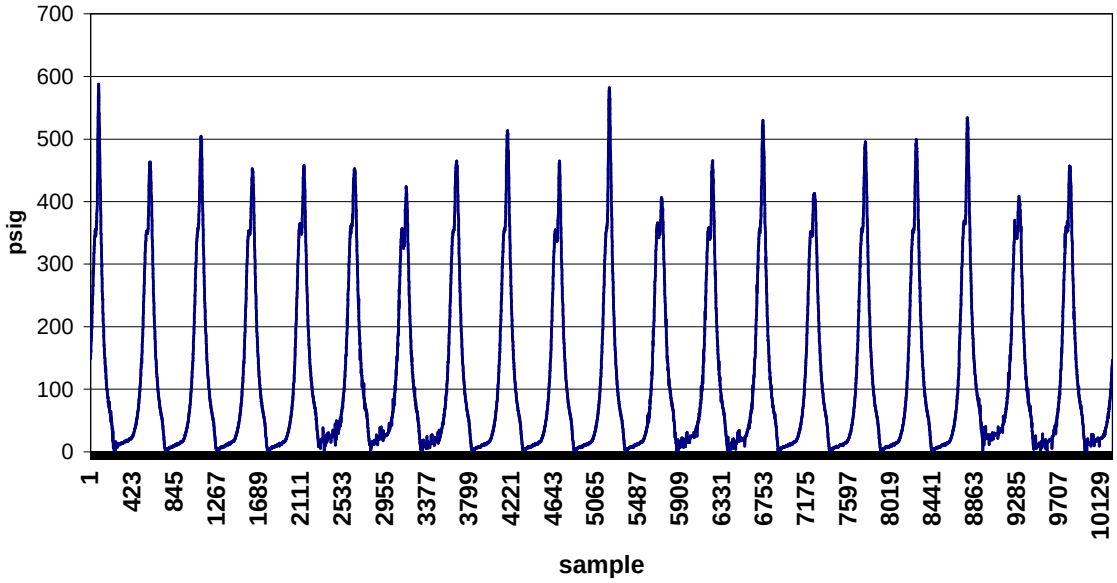

Figure 69. Typical 20 Successive Cycles – Power Cylinder #2

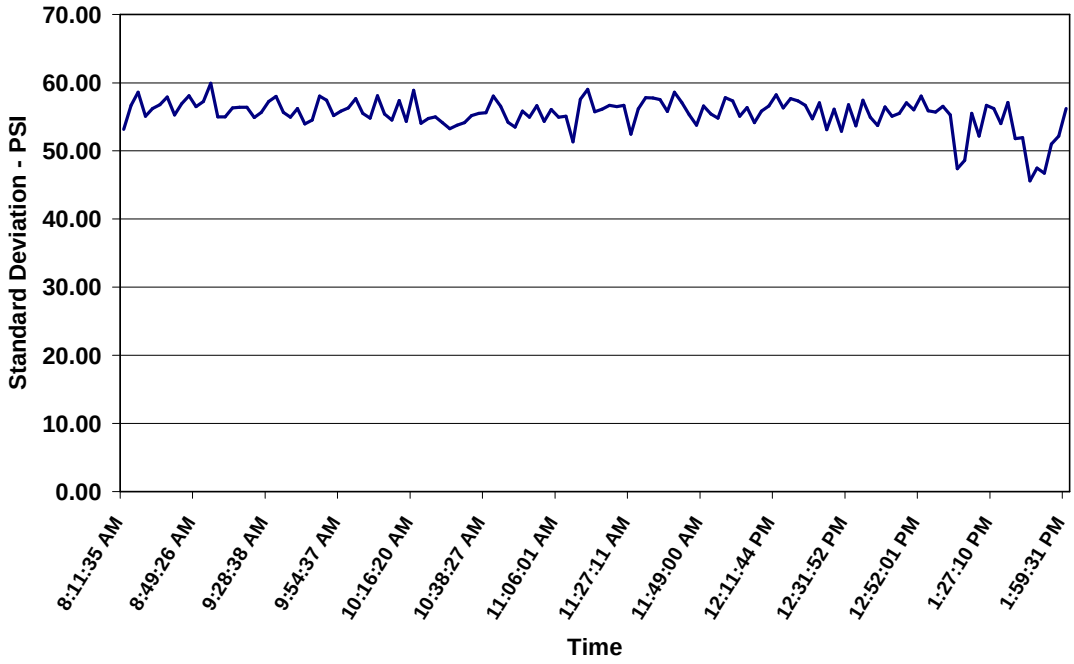

Figure 70. Average Engine Power Cylinder Deviations

Figure 71 shows the variation of fuel flow over about seven hours of testing. The fuel flow reduces in a manner qualitatively consistent with the reduction in engine horsepower over time during the tests. The magnitude of the reduction is from about 427 MMSCFD to 420 MMSCFD. This is slightly less than 2%. A potential reason for this reduction in fuel flow being lower than the 2 to 2.5% reduction in engine power is that engine brake thermal efficiency typically decreases with decreasing load on the engine. The sharp dip in fuel flow from 420 to 404 MMSCFD at about 1:00 PM corresponds to an advance in timing from 8.5 to 11 degrees at that time, and the spike up to 441 MMSCFD corresponds to a timing value of 6 degrees.

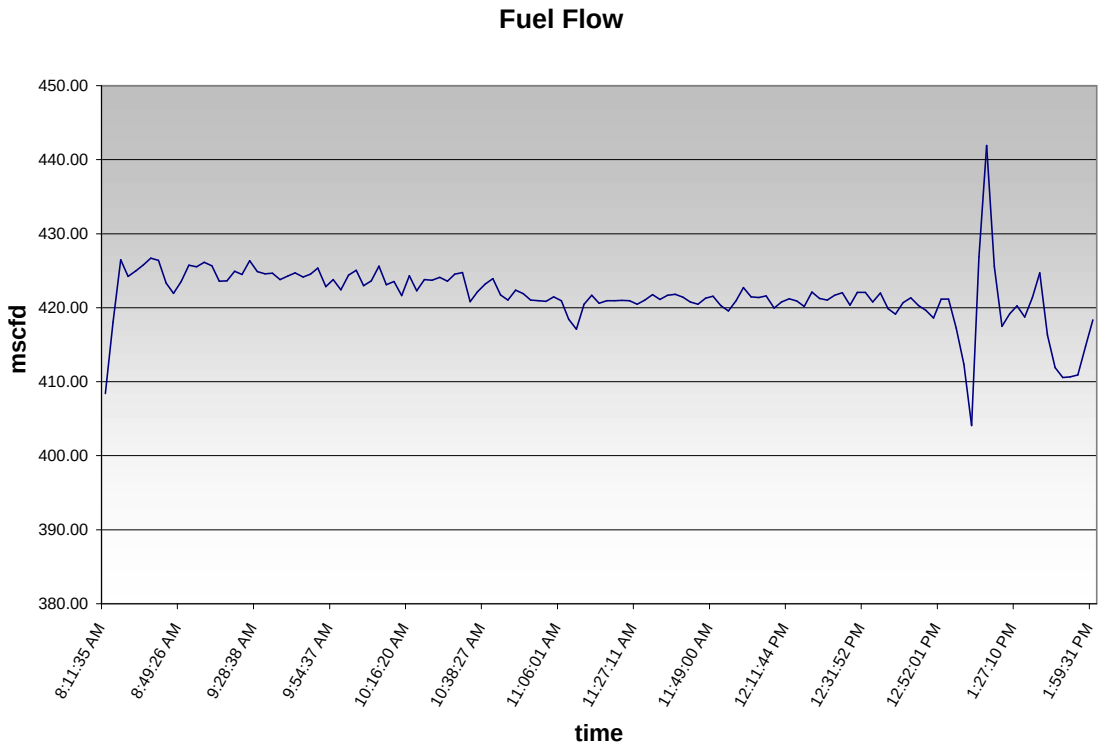

Figure 71. Engine Fuel Flow

Figure 72 shows how normalized NOx concentration and equivalence ratio vary with time throughout the testing. There is no significant change for several hours once the unit has started up. The NOx concentration values have all been normalized (not as brake specific NOx). The spike before start-up, of course, has no relevance. After that, for

most of the test, the NOx remained close to constant until about 1:00 PM when some timing change and air manifold pressure changes were made. These changes had a noticeable influence on NOx, and the NOx changes tracked the equivalence ratio changes.

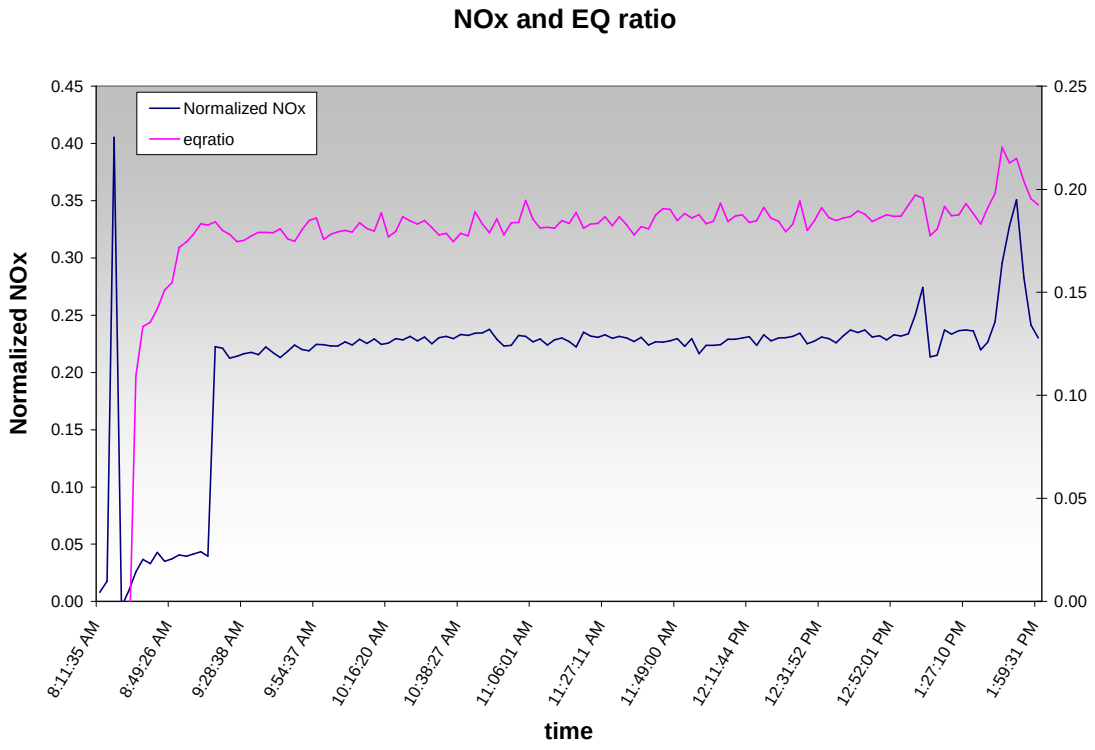

Figure 72. Normalized NOx Concentration and Equivalence Ratio

Figure 73 shows the variation in instantaneous spread in PFP across the ten cylinders and the spread in average PFP across the cylinders over a days testing. The instantaneous spread does not change much, except late in the day when timing and air manifold pressure changes were investigated. The high and consistent level of instantaneous spread directly reflects the cycle-to-cycle variability.

The spread in average PFP is typically around 30 PSI. It increases as a result of two changes in conditions. First, the engine was intentionally unbalanced around 10:00 AM, and returned to its previous balanced condition around 11:00 AM. Then, around 11:30

AM, the unit was balanced using CPR balancing (which seeks to equalize the ratio of PFP to compression pressure – termed the combustion pressure ratio, or CPR). The result of CPR balancing is to raise the spread in peak-firing pressure, because there is imbalance in compression pressure. However, the anticipated benefit of CPR balancing is to approach more closely a condition of equal air fuel ratio across the cylinders. It is further expected that this will have some benefit in reducing the tendency to detonate.

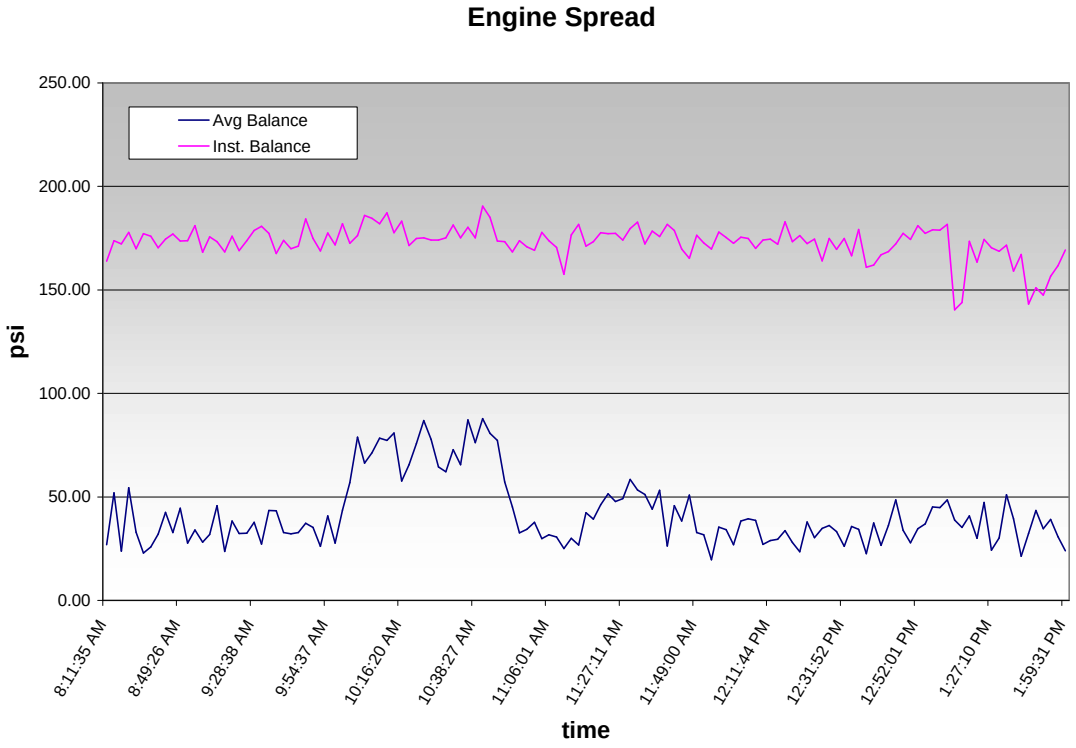

Figure 73. Engine PFP Spread

Figure 74 presents the evidence of accomplishment of CPR balancing. It shows how for all ten cylinders, the ratio of peak-firing pressure to compression pressure is effectively equal. The actual maximum tolerance on these CPR values is +/-2.5%, when they display as equal, as a result of the precision to which they are graphed.

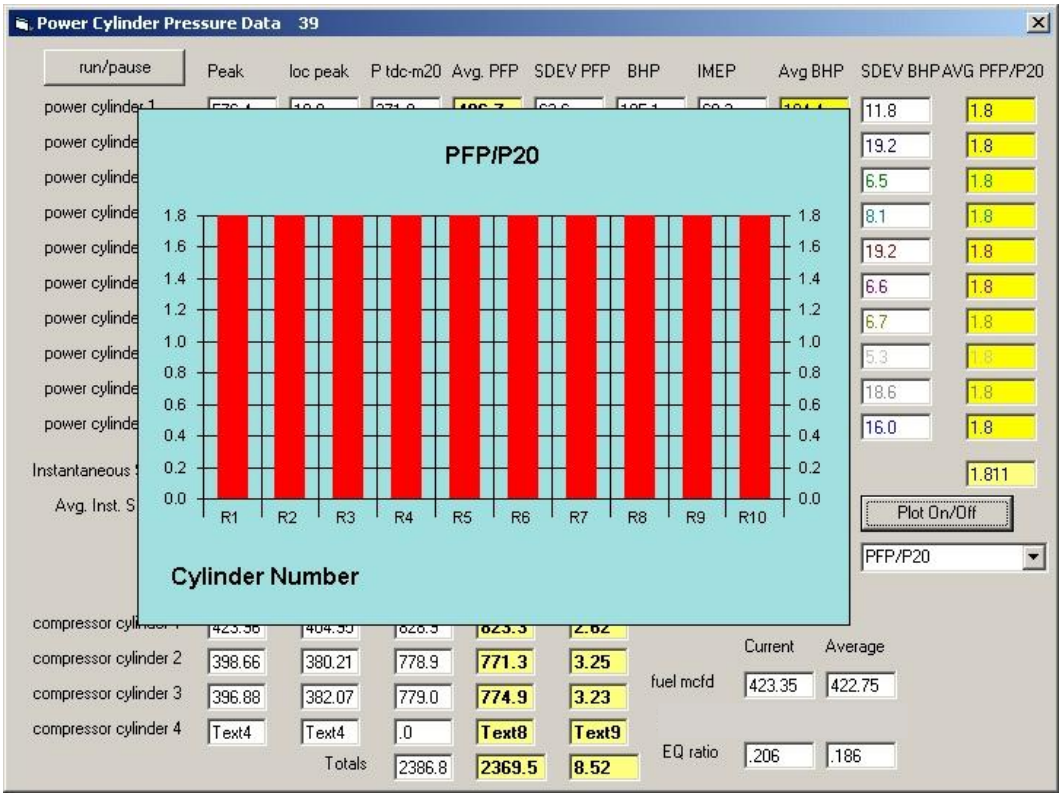

Figure 74. CPR Balancing Feasibility Demonstration

Figure 75 shows how average combustion pressure ratio (CPR) varies over the test series, and also how the standard deviation in CPR divided by average CPR falls under the condition when the engine is CPR balanced. There appears to be a small but consistent increase in CPR over the test from about 1.81 at 8:30 AM to about 1.84 at 12:50 PM. The Sdev (CPR)/avg CPR exhibits noticeable modulation, sample-to-sample, about a 4% average for most of the test. This is the COV of CPR across the cylinders. During CPR balancing, this quantity drops to under 2%, as would be expected, since bringing all CPR values close to the average CPR is the accomplished objective of CPR balancing!

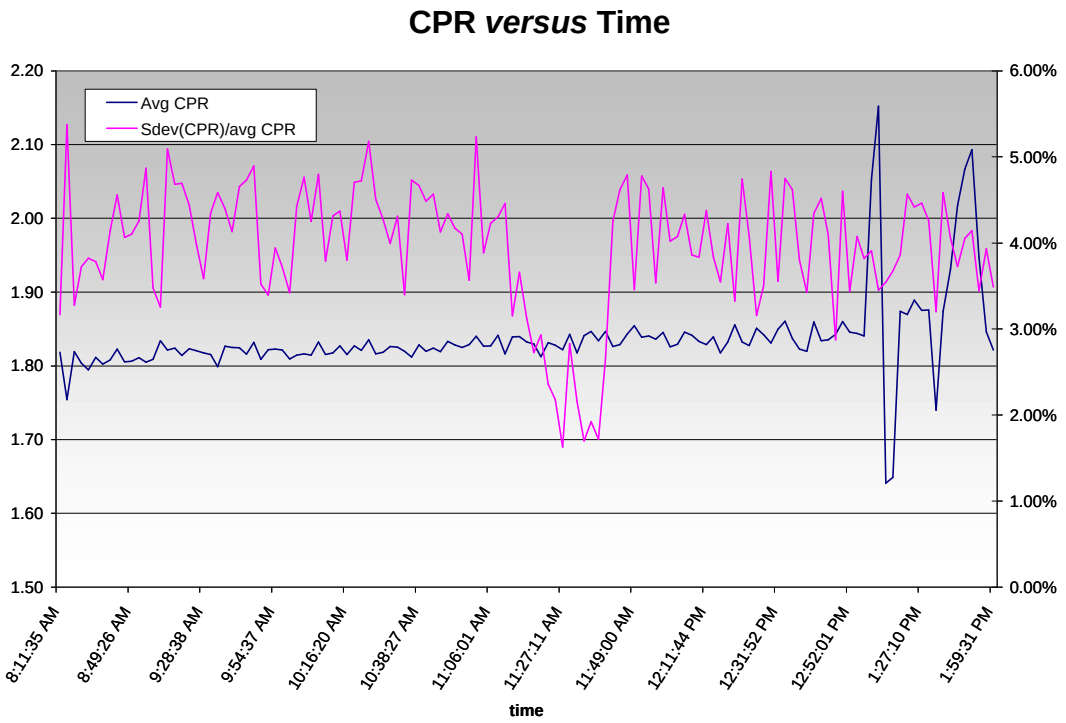

Figure 75. Ratio of PFP to Compression Pressure – Average and COV

Figure 76 shows how the heat rate of the engine (BTU/BHP-hr.) varies, where BHP-hr. represents the indicated cylinder energy. It also shows how the overall system efficiency (conversion of LHV fuel energy to useful compression energy) varies over the test. The heat rate is low for this recently converted engine, lying in the range 6900 to 7000 BTU/BHP-hr. for most of the test. The overall system efficiency is about 30.0%, once the mechanical efficiency has reached its asymptotic condition. With the timing advance towards the end of the test, the heat rate drops to 6620 BTU/HP-hr., and the overall system efficiency increases to almost 31.4%, a high number for an integral engine compressor. These numbers of 30.0 to 31.3% overall system efficiency set a challenging benchmark for the industry. (It will be noted some of these numbers have changed from an earlier quarterly report. The earlier calculations did not include the effect of compressor mechanical efficiency in calculating HP for use in the heat rate.) For reference purposes, overall system efficiency is the product of engine brake thermal efficiency, compressor mechanical efficiency, and compressor thermal efficiency.

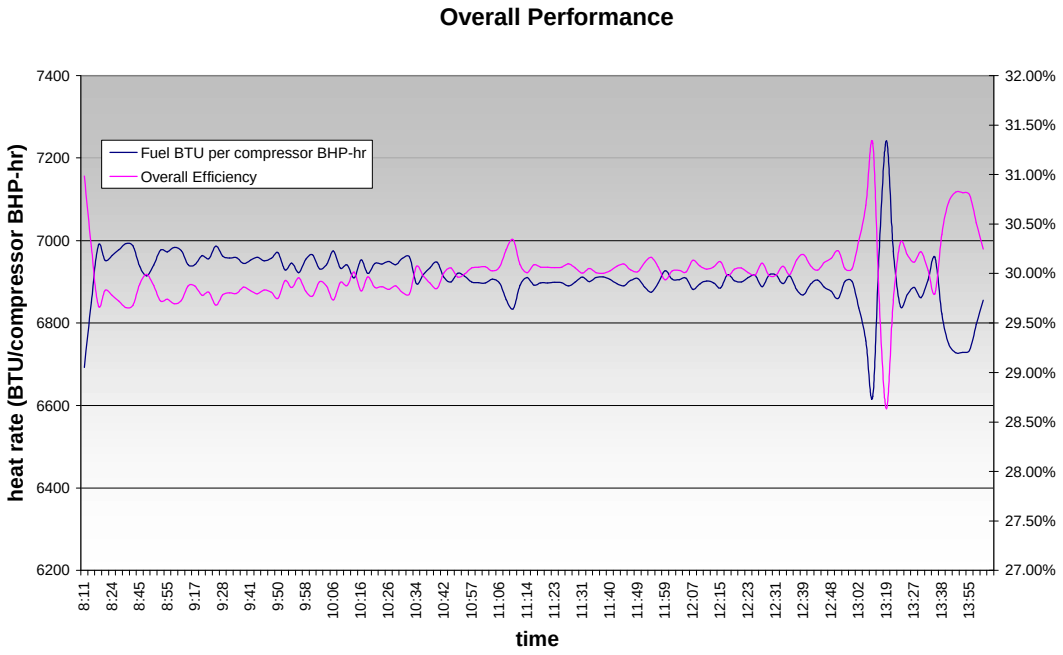

Figure 76. System Performance

4.4 SUPPLEMENTARY ANALYSIS OF DATA FROM GMW10 TEST 1

Table 3 summarizes the data obtained during the GMW10 Test 1 at Sour Lake (Williams-Transco, Station 40). The following addresses some additional items of data analysis from these tests.

Table 3. Summary of Sour Lake Data Analysis Results

Dynamic Variation Range for Air Manifold Pressure	17 to 22% of Average
Dynamic Variation Range for Exhaust Manifold Pressure	48 to 70%
Rod Load Range	-47,000 lb. to +55,000 lb.
Typical Compression Power during Tests	2375 HP
Compressor Thermal Efficiency	85% to 86%
Engine Heat Rate	6900 to 7000
Increase in Ratio of Compressor to Engine Power during 5 Hours of Tests - As an Apparent Increase in System Mechanical Efficiency as Oil Heats Up	2 to 2.5%
Corresponding Decrease in Fuel Flow	1.5%
Corresponding Decrease in Heat Rate	1.25%
Heat Rate Reduction by Advancing Timing from 8.5 to 11 Degrees BTDC	Reduction from 6900 to 6620 BTU/HP-Hr.
System Thermal Efficiency with "As Found" Timing	30%
System Thermal Efficiency with 11 Degrees Timing	31.3%
Typical Range of Peak-Firing Pressure in 20 Successive Cycles	401 Minimum to 588 Maximum (PC2)
Range of Crankshaft Dynamic Strain during Tests	Between 50 and 60 Microstrain Peak-to-Peak
Typical Spread in Power Cylinder Compression Pressure Over 10 Cylinders	From 244 to 275 PSI
Typical Spread in Average Peak-Firing Pressure Across 10 Power Cylinders	35 PSI
Typical Instantaneous Spread	175 PSI

4.4.1 Relating Heat Rate, Efficiency, and NOx Emissions to Timing and Air Manifold Pressure

Figures 77 and 78 show how timing and air manifold pressure (AMP) influence heat rate and system thermal efficiency. The points at 8.5° before top dead center (BTDC) for timing and at 12.5 inches of Mercury (Hg) for AMP represent the nominal condition (resulting in 7250 BTU/HP-hr. and 29.8% efficiency). The points at higher and lower timing (6° BTDC, 11° BTDC) and at higher and lower AMP (10 inches, 14 inches Hg) represent independent perturbations in timing and AMP about this nominal condition. They quantify how heat rate falls as timing is increased and how heat rate rises as AMP is increased (making the combustion leaner). Figures 79 and 80 quantify how NOx follows opposite trends to the heat rate. This opposing trend is sometimes referred to as the NOx-

heat rate trade-off. Figure 80 presents a plot of heat rate as a function of NOx with all the data from Figures 76 through 79 on it. Figure 81 shows, for example, that heat rate can be substantially reduced from 7250 to 6950, with a 20% NOx increase, by an increase in timing to 11° BTDC.

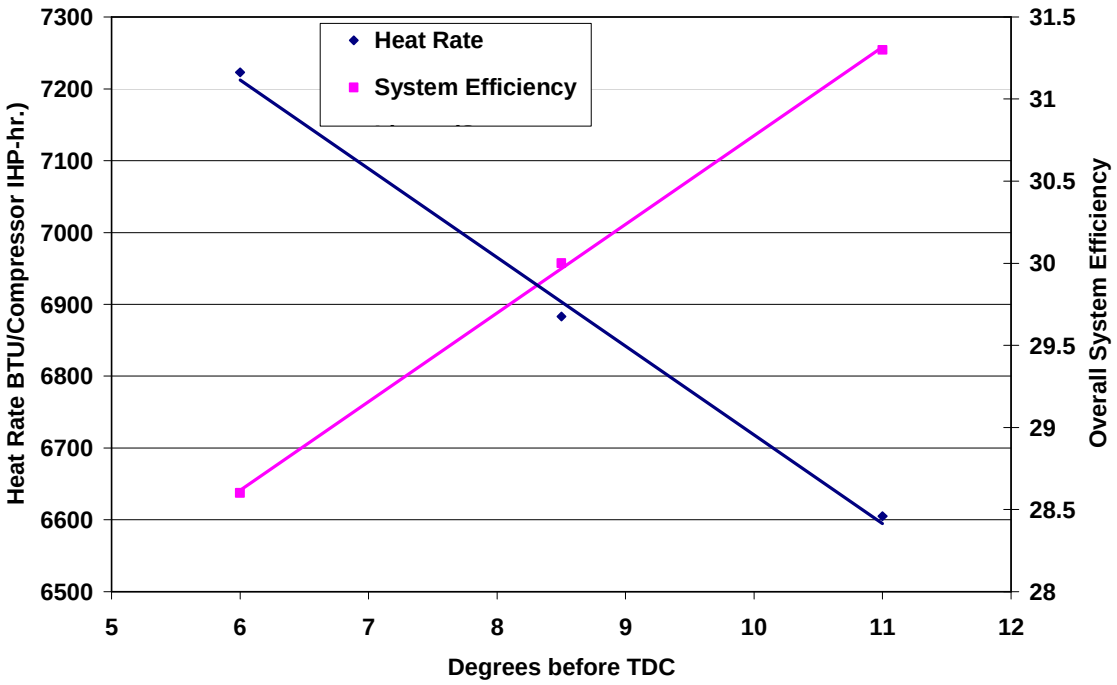

Figure 77. Heat Rate and System Efficiency as a Function of Timing (use for Relative Analysis Only)

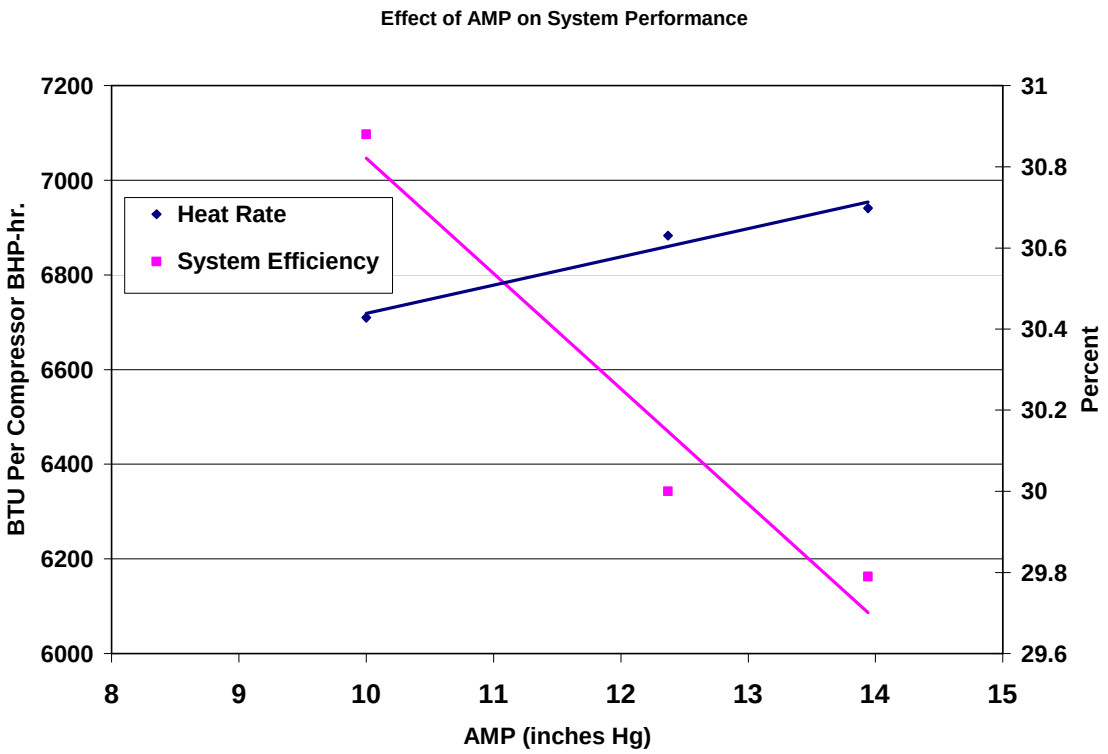

Figure 78. Heat Rate and System Efficiency as a Function of Air Manifold Pressure

It is noted that the result of air manifold pressure changes is to change equivalence ratio, and that other changes in conditions such as ambient temperature may cause equivalence ratio to change. For this reason, there are benefits to be expected from implementing equivalence ratio control. This would need to be coupled with timing control in response to detonation detection. Plans for implementing these controls using an equivalence ratio sensor and detonation detection will be discussed subsequently.

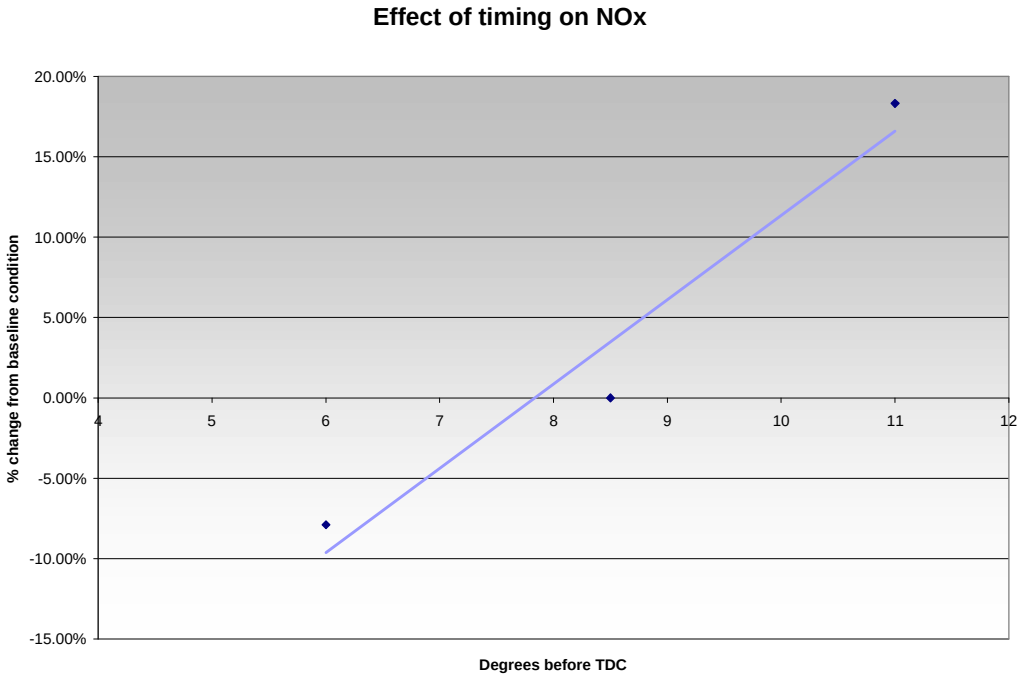

Figure 79. Change in NOx as a Function of Timing

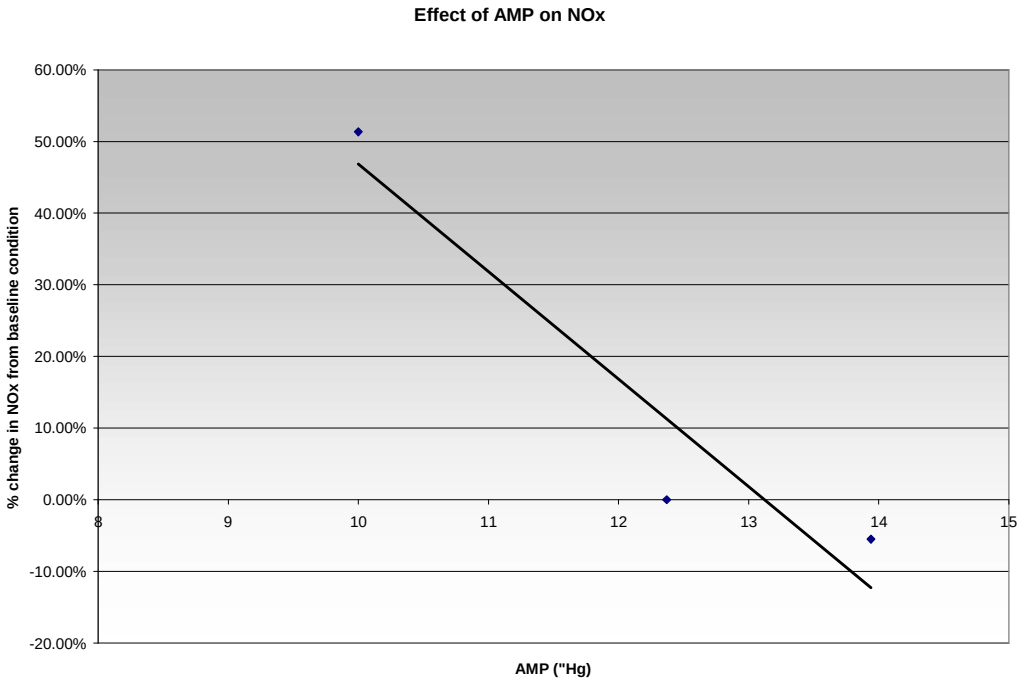

Figure 80. Change in NOx as a Function of Air Manifold Pressure

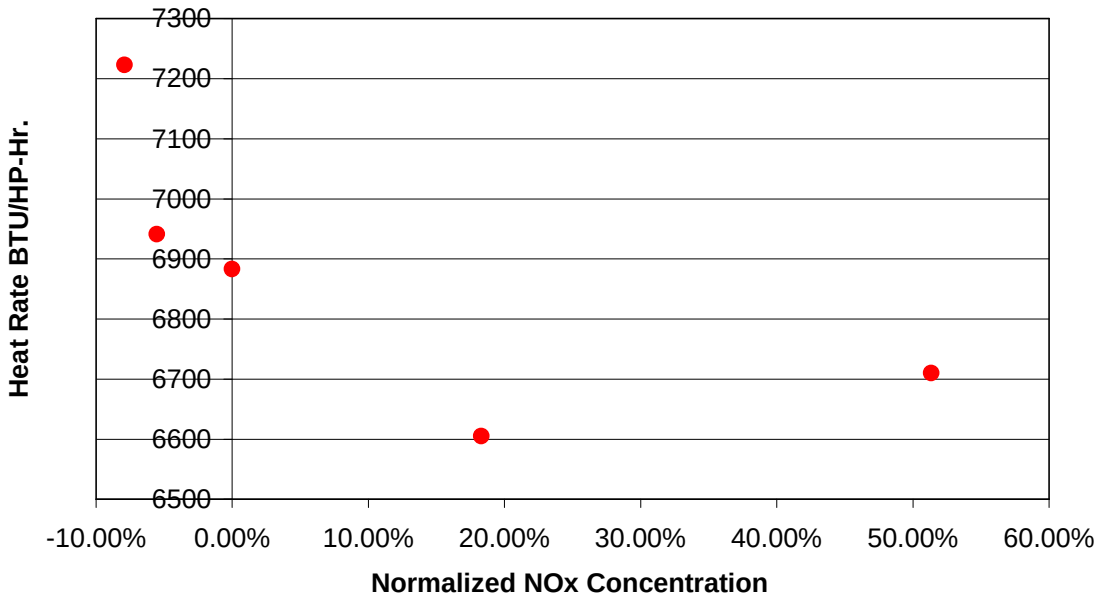

Figure 81. Trade-off between Head Rate and NOx (Relative Analysis Only)

4.4.2 Relating Rod Load Monitor Output to Cylinder-Indicated Power

During the Sour Lake tests, data was obtained on compressor cylinder #3 with cylinder pressure and with the rod load monitor (RLM). However, when compared, the ratio between cylinder-pressure-indicated horsepower and the horsepower determined from the RLM varied strongly during the day. The sensitivity of the RLM appeared to be changing during the day, and since it has already been observed that there is an increase in oil temperature over the day, a temperature effect was suspected. Tests in the laboratory following the Sour Lake tests confirmed a distinct increase in the ratio of volts per 1000 microstrain with temperature, as shown in Figure 82. Based on this, an effort was made to correct the data. Figure 83 presents the variation of oil inlet and outlet temperature during the test day, and the increase in outlet temperature is clear. As the best information available on temperature variation, the outlet temperature data of Figure 83 has been combined with the sensitivity correction of Figure 82, as expressed in the equation on the chart ($y = 0.0016x + 0.8571$, where y is volts/1000 microstrain and x

is temperature), to come up with a corrected horsepower based on the RLM. The correction is not perfect, because the oil temperature would not be expected to provide a precise measurement of rod temperature.

The result is shown two ways. Figure 84 presents the horsepower determined from cylinder pressure (compressor IHP) and from the RLM (corrected), as they varied during the day. Figure 85 presents the ratio of the two horsepowers. Clearly, the correction is imperfect, and is not a long term satisfactory way to determine horsepower from the rod load measurement. Based on these results, the component in question in the RLM has been replaced and the sensitivity now does not vary with temperature. We plan to test the refined RLM on the return to El Paso Station 823.

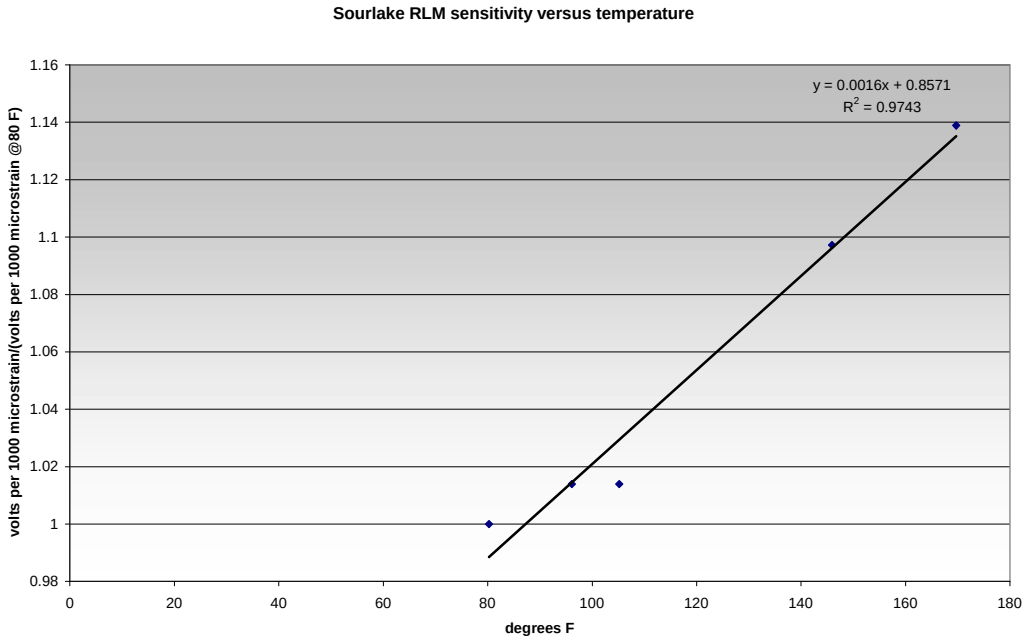

Figure 82. Post Test RLM Temperature Sensitivity Measurements

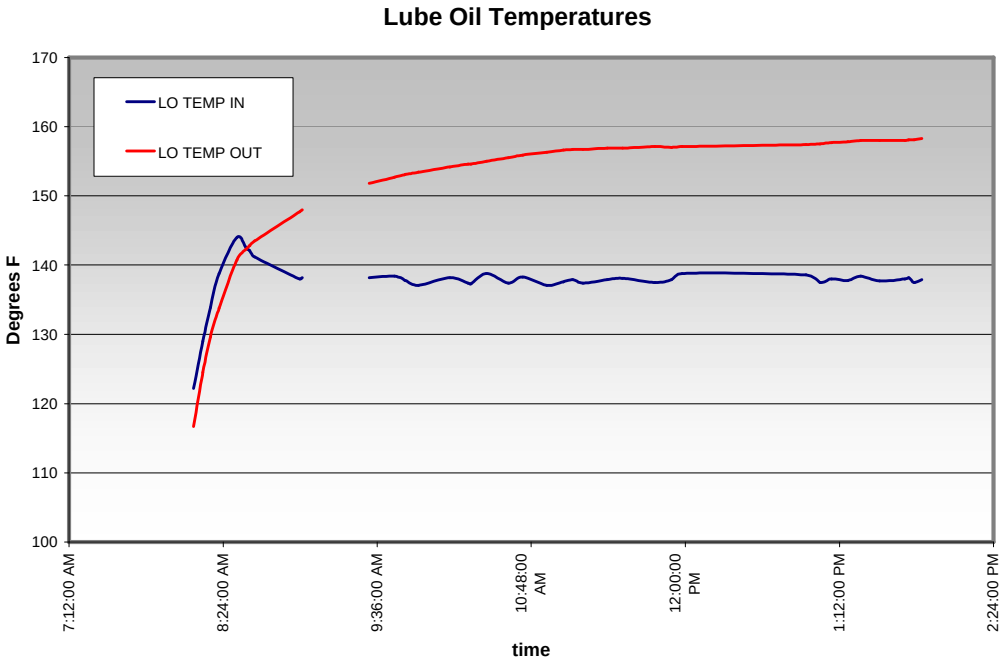

Figure 83. Variation of Oil Inlet and Outlet Temperatures

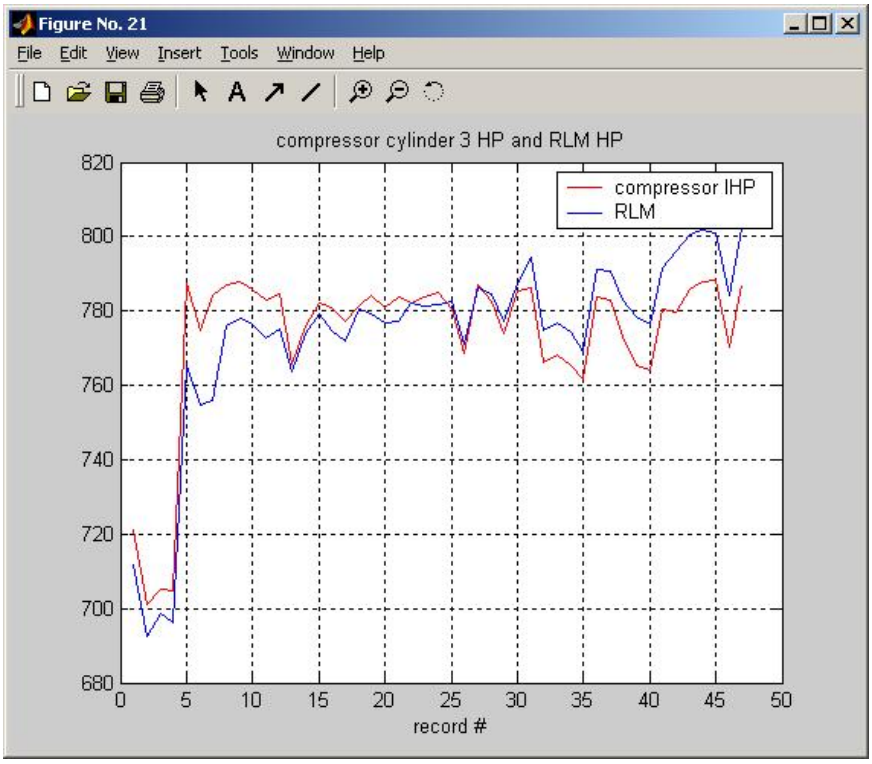

Figure 84. Compressor IHP and RLM HP

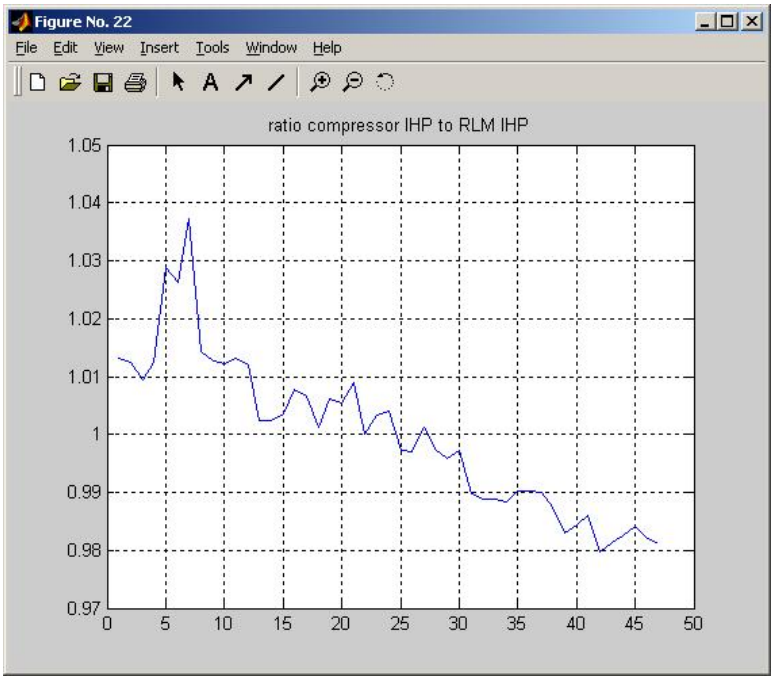

Figure 85. Residual Ratio Compressor IHP to RLM HP

4.4.3 Influence of Load and Load Step

During a second day's testing, the influence of load step was investigated. The first objective was to investigate how load step might influence brake thermal efficiency or heat rate when the unit was otherwise operating at the same horsepower. Some test results on a preceding GMRC/PRCI project had suggested that the way the compressor cylinder load is distributed along the shaft might influence the power cylinder behavior to a small extent under part load. A second objective was to investigate how load on the engine might influence compression pressure and rod load data.

These objectives encountered mixed success. By combining a change in load step with pinching the suction line to increase ratio, it should in principle be possible to achieve the same horsepower with a different load step. However, the efforts to readjust the horsepower back to the value before the load step change were not successful – a series of operational problems and unit trips showed that this was not readily attainable – at least under the prevailing pipeline conditions. Thus, the first objective could not be met during these tests.

The change in load step prior to efforts to change suction pressure did however accomplish a change in horsepower, as would be expected, and data was obtained on how compressor load influences compression pressure in the power cylinder and the relationship of rod load monitor to indicated horsepower. Figure 86 shows the variation of horsepower during the tests. Approximately 20% increase in compressor power was obtained over the test range. Figure 87 shows the corresponding variation in compression pressure in the ten power cylinders. They all track each other and appear to maintain a similar separation. Figure 88 confirms this by plotting the difference from cylinder #1 compression pressure for all the other cylinders. In spite of substantial absolute variation in compression pressure (over 30 PSI) the difference of all cylinders from cylinder #1 shows at most a 5 to 6 PSI variation. This is further indication of a consistent cylinder-to-cylinder variation in the trapped mass of air, which is a basis for a separately proposed air balance investigation.

Figure 89 shows the change in indicated cylinder #3 horsepower and the corresponding ratio of indicated horsepower to RLM horsepower (this time without temperature correction). The qualitative ability of the RLM to track horsepower is clearly demonstrated. However, the need for temperature correction is re-emphasized by this data. The uncorrected data in Figure 89 shows much wider variation of the horsepower ratio than the corrected data for the previous day in Figure 85.

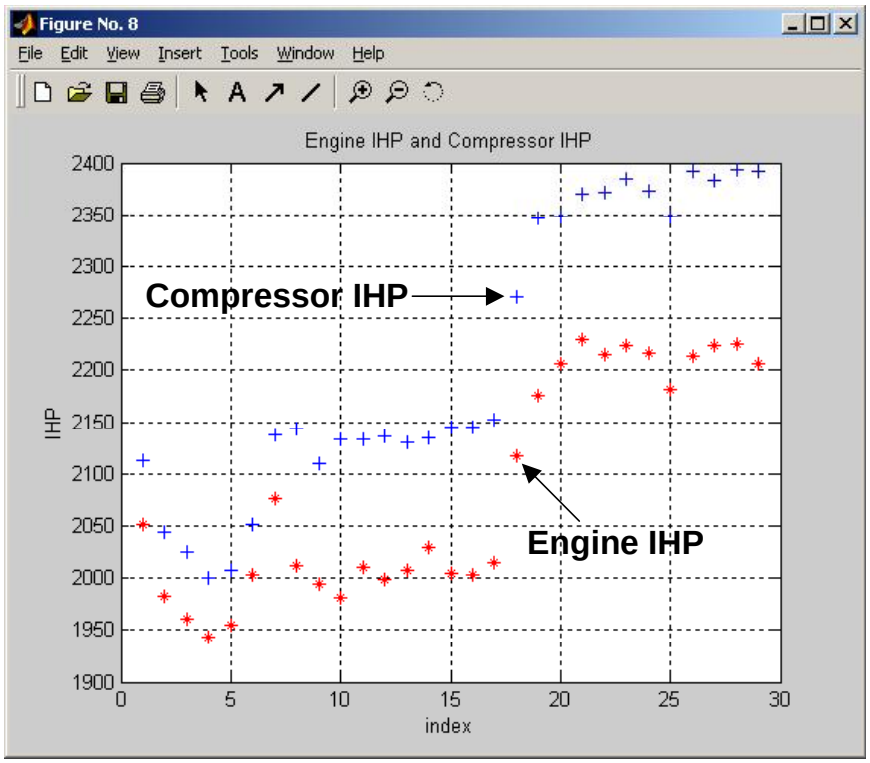

Figure 86. Variation in Power during Second Day's Testing

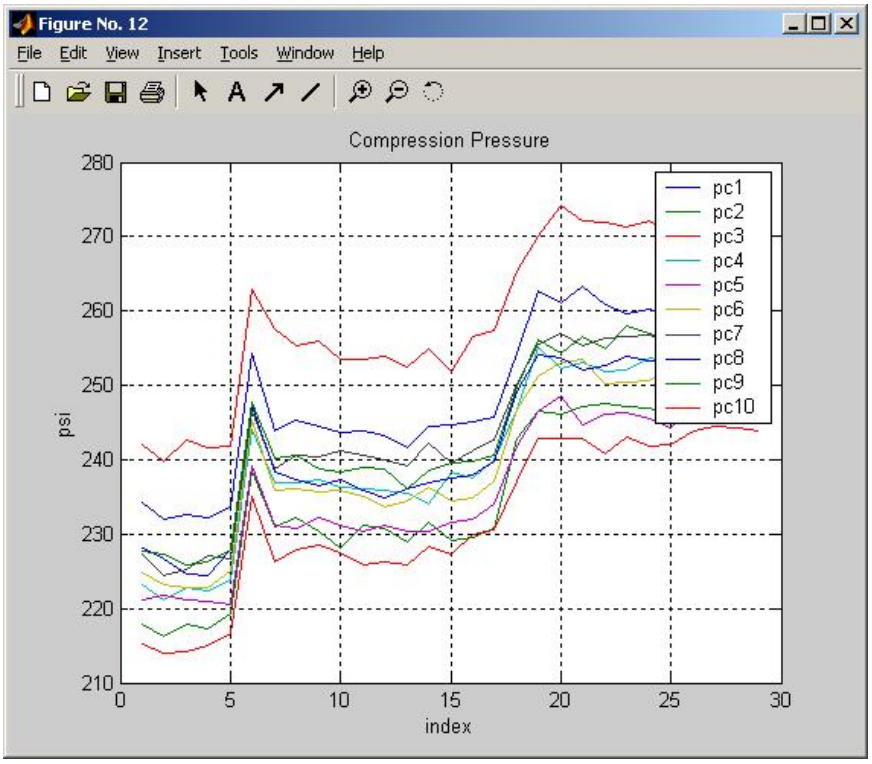

Figure 87. Compression Pressure for 10 Power Cylinders during Second Day's Testing

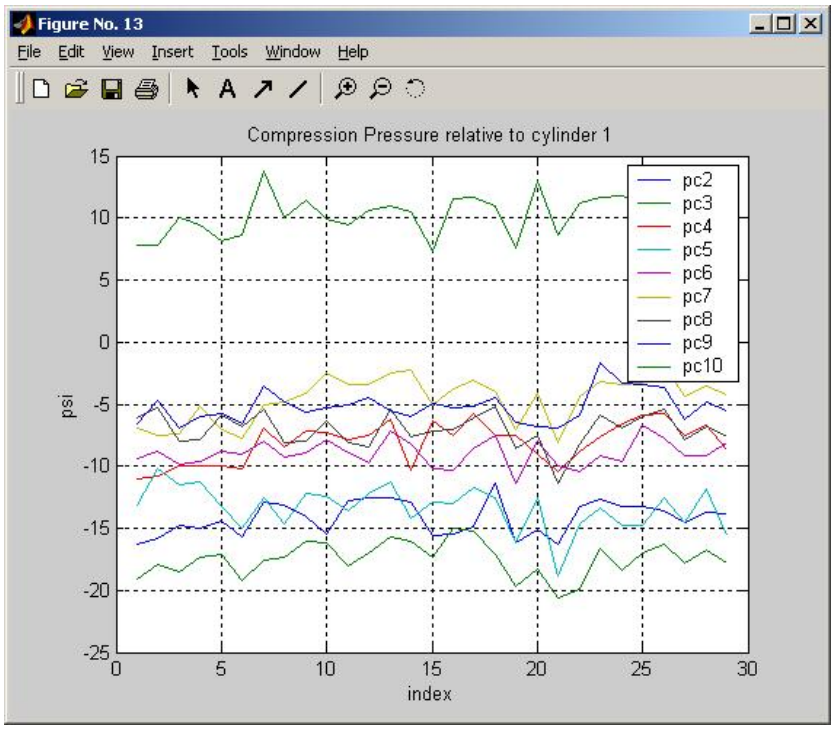

Figure 88. Compression Pressure Relative to Cylinder #1 for Second Day's Testing

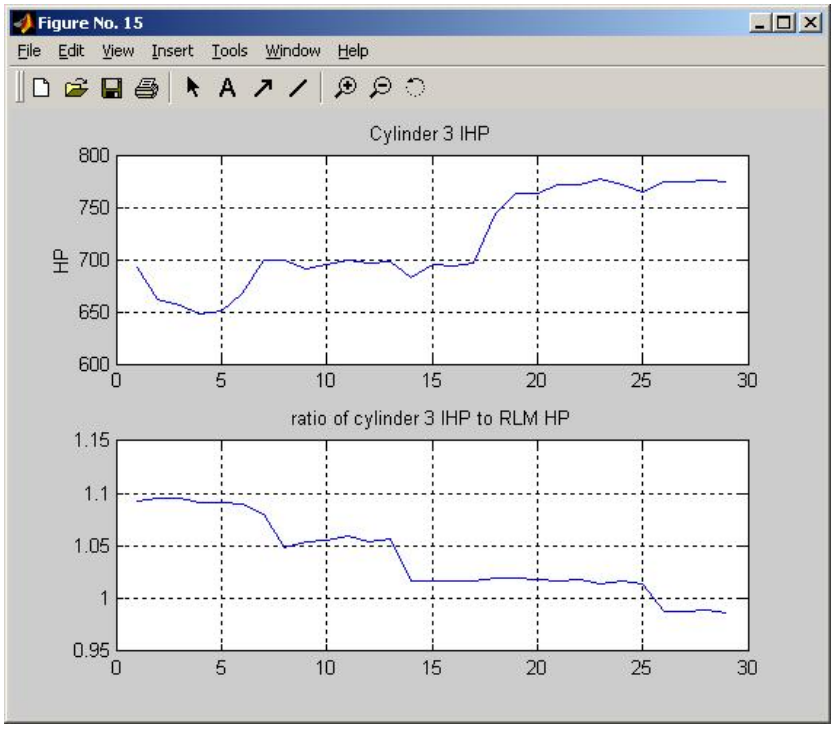

Figure 89. Cylinder Indicated HP and Ratio of IHP to Rod Load HP (without Temperature Correction)

4.5 OPERATIONAL OPTIMIZATION – OBJECTIVES AND ANTICIPATED BENEFITS

Based on the preceding analysis of data from the first and second test sites, the following potential methods for optimizing operation have been identified:

- Combustion Balancing to Equalize Combustion Pressure Ratio (CPR Balancing)
- Advancing Timing Subject to Knock Detection and Avoidance
- Closed-Loop Control of Global Equivalence Ratio
- Starting the Engine with Preheated Oil
- Running with Hotter Oil
- Manifold Redesign and Retrofit to Reduce Air Imbalance
- High-Pressure Fuel Injection on Turbocharged Engines
- Maintaining Unit Load by Monitoring Compressor Rod Load

The anticipated benefits of CPR balancing are first a reduction in the tendency to detonate. Because combustion and trapped air fuel ratio are likely to be equalized, all cylinders should approach a condition where extremes of richness and leanness are minimized. In addition, if PFP balancing reduces fuel consumption and NOx, then CPR balancing should produce further reductions. However, since not all engines respond that much to balancing of any kind, the fuel and NOx benefits may be small. The feasibility and benefits of CPR balancing have been evaluated in the most recent round of operational optimization tests. Efforts at a second test on a GMW10 showed no consistent benefit in NOx or heat rate reduction in response to either of PFP or CPR balancing. The tendency to reduce detonation was qualitatively observed, but has not yet been documented.

Advanced timing has been shown to reduce heat rate considerably, with some NOx penalty. For those operating companies where this combination of effects achieved by advancing timing is desired, the additional concern arises that detonation tends to become more likely as timing is advanced. Thus, a method of advance timing while protecting

against detonation is desirable. Detonation detectors are now available on the market and their effectiveness at discriminating detonation has been evaluated in the most recent round of operational optimization tests at Williams Station 60. The specific detonation detectors evaluated were loaned by Metrix.

Controlling waste-gate to maintain a set point in global equivalence ratio, rather than simply maintaining a waste-gate setting, ensures much more consistent engine operation as conditions change. Of course, this also depends on detonation avoidance. The benefits should be more consistency in NOx, since the range of air manifold pressure investigated on the GMW10 had as much as 50% influence on NOx. The use of closed-loop control of the turbocharger waste-gate to maintain a global equivalence will be evaluated in the next round of operational optimization tests at El Paso's Station 823. Timing and air manifold pressure control are discussed in more detail in the section below.

Circumstantial evidence exists for the influence of oil temperature on the efficiency of mechanical power transmission from power cylinders to compressor cylinders. Further critical testing is planned in which oil temperature will be actively changed at El Paso's Station 823. If possible, after the oil has heated up in order to confirm that the phenomenon observed is not simply related to time from starting a test to stop, a restart will be performed.

Calculations show the potential value of eliminating air imbalance. This will be evaluated under additional tasks. As part of the evaluation, a modified manifold(s) will be designed to achieve reduced or eliminated air imbalance. The new manifold will be built and tested if the predicted benefits show a satisfactory cost-benefits relationship for commercial deployment.

4.5.1 Plans for Spark Timing and Air Fuel Ratio Control

4.5.1.1 AMP Automatic Control System Options

There are a few options for demonstrating a simple AMP or air/fuel ratio control system. The most common approach is to control AMP as a linear function of Fuel Header Pressure (FHP). With this approach, there may be several functions that relate to each engine speed that the engine is operated at. A more advanced version of this technique is to implement an algorithm to correct the AMP setting, such that only one function exists at all operating conditions, and requires a few additional measurements and empirical data-based look-up table for speed related coefficients. A more advanced system would involve additional measurements and a model-based algorithm that estimates the trapped fuel/air equivalence ratio for which control is based. This system, however, is complex and expensive, and would require different programming for different engine models and configurations.

Since the purpose of this effort is to demonstrate a low-cost, simple control system, a single variable approach would be desirable. The original technique for setting AMP involves a manual adjustment with no automatic feedback. Therefore, the simplest approach is to install a single input PID controller that would modulate the waste-gate to control to a user input setting of either AMP or exhaust equivalence ratio. The NGK-Locke NOx/O_2 sensor, being used for data acquisition, has a 0-5v signal that has been calibrated to exhaust equivalence ratio. This signal could be connected to the PID controller to allow automatic closed-loop control of fuel-air equivalence ratio. Although very simple, this approach should offer significant improvement over a manual setting and compensate for varying ambient conditions until the extreme case where the engine may become boost-limited.

The demonstration unit will be a simple PID controller coupled to an I/P, with only the O_2 sensor (or AMP) feedback. A Honeywell UDC 3000 Universal Digital Controller has been used in the labs at SwRI for similar closed-loop controls. This controller would be the simplest approach to provide an automatic air/fuel ratio control system. A linear

calibration can be programmed into this unit to turn the voltage signal from the O_2 sensor into exhaust equivalence ratio engineering units. The controller has both manual and automatic modes. In manual mode, the unit will work almost exactly as turning the regulator knob on the control panel in the current setup. Therefore, the operators should have some comfort in its use. In automatic mode, a standard PID loop will adjust the 4-20 mAmp output to an I/P to move the waste-gate until the user entered equivalence ratio is achieved. SwRI would bring the Honeywell controller, O_2 sensor, and I/P for this demonstration.

For long-term permanent installation, a controller such as the Woodward 723 would likely be proposed. The 723 is used for engine control in compressor stations and, therefore, meets applicable requirements. The 723 would also have the ability to program basic safeties, standard start-up/shut-down procedures, and a redundant fuel-air curve to provide engine control in the event the closed-loop signal from the NGK sensor is lost. (A separate DOE funded project is evaluating various control strategies based on modified forms of the standard fuel-air curve to provide better integration with the closed-loop signal from the NGK sensor.)

4.5.2 Spark Timing Control and Knock Detection

If the simple PID controller for AMP or exhaust equivalence ratio is employed, a system to detect knock and compensate with timing retard should be implemented. This system would allow spark timing to be advanced to OEM specifications and prevent knock in the extreme condition where insufficient boost pressure (air-limited condition) can be delivered to maintain the air/fuel ratio. The unit is currently configured with an Altronic II-CPU, which has a feature for automatic timing retard through a 4-20 mAmp signal. Several companies make knock detection systems that feature accelerometers tuned for the particular knock frequency of a given engine.

Modern knock detection systems utilize accelerometers strategically located on the engine and tuned to the specific knock frequency of a given engine. This signal is routed to a control module that is programmed to look at this signal only during the combustion

duration of each cylinder, called windowing, to prevent false triggering from vibrations caused by other engine events. Once the signal exceeds a programmed threshold, the control system commands the ignition timing to be retarded. The timing retard is usually done in steps, with the knock sensor signal rechecked to determine if knock has subsided. The controller will keep retarding ignition timing if a knock trigger is continually detected. If timing retard has continued to a significant level and knock is still being triggered, the control system will send a signal to either shut down the engine or reduce load or some other corrective action that is programmed.

The original approach for this demonstration was to obtain a demonstration unit from either Woodward or Altronics for field testing. Both companies have knock detection systems available. The Altronics system would have been more ideal, as it would interface directly with the II-CPU ignition system on the HBA. However, Altronics is unable to provide a demonstration system. The current approach is to acquire the accelerometer(s) and install on at least one cylinder of the engine. It is anticipated that a Metrix sensor, used by Altronics, will be obtained for demonstration. This Metrix device has been evaluated at Williams Station 60. The signals from the Metrix sensor will be routed to the SwRI data acquisition system to display the knock signals. A manually adjusted trim pot will be used to interface with the II-CPU ignition module to manually reduce timing when knock is intentionally induced on one cylinder and the sensor signals clearly demonstrate detection. While not an automatic system, this setup will allow demonstration of the technology and show the potential for its use on these two-stroke integral engines.

4.5.3 Manifold Design for Improved Air Balance

4.5.3.1 Objective

The objective of this proposed task is to improve the cylinder-to-cylinder balance of trapped air mass, and therefore trapped air/fuel ratio, in an integral two-stroke compressor engine. Specifically, the current engine breathing and manifold design will be analyzed to determine new manifold designs and the cost-benefit trade-off of the new manifold designs. In addition, an investigation into the magnitude of contribution to air imbalance from component geometry and/or tolerance variations will be performed. Improved balance of cylinder-to-cylinder airflow is another technique for these older integral engines to comply with impending emissions regulations, achieve enhanced operation, extend integrity, extend reliability, and increase capacity for continued use in the U.S. natural gas transmission network.

4.5.3.2 Test Bed

The test bed for development, evaluation, and demonstration of manifold design for improved air balance will be a Cooper-Bessemer GMVH-6 two-stroke integral compressor engine that has been installed at SwRI laboratories. This engine is owned by Cooper Energy Services (CES) and was installed to develop and evaluate new products or technologies for reduced emissions and improved efficiency. The GMVH-6 engine is heavily instrumented with appropriate pressure, temperature, flow, and speed sensors for full engine characterization and performance analysis across the operating range of the engine. The test cell features advanced data acquisition, including time-averaged and crank angle resolved measurements, and controls. Additional instrumentation will be installed as needed to fully document the dynamic characteristics of the inlet and exhaust gasses.

The analysis and design process will utilize several software packages. The primary analysis and design tool will be an engine simulation software package that simulates the combustion and fluid dynamic behavior of the inlet and exhaust streams. Several companies produce engine simulation software packages. El Paso has experience with

Optimum Power Technology software on a Worthington UTC two-stroke integral engine. Therefore, the *Virtual 2-Stroke* ® simulation software will be purchased from Optimum Power Technology for this task. Optimum has offered to provide the software at a significant discount for the task.

A proposal for extra funding to perform these added tasks has been submitted to DOE. Co-funding will be provided by El Paso, GMRC, and Cooper Energy Services. Additional tasks are to be initiated upon DOE approval to proceed to subsequent activities (decision point 1) beyond Task 9.

4.5.3.3 Scope of Work – Air Balance

The scope of this proposed effort has been broken down in two additional tasks. The first includes detailed analysis of the air balance issue and conceptual design of manifolds to improve cylinder-to-cylinder airflow. At the conclusion of the first additional task, a review of the conceptual designs will be conducted with program participants to determine which design provides the best cost-benefit trade-off. The second additional task will then involve the detail design, prototype construction, and validation testing.

Depending on the success of this program, a third task to incorporate a second engine will likely to be conducted. This will be a follow-on program to be funded by industry, with DOE retaining involvement, to determine the benefits on a different engine model (i.e., Clark HBA-6T).

A list of associated sub-tasks is as follows:

- First Additional Task for Air Balance
  - Sub-task 1 – Form Project Oversight Committee
  - Sub-task 2 – GMVH Setup and Baseline Testing
  - Sub-task 3 – Baseline Simulation and Analysis
  - Sub-task 4 – Conceptual Design
  - Sub-task 5 – Conceptual Design Review

- Second Additional Test for Air Balance
  - Sub-task 1 – Detail Design
  - Sub-task 2 – Prototype Fabrication
  - Sub-task 3 – Prototype Validation Testing
  - Sub-task 4 – Cost-Benefit Analysis

4.6 TYPICAL DATA FROM SECOND TEST ON A GMW10

4.6.1 Overview

During the week of February 23-26, 2004, a test series was completed on a GMW10 at Williams Station 60 located in St. Francisville, near Jackson, Louisiana. Figures 90, 91, and 92 show the unit tested and the installation of transducers for compressor cylinder pressure, power cylinder pressure, and crankshaft strain. The station is scheduled for installation of retrofit technology designed to improve performance and reduce NOx later this year on all but one of the GMW10 engines. These engines currently have no turbocharger and a small amount of inlet air boost (about 1.5 PSIG) is achieved with Cooper's flapper valve driven by the crankshaft. The main theme of the tests recently completed is to provide baseline data for comparison with similar data obtained after the retrofit technology is installed. The planned modifications are the installation of a turbocharger, installation of a high-pressure fuel injection system (Enginuity's HPFI™), installation of cylinder pressure sensors on compressor and engine, and addition of automatic balancing as part of the high-pressure fuel injection system.

Figure 90. GMW10 Compressor Cylinders with Pressure Transducer Installed

Figure 91. GMW10 Power Cylinder with Pressure Transducers Installed

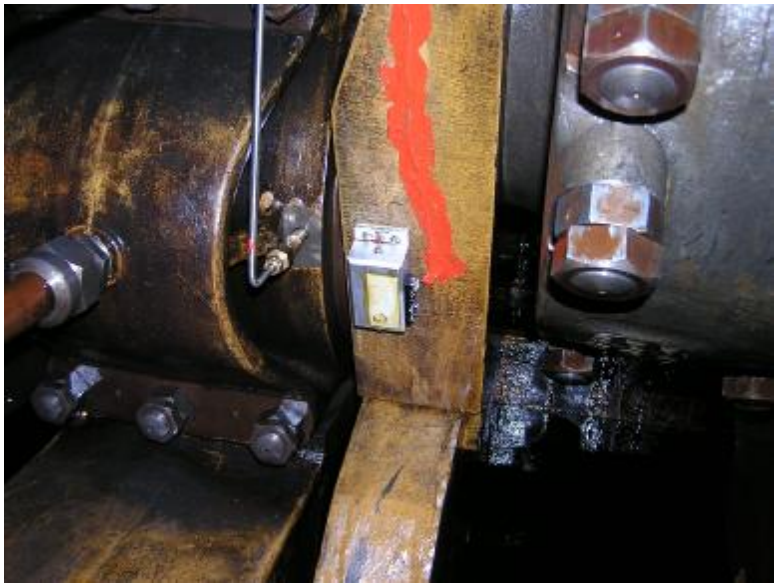

Figure 92. Strain Data Capture Module and Combined Power and Compressor Throw

A similar suite of instruments was installed as for the preceding tests described in this report, with the exception of the exhaust manifold sensor. All instruments worked well with the exception of the rod load monitor. This was installed with self-powering for the first time on this test program, and the self-powering provided insufficient power. This power problem has since been tracked down to nonlinearities in the relationship between gap and power generated. It is hoped to make changes to increase the power for the next test.

In addition to the instruments used in past tests, several knock detection sensors (loaned by Metrix) were used during the tests. The primary purpose was to gain experience with these sensors before using them at a subsequently planned test to evaluate the use of knock protection during timing advance tests. The instruments provide a voltage proportional to the count of events causing shock vibration above a specified threshold in the sample period.

4.7 DAY #1 TESTS – UNMODIFIED GMW10

After the instruments were installed and checked out on February 23 and 24, two days of testing followed. Figure 93 shows speed during the first day. For the first hour of testing to 11.21, speed was at 245 RPM. At 11.21, speed was increased to 250 RPM, where it remained for most of the test. Between 1.42 and 1.57, problems with the encoder caused a loss of speed signal, but not a change in speed. The sharp changes in plotted speed at this time should be ignored.

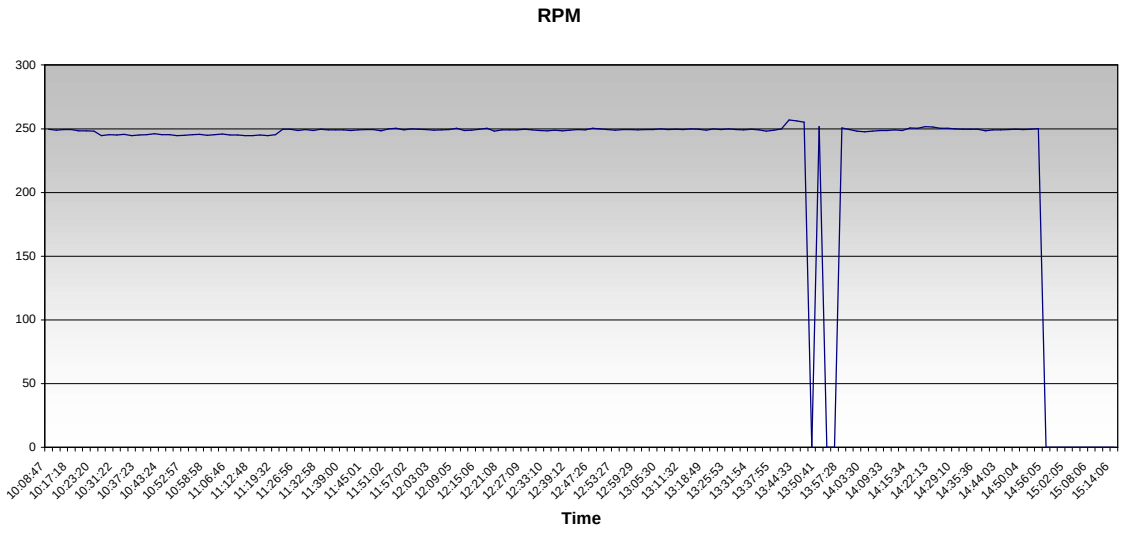

Figure 93. Speed in RPM Throughout Test Program from 10.08 Through 15.14, February 25, 2004; Day #1
(Loss in speed signal from 1.42 through 1.57 should be ignored.)

In addition to the SwRI instruments, Williams' personnel recorded a number of channels from the installed station instruments. Some of these channels provide a convenient profile of conditions during the test. The torque was maintained close to the range 100 to 101% during the day's testing, as shown in Figure 94, except towards the end of the day when an increase to about 103.5% occurred, which was then reduced back to 102% by load step adjustment. Figure 95 shows suction and discharge pressure during the day, with values very nearly constant at 573 and 774 PSIG, giving a ratio (shown in Figure 96) of about 1.34 until about 1:30 PM. Between 1:30 and 2:00 PM, suction

pressure fell to 505 PSI and discharge pressure rose to 781 with a resultant increase in ratio to about 1.37. This increase is part of the reason for the increase in torque towards the end of the day, though adjustments in load step, which went from Step 10 to Step 14, as shown in Figure 97, help maintain the torque close to 100%.

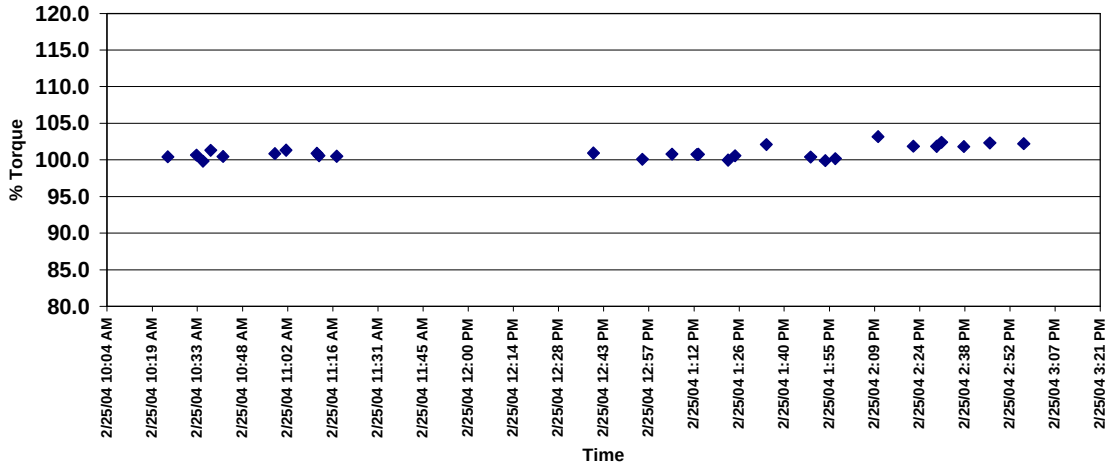

Figure 94. Torque, Percent from 10.04 Through 15.21, Day #1

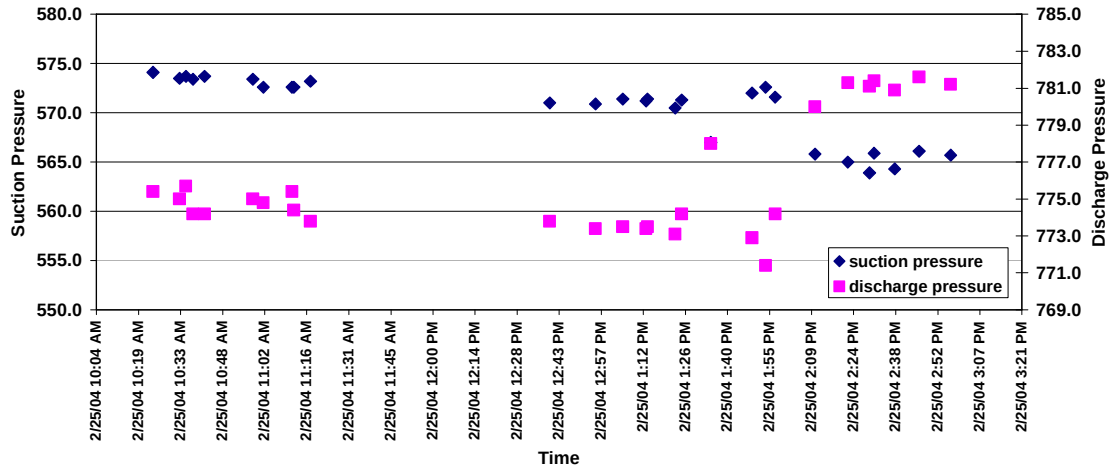

Figure 95. Suction and Discharge Pressure from 10.04 Through 15.21; Day #1

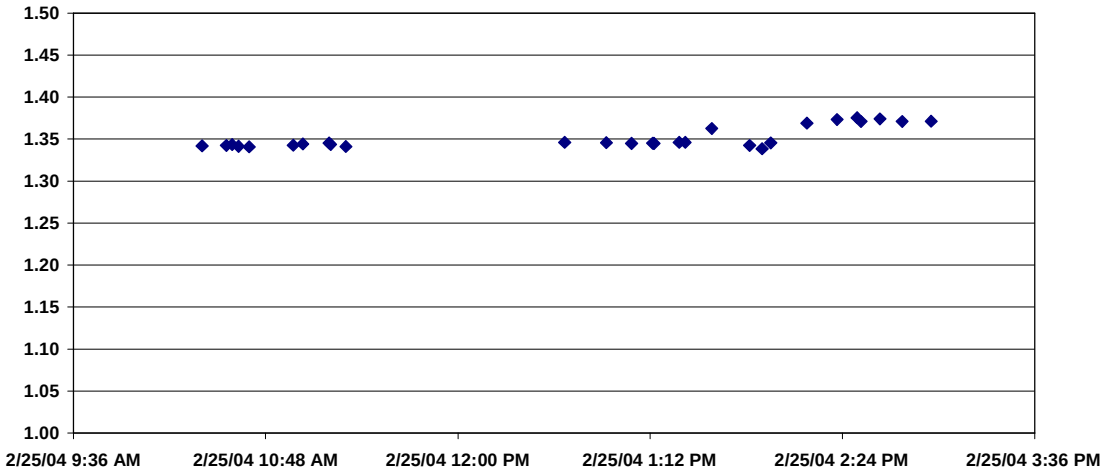

Figure 96. Ratio of Compression during Day #1

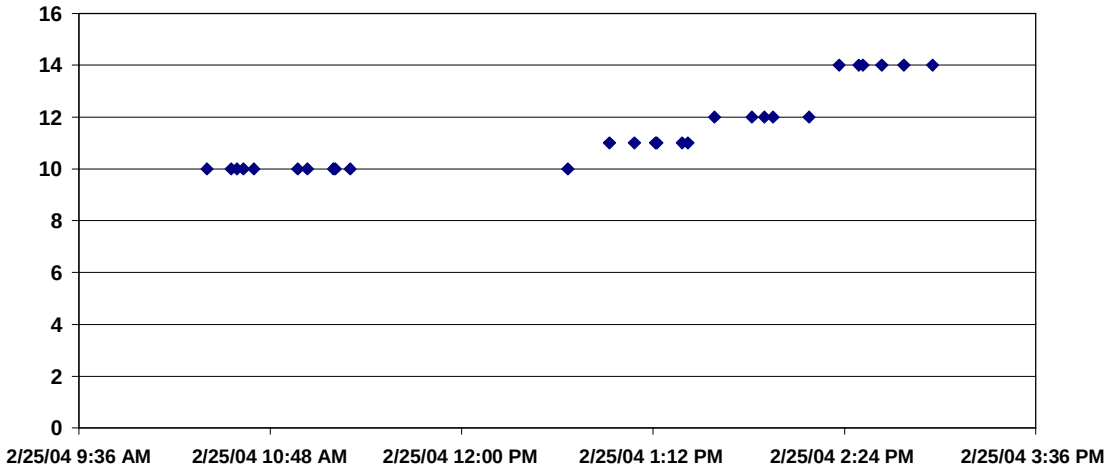

Figure 97. Load Step during Day #1

A number of temperatures relevant to operation, control, and protection are shown in Figure 98. Specifically, gas suction temperature remains around 58°F. Cylinder discharge temperature remains at around 101°F for most of the day, and increases to 104°F when the discharge pressure and ratio of compression increase (only cylinder #1 is shown, but the others have the same discharge temperature within 1°F; cylinders #2 and #3 tended to be about 1 degree lower in discharge temperature). Air manifold

temperature is between 102°F and 105°F. Lubricating oil cooling water remains very steady at 120°F; lubricating oil outlet temperature maintains itself at 143 to 144°F. Jacket water inlet and outlet are at 150°F and 160°F, respectively.

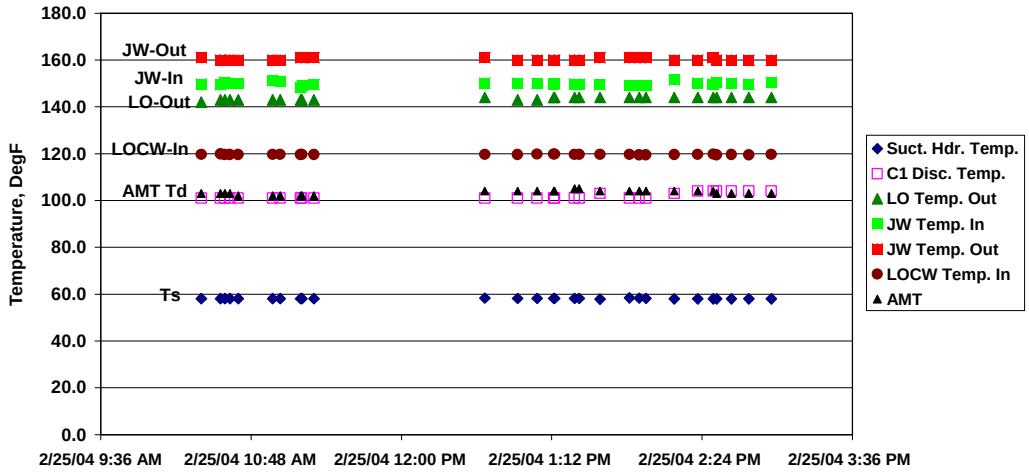

Figure 98. Temperatures during Day #1 for Suction Gas, Discharge Gas, Air Manifold, Lube Oil Cooling Water Inlet, Lube Oil Outlet, Jacket Water Inlet, and Jacket Water Outlet

To summarize Figure 98, the unit operating temperatures appeared quite stable during the day. It had been running immediately prior to the tests, so no significant warm-up occurred during the early hours of the tests.

Figure 99 provides an overview of test conditions during the day superimposed on a plot of peak-firing pressure normalized spread (expressed as a percentage of peak-firing pressure) during day #1. Day #1 was designed to provide a set of baseline data, including the effects of timing for the unmodified GMW10, to investigate balancing options, and to evaluate the influence of balance on performance.

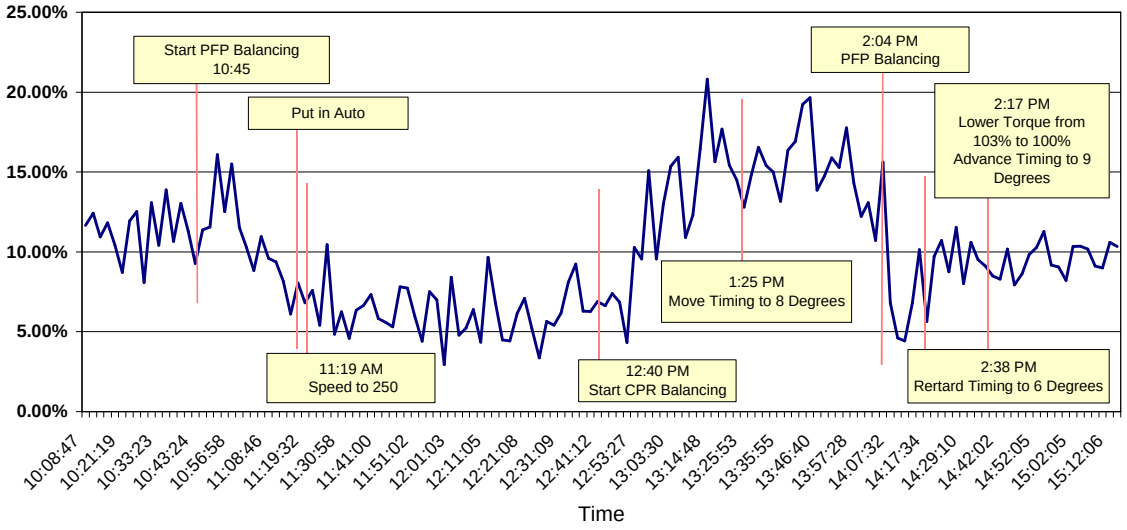

Figure 99. Test Conditions Overview Superimposed on Spread in Peak-Firing Pressure as Percent; Day #1

Thus, the log shows the unit was started soon after 10:00. At 10.45, peak-firing pressure (PFP) balancing was started, and the PFP spread was reduced from over 10% to about 6%. The unit speed was adjusted to 250 RPM at 11:21, then the unit was left run for an hour or so, with automated load step control activated. At 12:40, CPR balancing was started. Although this appears to increase the spread in peak-firing pressure to almost 15%, this is to be expected, since CPR seeks to equalize the ratio of peak-firing pressure to compression pressure. Compression pressure is defined for this test as P20, the pressure 20 degrees before top dead center (TDC). The implicit goal of CPR balancing is to equalize air fuel ratio across the cylinders, accounting for the differences in trapped air mass between cylinders.

Figures 100 and 101 present bar graphs of CPR for all cylinders. Clearly, Figure 101 has almost exactly equal height bars, indicating a CPR-balanced condition, whereas Figure 100 shows much more spread between the bars. These are two representative conditions: one indicating good CPR balance, and one showing cylinder-to-cylinder deviation in CPR.

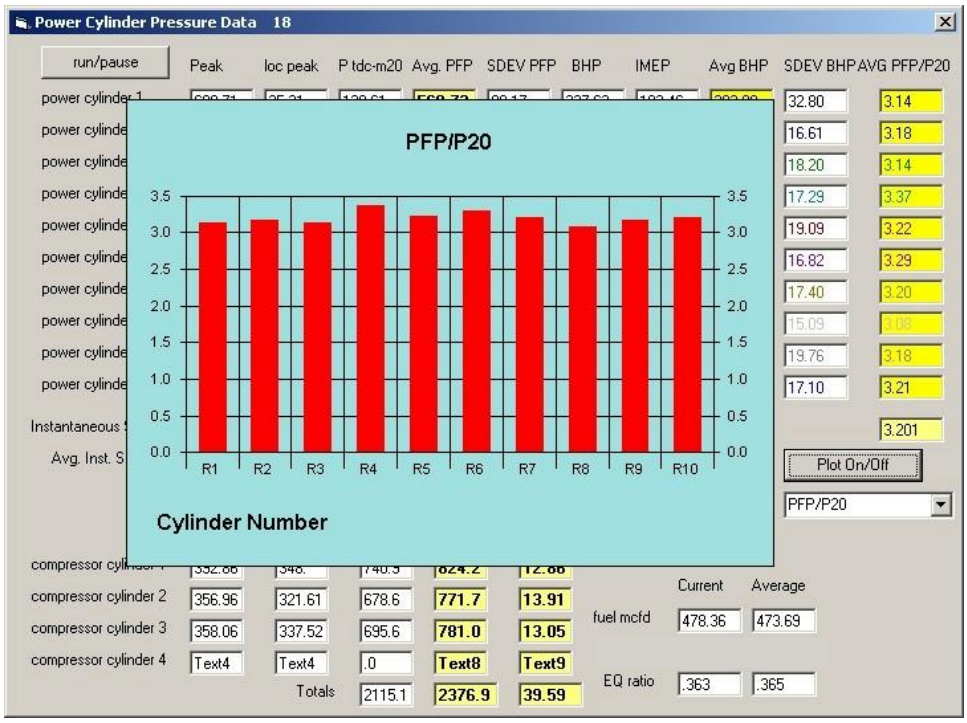

Figure 100. Cylinder-to-Cylinder Variation in Combustion Pressure Ratio (CPR); Day #1

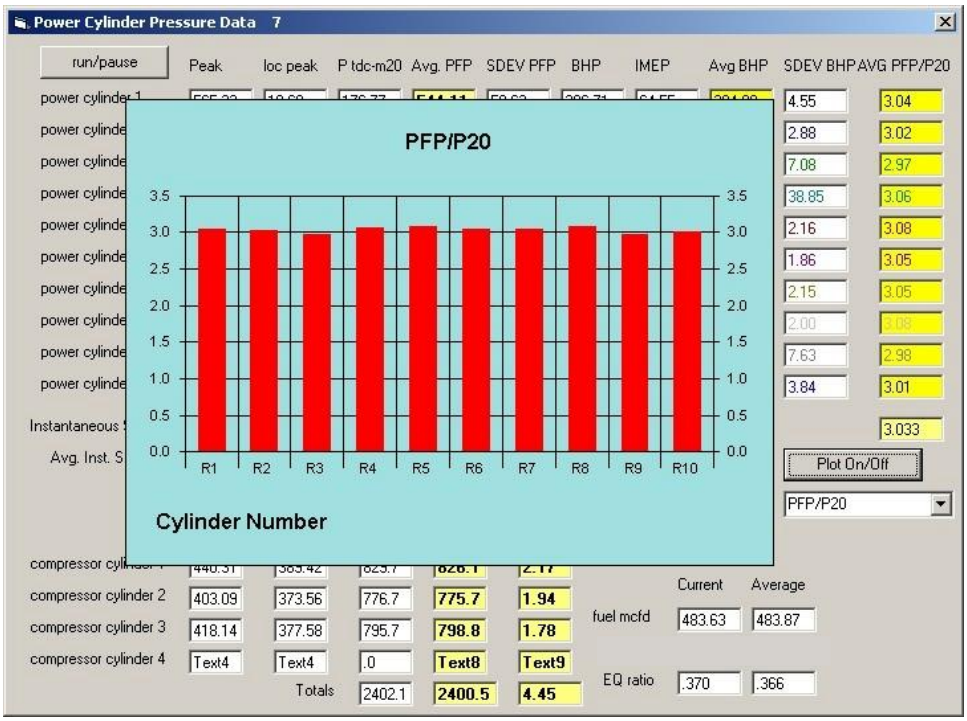

Figure 101. Cylinder-to-Cylinder Variation in Combustion Pressure Ratio after CPR Balancing

Returning to Figure 99, the log shows that at 1.25, ignition timing was advanced 2 degrees from 6 to 8 degrees before TDC. Then at 2.04 PM, peak-firing pressure balancing was initiated again, bringing the normalized spread in PFP momentarily down below 5%. Just as PFP balancing was being performed, station control instrumentation indicated torque had increased on the unit to over 103%, and at about 2.15 load step was increased from 12 to 14 in an attempt top reduce torque. Figure 94 has shown that this change succeeded in reducing torque, based on station instruments, to about 102%.

Timing was further advanced to 9 degrees at 2:17 PM, and then retarded back to 6 degrees at 2:38 PM. Testing ceased about 30 minutes after this final retarding.

Figure 102 shows the variation in fuel flow during day #1 testing. Up to about 10.30, the variation can be attributed to start-up transients, prior to any organized testing. Between the start of PFP balancing and the end, there is no obvious reduction in fuel flow. However, there is a distinct response of fuel flow to the increase in speed from 245 to 250 RPM – this 2% increase in speed at constant torque would cause about 2% increase in power and, hence, the fuel flow increases also by about 2%. Then just before 2:00 PM, a minimum in fuel flow rate occurs as a result of the timing advance to 8 – a reduction almost immediately offset by the increase in torque on the engine from the compressor, which causes an increase in fuel flow to keep the speed set point of the governor under increased load. The combination of load step adjustment and timing advance to 9 degrees brings fuel flow down, and then the return to 6 degrees timing causes fuel flow to go up again.

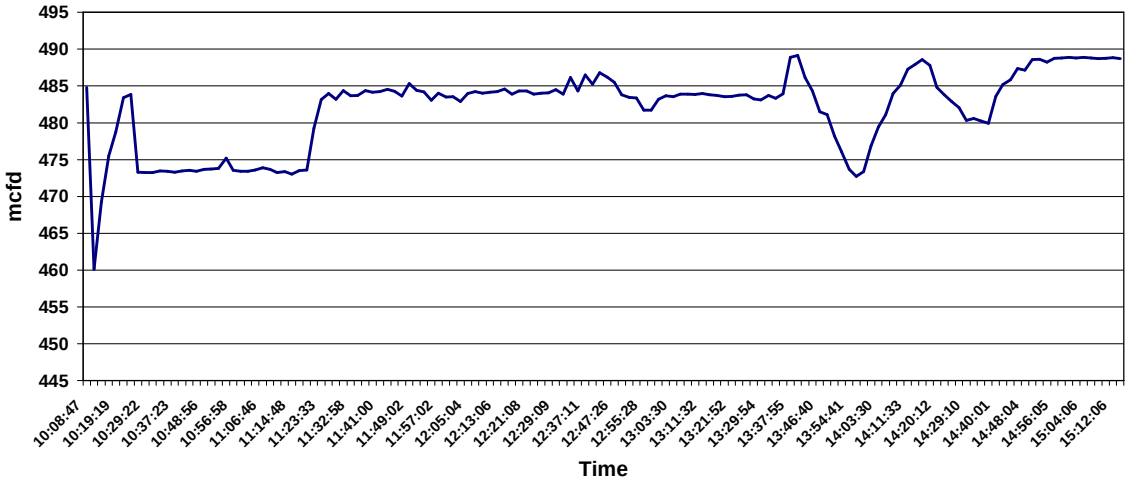

Figure 102. Engine Fuel Flow in MCFD during Day #1 Testing

There does not appear to be any notable relationship between fuel flow and state of balance – at least in the ranges of spread covered in the first day's testing.

In Figure 103, the fuel flow has been partially normalized in a plot of heat rate *versus* time – heat rate is the ratio of fuel energy consumed to energy provided by the engine to the compressor. Its units, by widely used convention, are BTU/HP-hour, using lower heating value as the fuel energy input (actually BTU/HP-hour can be related to thermal efficiency by the relationship efficiency = 2545/(BTU/HP-hour)).

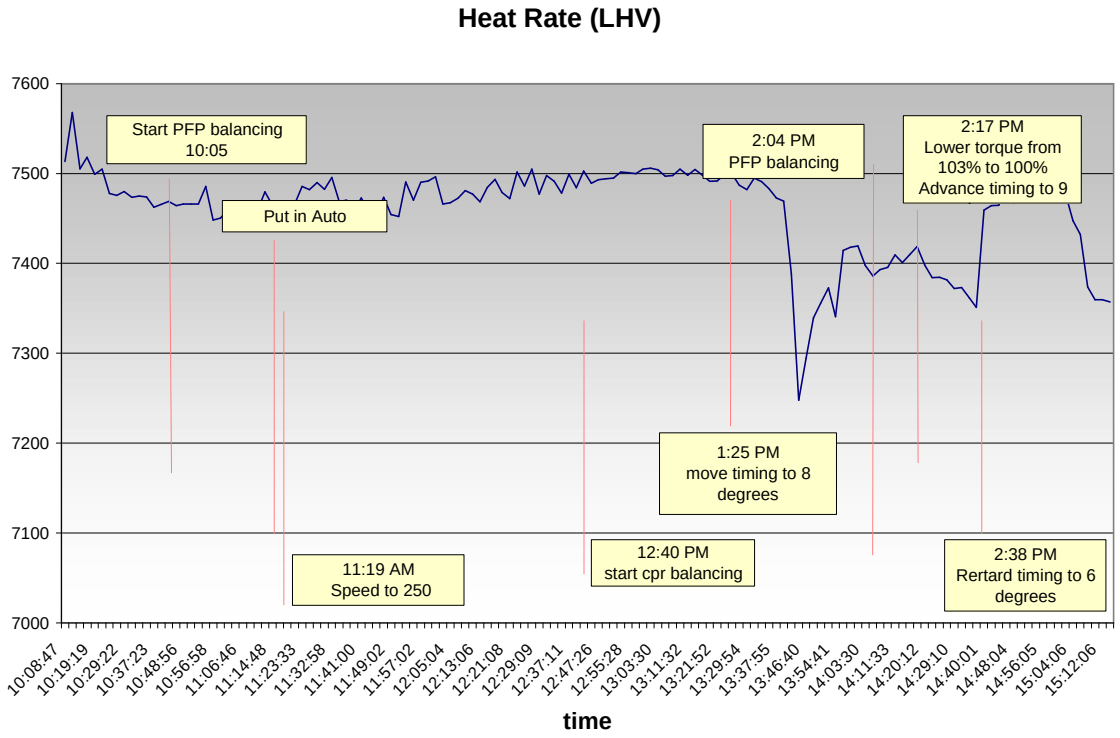

Figure 103. Heat Rate during Day #1 Tests

The first item of note from Figure 103 is that the average level of heat rate at 6 degrees timing is around (7500 BTU/HP-hr). This is distinctly higher than the value obtained at Williams Station 40 on a GMW10 similar to these, which already had been converted to high-pressure fuel injection conversion. The nominal value measured at Station 40 was 6900 BTU/HP-hr. at 8.5 degrees timing. A direct comparison will be made against data from the same unit at Station 60 after it has had the same conversion.

A second item of note is that the heat rate appears to respond directly to timing changes. The advance in timing from 6 to 8 degrees at 1.25 is followed in the next 19 minutes by a reduction in heat rate from 7500 to 7250 BTU/HP-hour (a 3.3% reduction). The advance from 8 to 9 degrees at 2.17 is followed by a reduction in heat rate from 7410 to 7360 in the next 18 minutes (a 0.7% reduction). The retardation in timing from 9 to 6 degrees is followed by an increase in heat rate over the next 18 minutes from about 7360 to 7560. The 18- or 19-minute delay in response to timing changes appears quite consistent.

Clear documentation of the factory specified nominal timing for these GMW units has not been obtained, but it is believed to be 8 degrees.

There is an increase in heat rate between the lowest value following the advance to 8 degrees, and the advance to 9 degrees. There was a load step change from step 12 to 14, between 2.10 and 2.21, in an effort to reduce torque from 103%, which may have influenced some of the observed changes in heat rate.

A third item of note in Figure 103 is the lack of a distinct response of heat rate to balancing changes – either by peak-firing pressure balancing, or by CPR balancing. No obvious change occurs in heat rate following the 10.45 start of PFP balancing or the 12.40 start of CPR balancing. It should be noted that the unbalance expressed as percentage spread prior to any balancing was only about 12%, so the unit was already moderately well balanced at the start of the day. On day #2, the effects of a bigger spread were investigated, as will be shown, also with little consistent influence of balancing.

Figure 104 presents the variation of compressor efficiency over the day's testing. The compressor isentropic efficiency is the quantity identified as "comp IHP-DIP HP". It varies over a range of about 1.8% from 83.3 to 85 over the day. The header isentropic efficiency tracks quite closely in the range 84 to 85 with one low outlier.

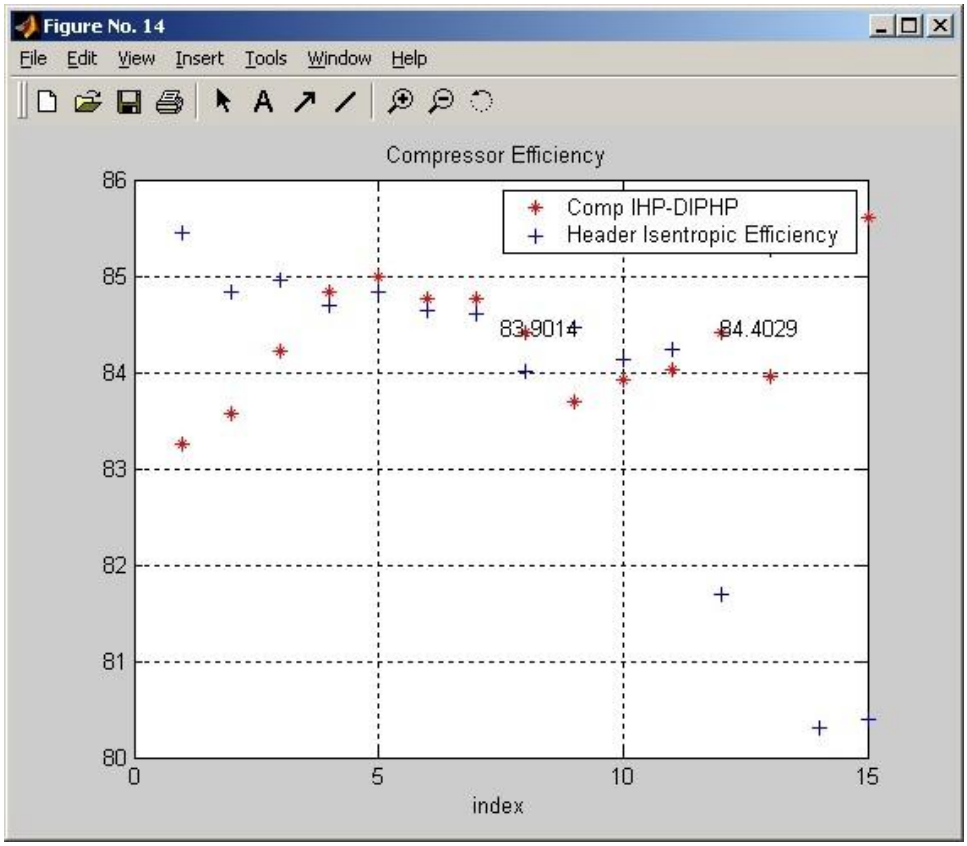

Figure 104. Compressor Efficiency

Figure 105 presents the overall system efficiency. The nominal value is 27.4%. It ranges between 27.3 and 27.5 over the first three and a half hours of testing, and then generally increases as a result of timing changes. This overall efficiency combines three important components: 1) the engine thermal efficiency; 2) the mechanical efficiency of power transmission from power cylinders to compressor cylinders; and 3) the thermal efficiency of the compressor. Unfortunately, the component efficiencies cannot be precisely isolated, but the overall efficiency is directly calculated as the ideal rate of doing work in compressing the gas from suction to discharge conditions divided by the energy input rate (calculated from the measured flow rate and fuel's lower heating value). Improving any of these efficiencies provides an equal opportunity to improve the overall system efficiency, which measures the conversion of fuel gas burned to useful compression work on the transported gas. Use of this quantity helps with the meaningful evaluation of any compressor package – integral or separable.

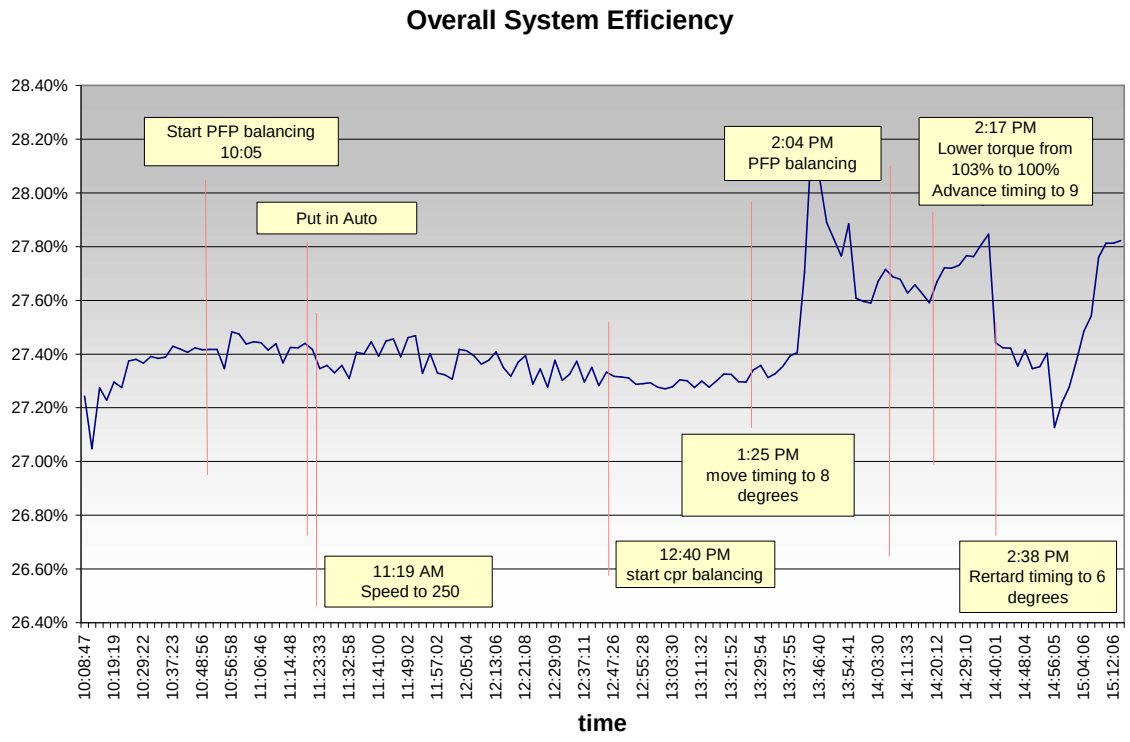

Figure 105. Overall Engine-Compressor System Efficiency

The unit tested at Williams Station 40 demonstrated an overall system efficiency of 30%, rising to 31.4% when timing was advanced. The benefits of the HPFI™ package modifications to the Station 40 units in improved overall efficiency are apparent. The benefits of similar modifications to the Station 60 units will be quantified following the planned tests later this year.

Figure 106 shows the ratio of engine to compressor power. This figure suggests a slight drop over most of the day, but it is not very pronounced. The excursion near the end of the day's testing is unexplained, but may have been a temporary response to a timing change from 8 to 6 degrees.

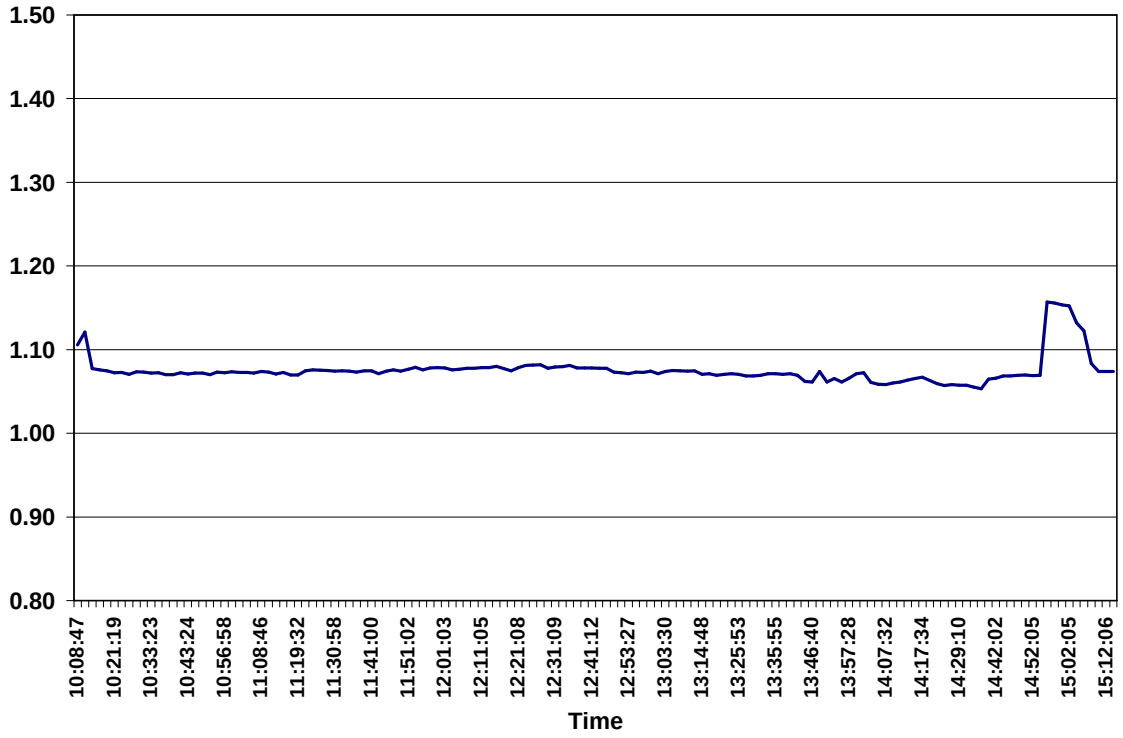

Figure 106. Ratio of Engine to Compressor Indicated Power

Figure 106 shows average values of peak-firing pressure and of P20 as they varied through the day. These are averaged over 50 cycles, and then averaged across the cylinders. The values of PFP, and P20 are approximately 600 and 200 PSIG, respectively, for reference purposes with some variation in peak-firing pressure during the day, from a minimum of 568 to a maximum 679. The compression pressure, P20, varies hardly at all during the day – its extremes are a low of 189.6 and a high of 203.1, but the majority of variation is much less.

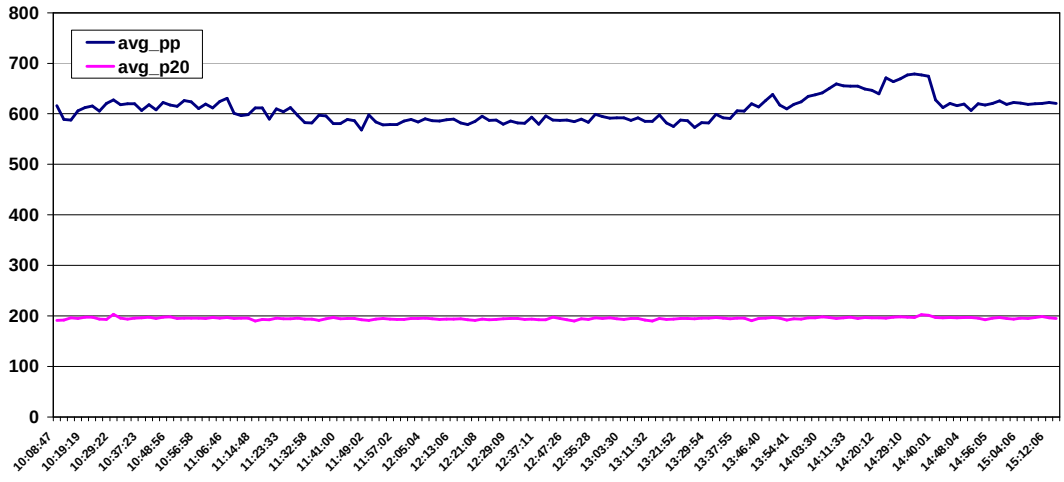

Figure 107. Peak-Firing Pressure and Compression Pressure (20° BTDC); Day #1

As might be expected, the mean value for peak-firing pressure appears to drop as a result of PFP balancing in the period 10:45 to 11:15 from about 620 to 600. There is a further drop in PFP to about 585 after 11:15. Speed is increased to 250 RPM at about this time, although with no change in torque, there is no obvious speed related effect on pressure to be expected; the load step stays at 10 until 12:55 PM, so small further drop in PFP may be the continued result of PFP balancing at 10:45 to 11:15.

Figure 108 presents the cycle-to-cycle standard deviation in peak-firing pressure, averaged over all cylinders. This quantity has a nominal value of 40 during the day, though it can vary from a low of 25 to a high of 55. The nominal value of 40 is actually lower than the values recorded and calculated at Station 40, which were about 58. Of course, the goal at Station 40 is to run as lean as is possible with minimum misfiring.

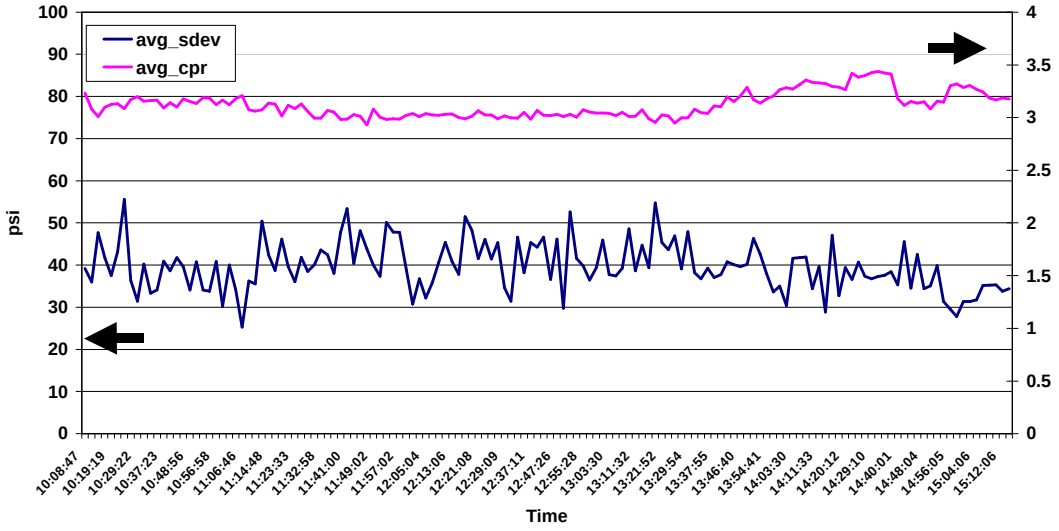

Figure 108. Engine Average Cycle-to-Cycle Standard Deviation Estimate; Ratio of Peak-Firing Pressure to Compression Pressure (CPR); Day #1

Figure 108 also includes the average value for combustion pressure ratio (CPR) – that is the ratio of peak-firing pressure to P20, the compression pressure. This, of course, follows a variation identical to the peak-firing pressure (discussed previously with respect to Figure 107). Its value runs from a low of just under 3 (2.92) to a high of 3.44. The highest values correspond to the most advanced timing. It is noteworthy that the CPR value for the GMW10 tested with high-pressure fuel injection, and turbo was in the range 1.8 to 1.85 — much lower than this unmodified unit.

Figure 109 shows the cylinder-to-cylinder variation of P20 and its cycle-to-cycle standard deviation estimate based on 50 cycles averaged over the day. P20 varies from cylinder-to-cylinder by about 20 PSI and its cycle-to-cycle standard deviation ranges from 2.8 to 4.4. Thus, P20 exhibits about a factor of 10 less short term variance than PFP. Looking forward, it is interesting that the following days data produced identical statistics for all the individual cylinder values of P20 and standard deviation in P20.

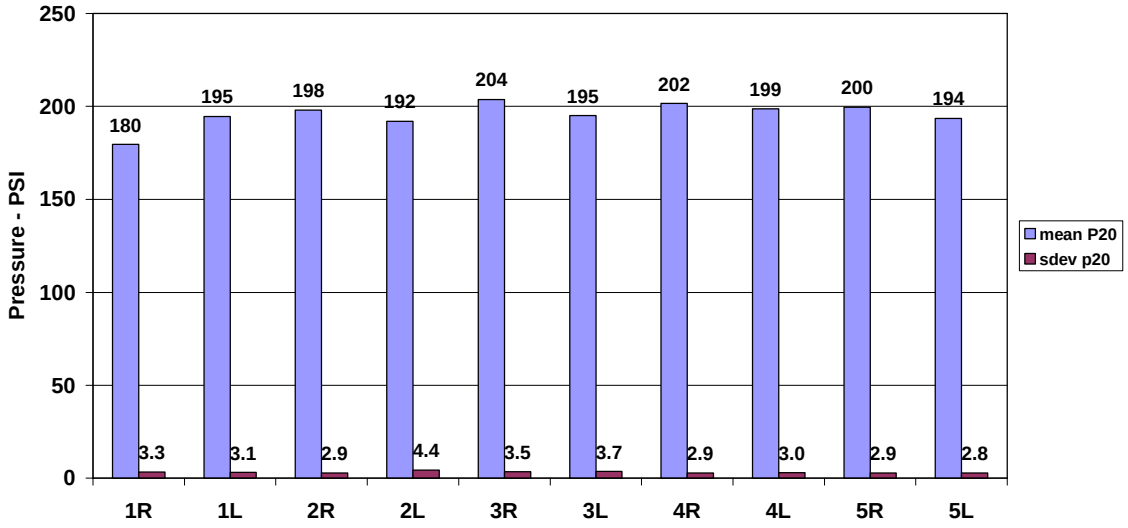

Figure 109. Mean and Standard Deviation for P20 (Pressure 20 DBTDC) as a Function of Cylinder; Day #1

Figure 110 shows the average and instantaneous cylinder-to-cylinder spread for peak-firing pressure. The average spread is the difference between maximum and minimum peak-firing pressure for all 10 cylinders, after the individual cylinder values have been averaged over 50 cycles. The instantaneous spread is the difference between maximum and minimum peak-firing pressure for all 10 cylinders obtained for each successive cycle, and then averaged over 50 cycles.

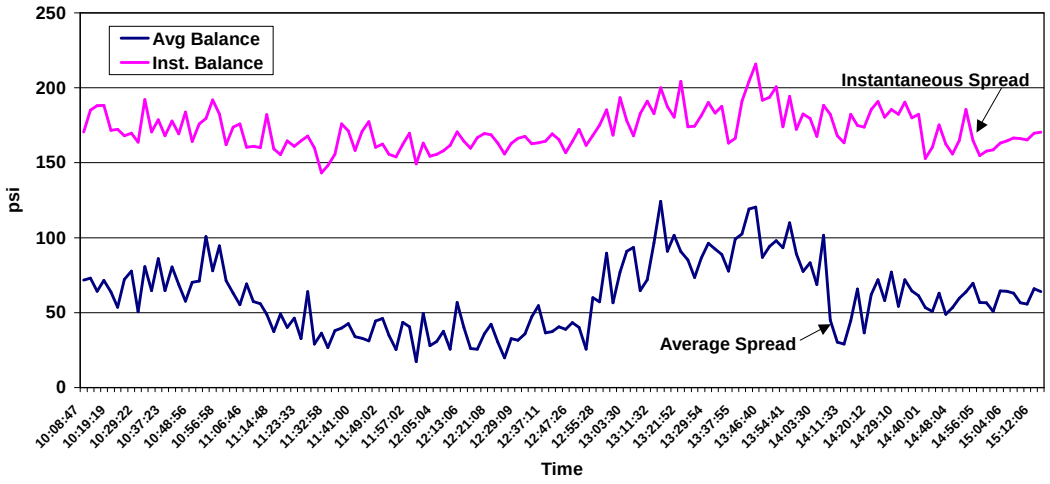

Figure 110. Average and Instantaneous Spread in Peak-Firing Pressure; Day #1

The result of PFP balancing is clearly apparent in the average spread – since this quantity is what PFP balancing seeks to reduce, the success in cutting this quantity from about 70 PSI to about 35 PSI is apparent. This is a 50% (factor of 2) reduction. However, the impact of balancing on instantaneous spread is much less – it reduces from about 175 to 160, which is by less than 10%. If balance were to reduce fuel consumption, it would tend to be as a result of reducing the extremity of outliers in the population of combustion events. Spread, particularly instantaneous spread, reflects the extremity of outliers, so this limited influence of balancing on fuel flow and heat rate is probably a result of this limited influence on instantaneous spread. Of course, the quantity spread does not directly measure the frequency of occurrence of the outliers, so there may be a yet more definitive cause if the outlier frequency statistics were reviewed; on the basis of this result, individual and population outlier statistics will be recorded and analyzed in future tests. As a result of CPR balancing, the instantaneous spread approaches 200.

Figure 111 shows the standard deviation estimate for variation across the cylinders of CPR, divided by the mean CPR value. This is the cylinder-to-cylinder coefficient of variation (COV) for CPR. It starts at about 4 and drops slightly as an immediate result of PFP balancing from 10:45 to 11:15. It drops further to about 3 over the next hour when

no changes to the engine occurred, and then as a result of CPR balancing starting at 12:40, it drops to 2, with a minimum recorded value of 1.41. As a result of PFP balancing, starting at 2.04, the COV of CPR increased from 2 to about 3.5.

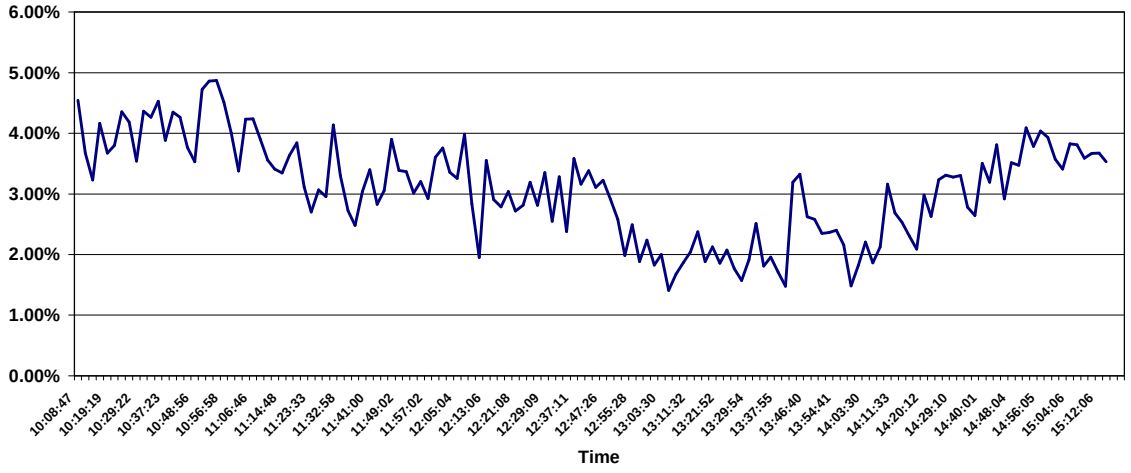

Figure 111. Coefficient of Variation for CPR (Standard Deviation/Mean); Day #1

The consistency of P20 is further emphasized by Figure 112, which presents the individual cylinder values as they varied during the day. It is noted that the pressure transducer for cylinder #1 was still giving trouble in this test series. The solution to this problem was discovered shortly after the tests at Williams Station 60. The lowest trace on Figure 112 should be higher.

Figure 113 shows the average location of peak-firing pressure (in degrees after top dead center). This quantity exhibits surprisingly wide swings with a minimum value during the day of 11.25 and a maximum of 28.125 degrees. Although the effect appears delayed and the wide variance makes trends hard to discern, this location of peak-firing pressure seems to respond most strongly to the timing changes, reaching its lowest value of 11.25 soon after timing is advanced to 9 degrees at 2.17.

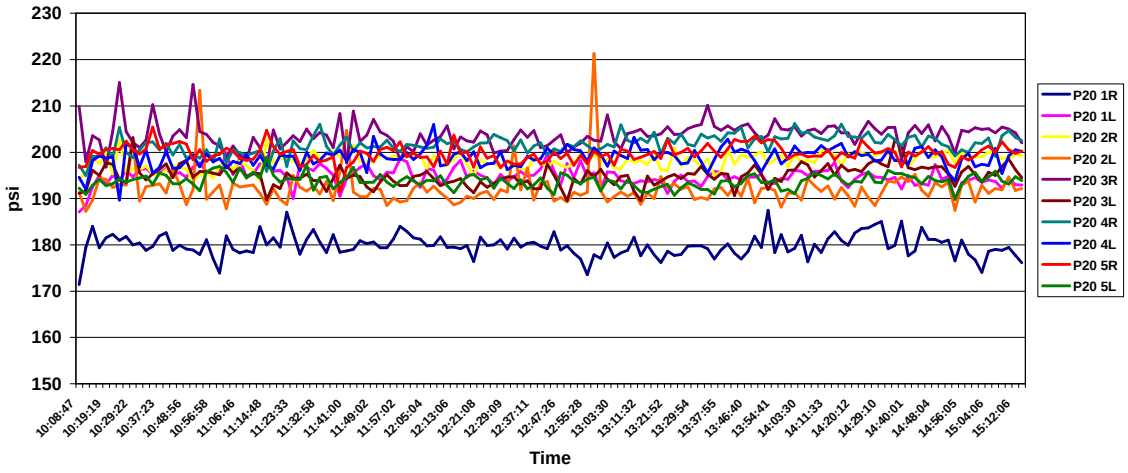

Figure 112. Variation of Compression Pressure (P20) for all 10 Cylinders; Day #1

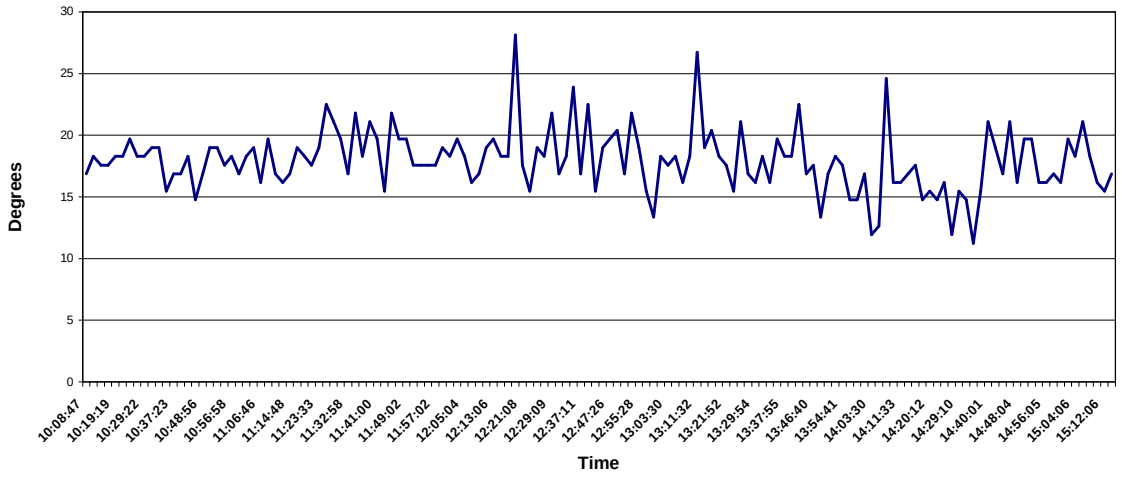

Figure 113. Average Location of Peak-Firing Pressure in Degrees after TDC; Day #1

Figure 114 shows the peak-to-peak vibration in inches per second at two locations on the frame and its variation during the day. The highest vibration averages over 0.9 inch per second peak-to-peak, and has maximum excursions to over 1.6 inches per second. This appears to be relatively high for frame vibration on a slow-speed unit. However, as a measure of how cycle-to-cycle and cylinder-to-cylinder variation in combustion might be influencing integrity, this vibration does not appear to provide a discernible trend.

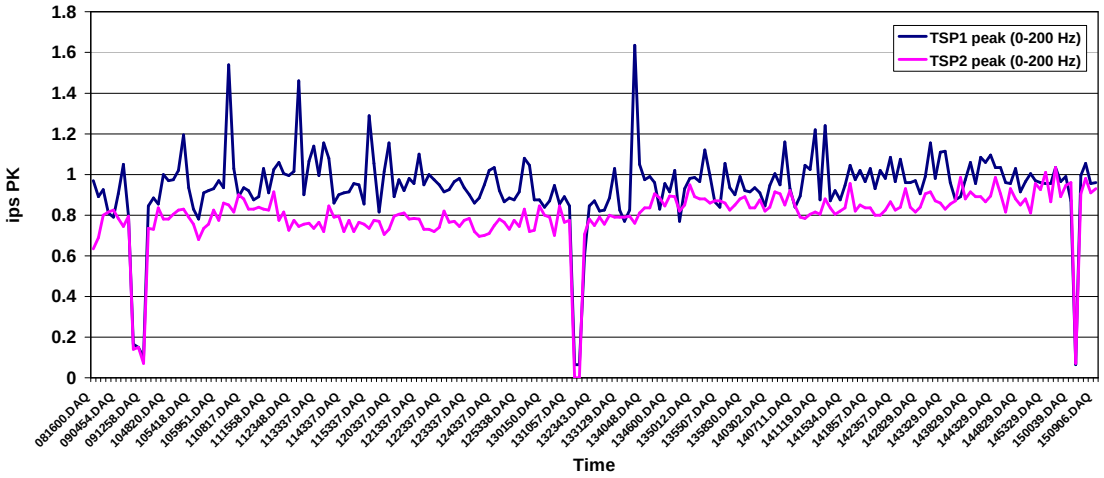

Figure 114. Vibration at Two Locations on Frame; Inches Per Second; Peak-to-Peak; Day #1

Figure 115 presents a waterfall plot of the vibration, showing a very dominant first order vibration, with magnitude of this order very similar to the peak-to-peak vibration. Based on this dominant frequency, an estimate can be made of the frame vibration in linear units. The result is a value of 30 mils or more (750 microns), and suggests a need to inspect the foundation, and a possible need for maintenance of the foundation and mounting of the unit.

The last three figures from the first day address crankshaft strain from the strain data capture module – the general characteristics of its output, and its relationship as a measure of integrity to the variation in test conditions during the day.

Figure 116 shows a typical series of waveforms over a 2-second snapshot (this is how the SDCM captures its data). The shape reflects the sharp variation in load on the crank throw over each revolution. It exhibits a narrow negative-going peak, often with two individual spikes, and a broader single positive going peak. The peak-to-peak amplitude in this snapshot is about 115 microstrains.

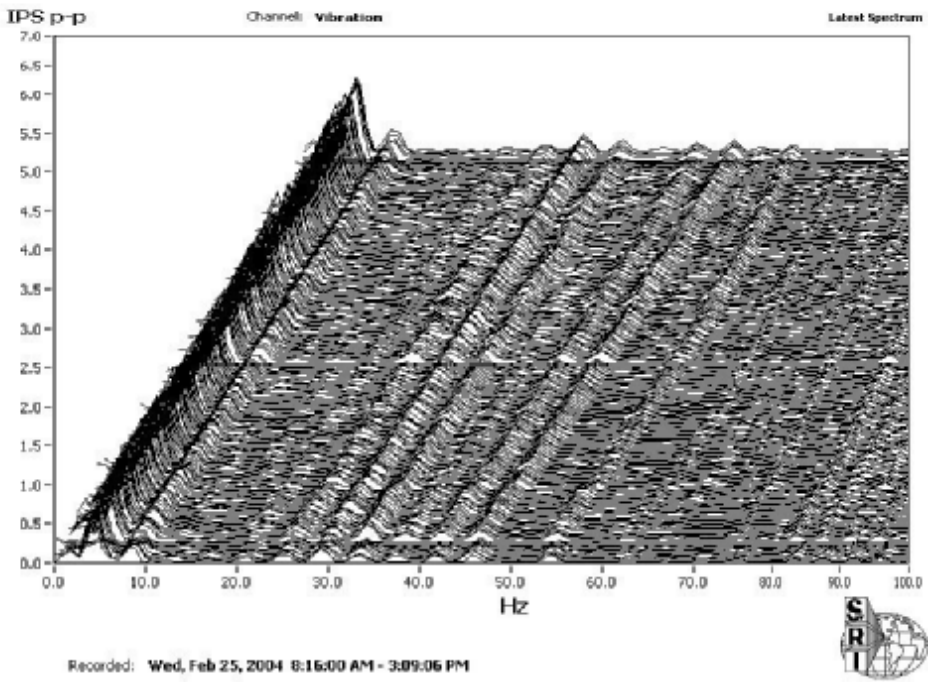

Figure 115. Vibration Waterfall Plot; Day #1

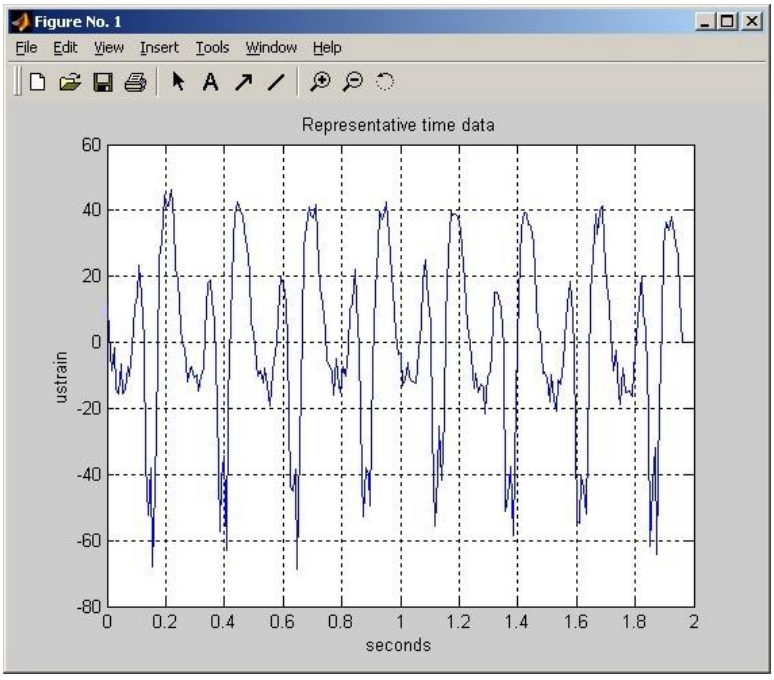

Figure 116. Typical Waveform for Crankshaft Strain Variation; Day #1

Figure 117 shows the spectral content as a waterfall plot over the day. The crankshaft strain shows noticeable amplitude at the first four orders, with the second order dominating (about 26 microstrains zero-peak). The second order is a strong component, because the compressor is double-acting and the SDCM strain gage rotates with the crankshaft, putting it in position to respond similarly to the applied load from either cylinder end. First order is also high at about 21 microstrains zero-peak, and third order is about 16 microstrains zero-peak. The fourth order is about 10 microstrains zero-peak.

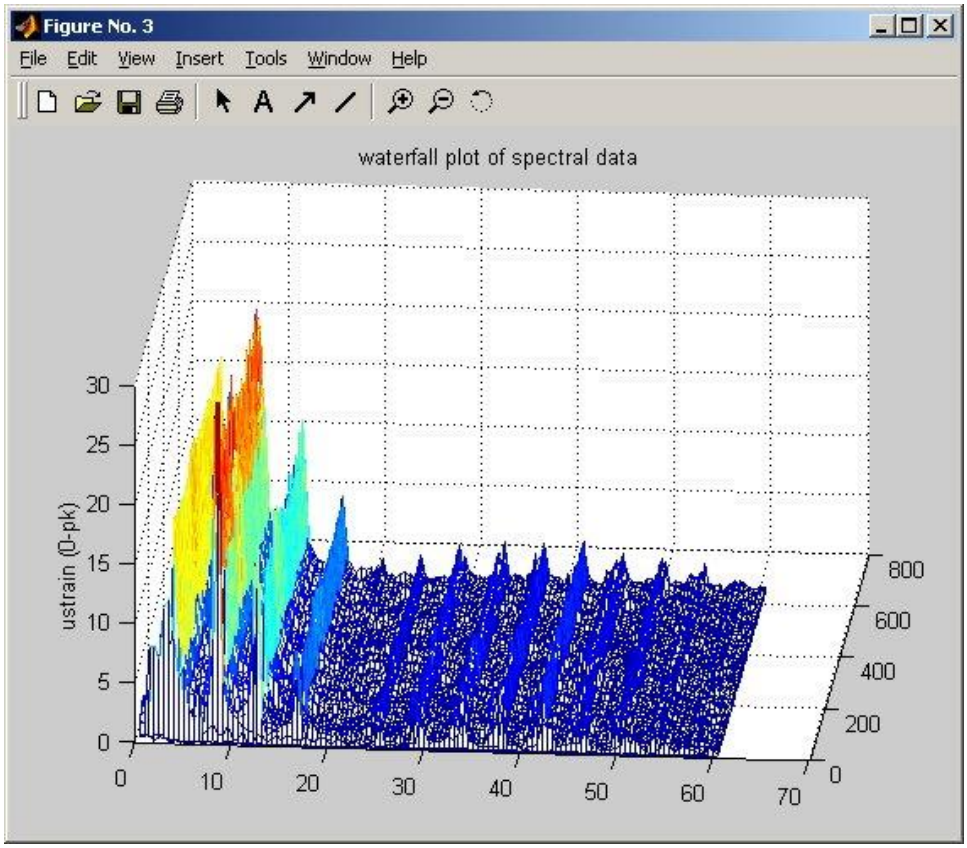

Figure 117. Waterfall Plot for Crankshaft Strain; Day #1

Figure 118 shows the variation in the peak-to-peak amplitude, extracted from each snapshot over the entire first day's testing, as a function of time in minutes from when the SDCM was installed and started for the day. The level stays quite steady at about 115 microstrains peak-to-peak until 220 minutes when a trend to increase starts, which

corresponds directly to the advances in timing, first to 8 degrees, and then further to 9 degrees — going up to an average of about 135 microstrains, and a maximum value approaching 145 microstrains. Thus, the 17% increase in crankshaft microstrains accompanies the approximately 12% increase in peak-firing pressure observed when timing is advanced and discussed with respect to Figure 107. This is a factor to be considered in conjunction with any performance benefits from timing advance.

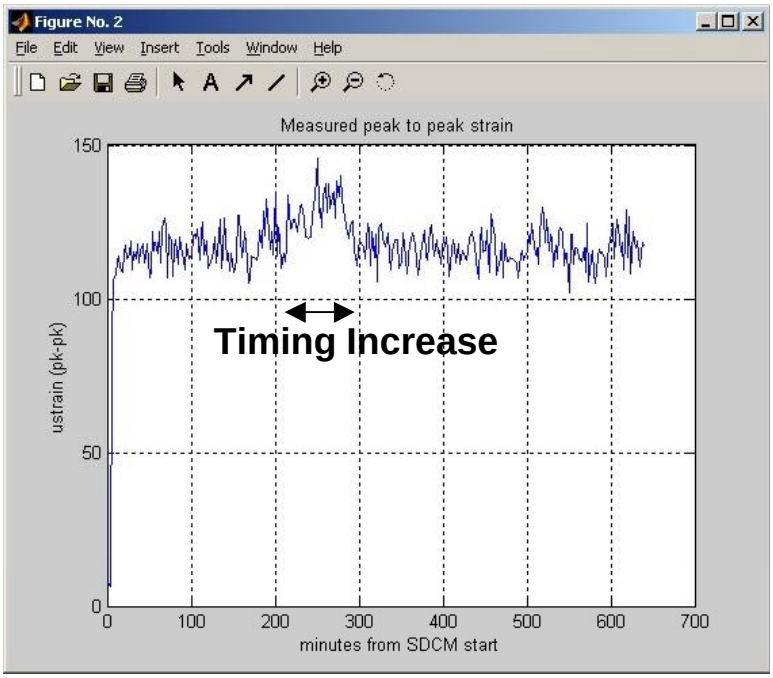

Figure 118. Variation in Peak-to-Peak Crankshaft Strain

Figures 93 through 118 conclude the data presentation and preliminary analysis for day #1's testing of the GMW10 at Williams Station 60.

4.8 DAY 2 TESTS – UNMODIFIED GMW10

The data from the second day of testing is presented in similar format to day #1, with a similar set of charts.

Figure 119 shows speed in RPM during the second day's testing – it was maintained close to 250 RPM from the start of testing, apart from three very brief and momentary excursions down by a few RPM.

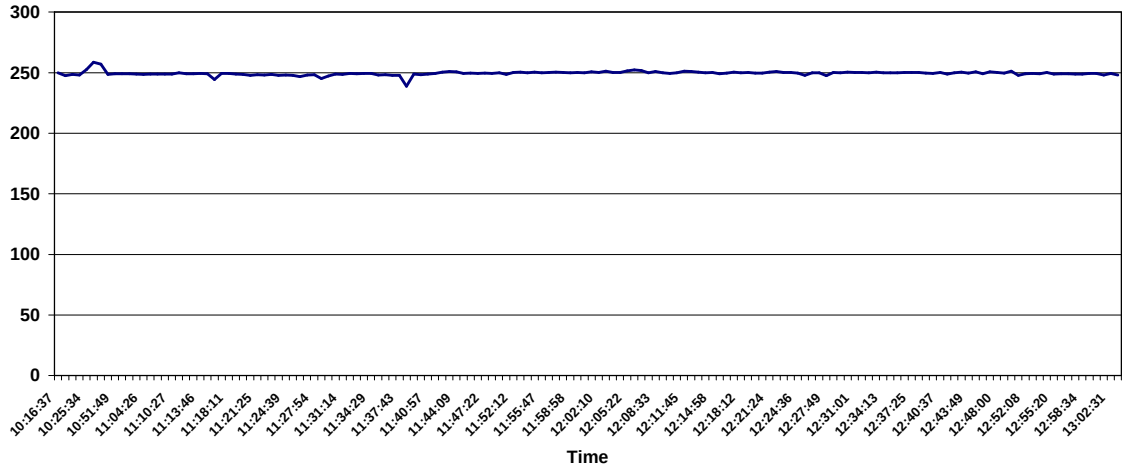

Figure 119. Speed Variation; Day #2

Figure 120 shows the torque during the day #2 testing from the station instruments and data system. It was maintained near 101%, except near the end of the test day when it was intentionally reduced to 94%, by an increase in load step to 19.

Figure 121 presents suction and discharge pressure. Suction pressure stayed very nearly constant around 530 PSIG, with a minimum of 527.1, and a maximum of 531. Discharge pressure started at 735.2, and ended the day close to 747, an increase of about 12 PSI. The corresponding ratio of compression is shown in Figure 122, increasing from 1.38 to about 1.4 in the middle of the day's testing, and then staying very close to 1.4 for the remainder of testing.

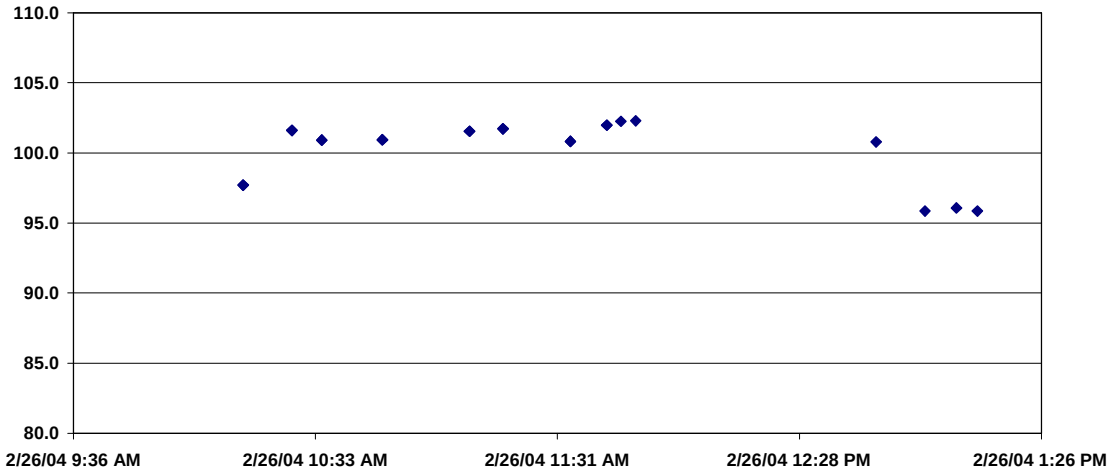

Figure 120. Torque from Station Data; Day #2

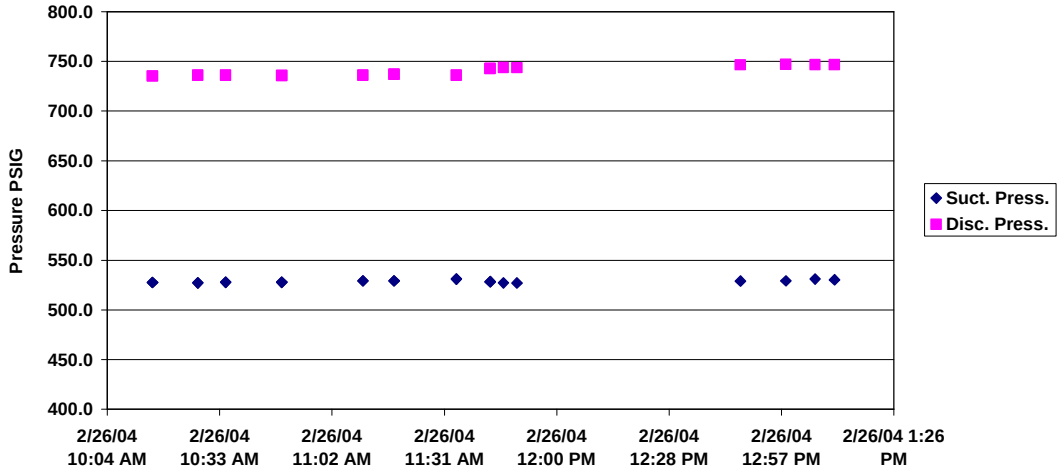

Figure 121. Suction and Discharge Pressure; Day #2

Figure 123 shows the load step. After starting and a momentary value of 12, load step stays at 8 for the early part of testing, and then increases to 9. To achieve the desired torque reduction, load step was increased to 19 for the last half hour.

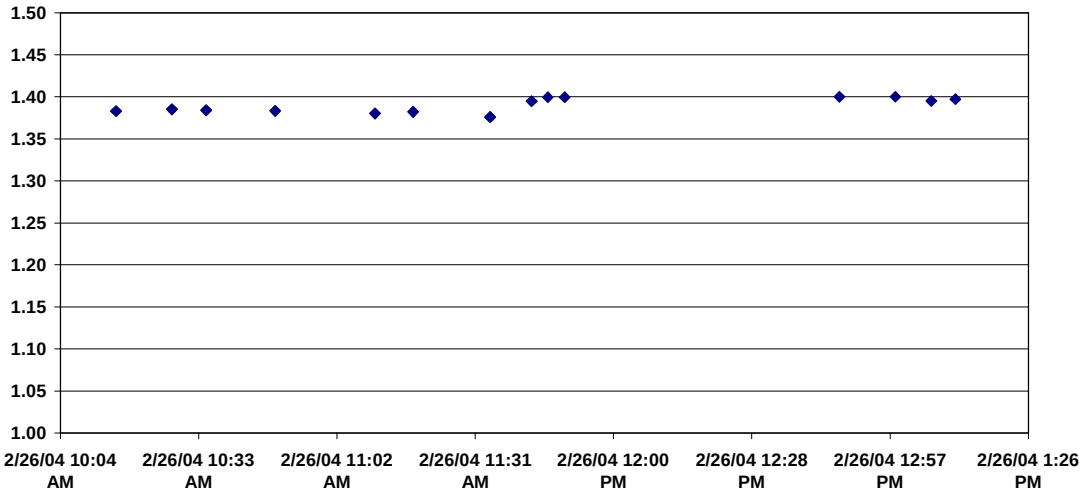

Figure 122. Ratio of Compression; Day #2

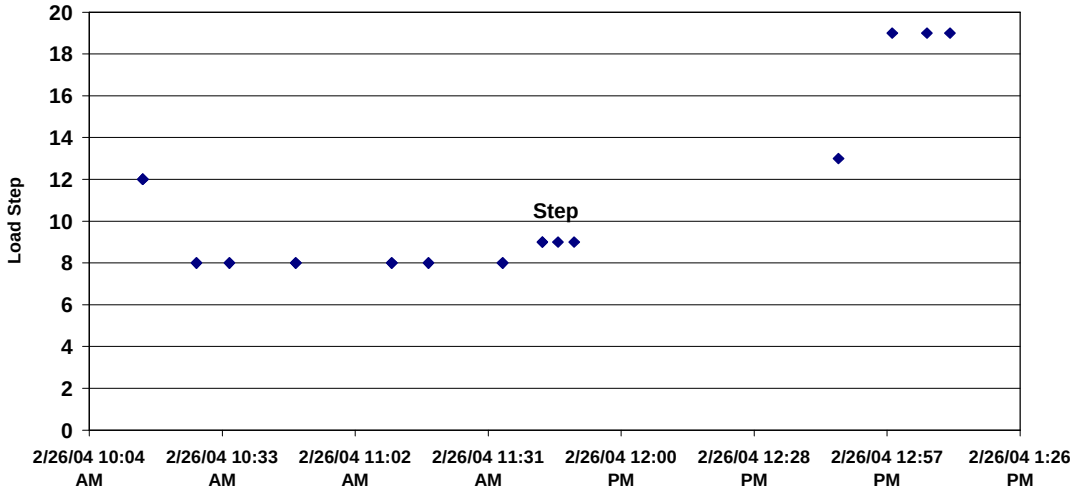

Figure 123. Load Step; Day #2

Figure 124 shows key temperatures of oil, water, air, and gas. Gas suction temperature stays very close to 58°F. Air manifold temperature stays close to 95°F (compared to 102°F on day #1). Cylinder #1 discharge pressure starts the day at 105°F, and ends the day at 106°F. Lube oil cooling water stays close to 120°F, with excursions down to 118°F, and up to 122°F. Lube oil outlet temperature stays around 142°F, but starts lower

at around 138°F and has excursions up to 144°F. Jacket water temperature in stays around 149°F and jacket water temperature out is between 185°F and 161°F.

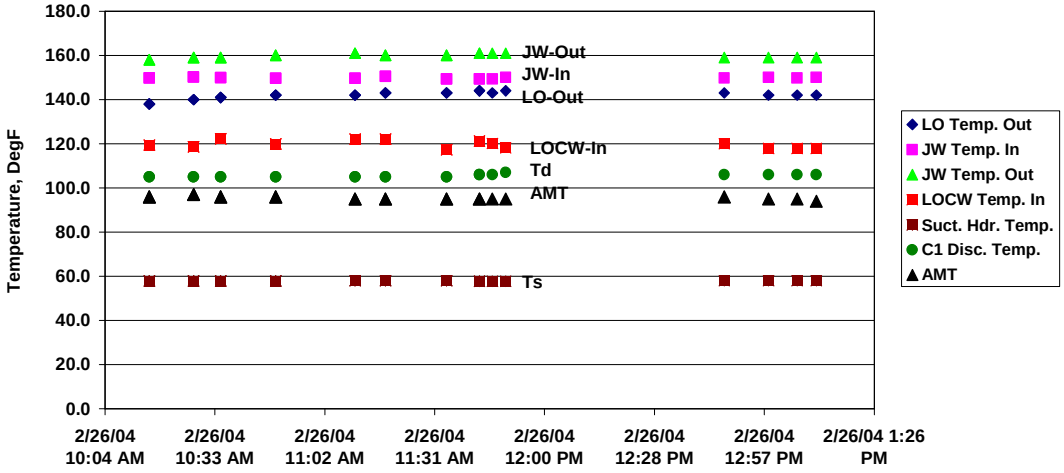

Figure 124. Temperatures during Day #2 for Suction Gas, Discharge Gas, Air Manifold, Lube Oil Cooling Water Inlet, Lube Oil Outlet, Jacket Water Inlet, and Jacket Water Outlet

On day #2, in an attempt to discern a stronger influence of engine spread on measured fuel flow and heat rate, the fuel flow valves in all cylinders were opened wide. Figure 125 shows the subsequent normalized spread and a log of events. The fuel valves were opened at 10:25 AM. The spread rapidly jumped to over 25%. At 11:10, ignition timing was advanced from 6 to 8 degrees. Balancing started at 11.15 and spread reduced from about 17% to 12% over the next half hour. At 11:49, timing was retarded from 8 to 6 degrees. At 12:45, the torque was reduced to 94%. The spread remained at around 15%, and the COV of CPR remained around 4.

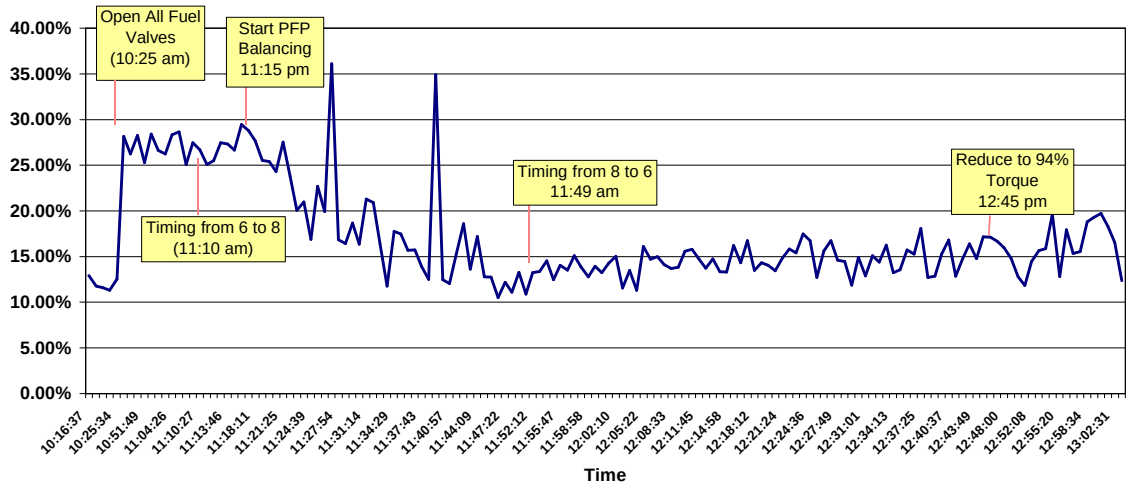

Figure 125. Spread in Peak-Firing Pressure as a Percentage with Timing of Test Conditions

Figure 126 shows the variation of fuel flow on day #2. This is presented for the purpose of documentation, and appears to respond distinctly to some changes, particularly timing changes. However, the next figure, 127, presenting heat rate, provides a more consistent basis for assessing how balancing and timing changes affect engine performance.

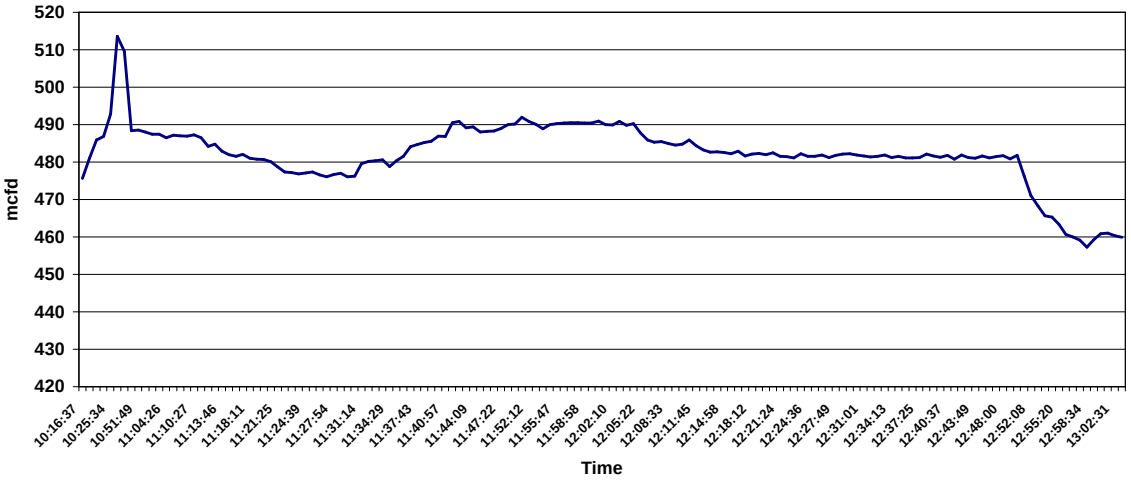

Figure 126. Engine Fuel Flow; Day #2

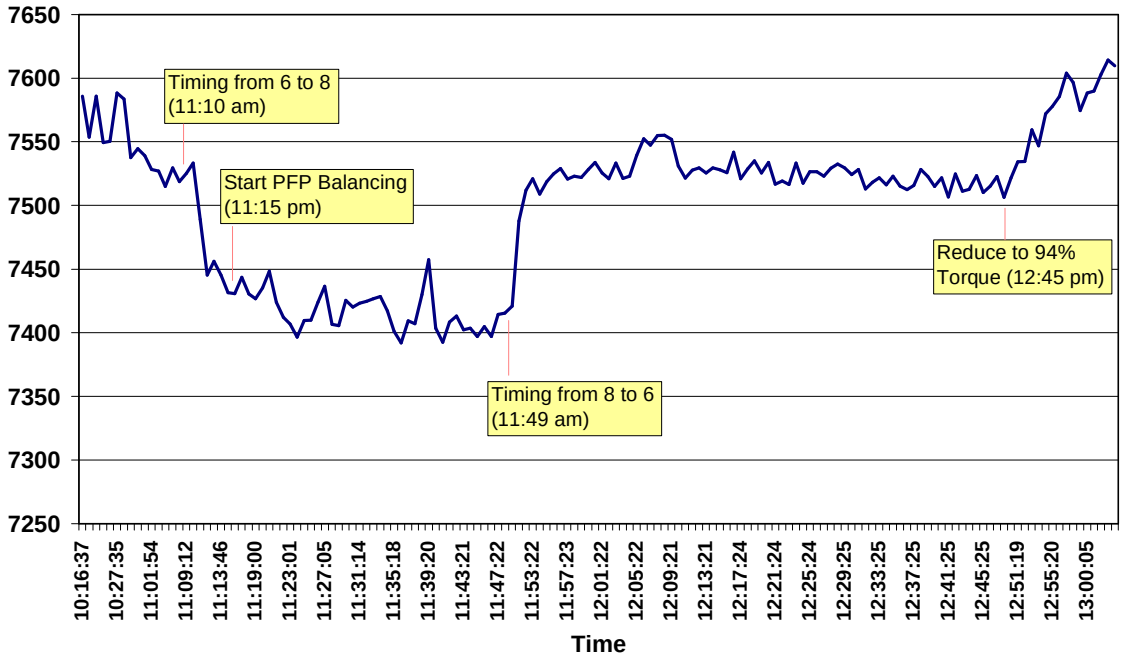

Figure 127. Heat Rate; Day #2

Prior to timing changes or balancing, the heat rate with fuel valves wide open and a spread of 27% is 7550 BTU/HP-hour. The previous day, prior to any timing or balancing changes with a spread of about 12%, the heat rate was about 7485. This might indicate that reducing the spread from 27 to 12% leads to a small reduction in heat rate, but the reduction is small — about 0.85% for a substantial reduction in spread. The heat rate on day #2 clearly responds to the advance in ignition timing at 11:10 AM, with an immediate reduction in heat rate of 90 BTU/HP-hour. PFP balancing, which reduces the spread from 27% to 15%, appears to be followed by a small reduction in heat rate, from 7460 to 7435. However, this small effect may also have been the continuation of heat rate reduction associated with timing advance, since the elapsed time for this influence is about 19 minutes. The torques on the two days at this point in the two tests were remarkably similar at about 101%; thus, any influence of torque level on heat rate can be discounted.

The retardation of timing back to 6 degrees was followed by an immediate increase in heat rate. After this, there were no significant changes, and the heat remained close to 7550 BTU/HP-hour, with the unit at 15% spread and timing of 6 degrees. Thus, there is no evidence from this data that on day #2, that balancing had any documentable effect on heat rate. Both with a spread of 27% and with a spread of 15%, the heat rate is 7550 BTU/HP-hour.

When the torque is reduced to 94%, there is a clear and immediate increase in heat rate from 7550 to about 7620 BTU/HP-hour – almost 1%.

Figure 128 presents the overall system efficiency; after the balancing and timing changes, this settles to 27.13% for a timing value of 6 degrees – very similar to day #1. The values obtained at Williams Station 40 were 28.6% for 6 degrees timing, 30% for 8.5 degrees timing, and 31.3% for 11 degrees timing. Thus, for the same timing of 6 degrees, we should compare 27.1% without the HPFI modification to 28.6% with it. The comparison will be more directly valid when made against data obtained on the identical unit – when tested later this year. With 8 degrees timing, the overall thermal efficiency on the Station 60 unit is 27.5%, and extrapolating approximately for 8.5 degrees (27.6%). This would be compared to 30% for the same timing (8.5 degrees).

Figure 129 presents the ratio of engine to compressor power. At approximately 1.11 to 1.13, it is clear this ratio has increased from the approximately 1.08 of the first day's testing. The start-up temperature of the oil was a few degrees lower than on day #1, but this is unlikely to account for this much difference in this ratio. In addition, this ratio appears to take a small jump up near the mid-point of the day's testing.

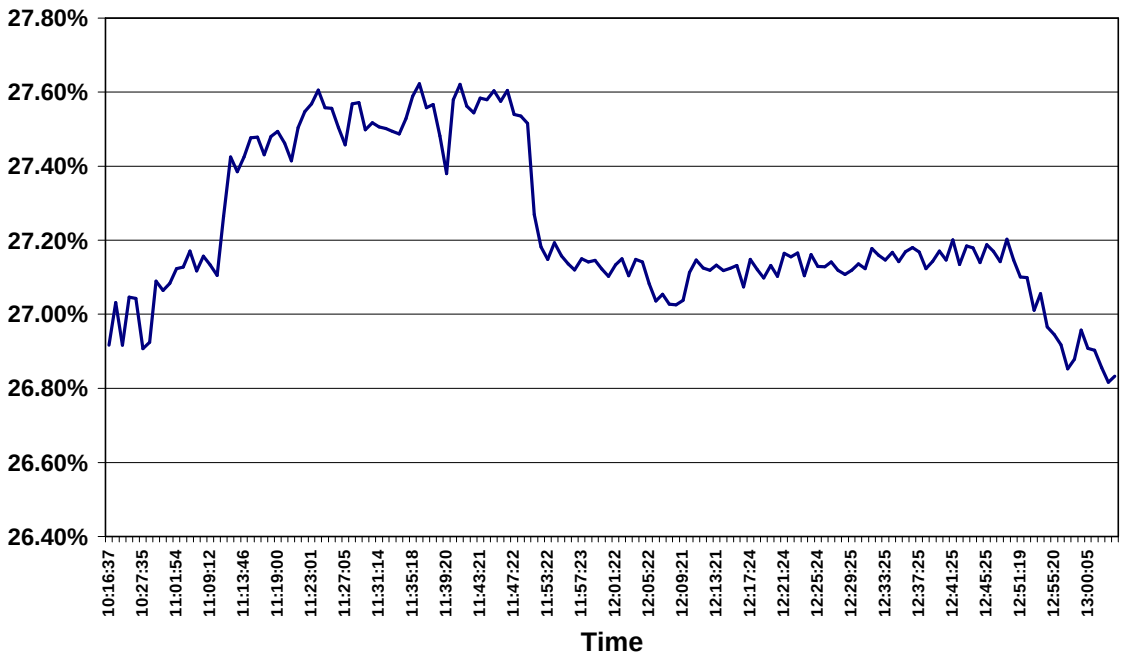

Figure 128. Overall System Efficiency; Day #2

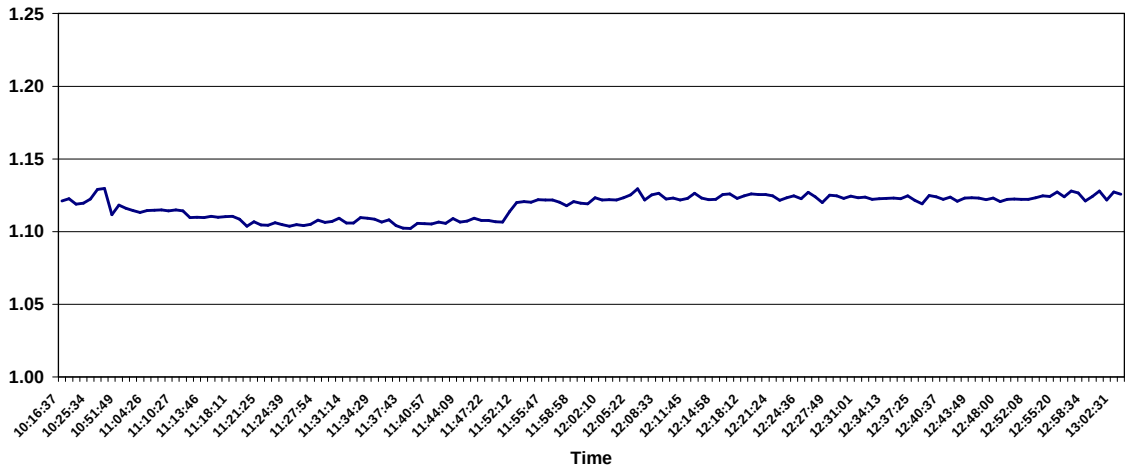

Figure 129. Ratio of Engine to Compressor Power

Figure 130 presents the peak-firing pressure and P20 during day #2 (averaged across the cylinders). As before, the P20 is right around 200 degrees. The peak-firing pressure is right around 600 PSI for the 6 degree timing, but increases to almost 700 PSIG with timing of 8 degrees.

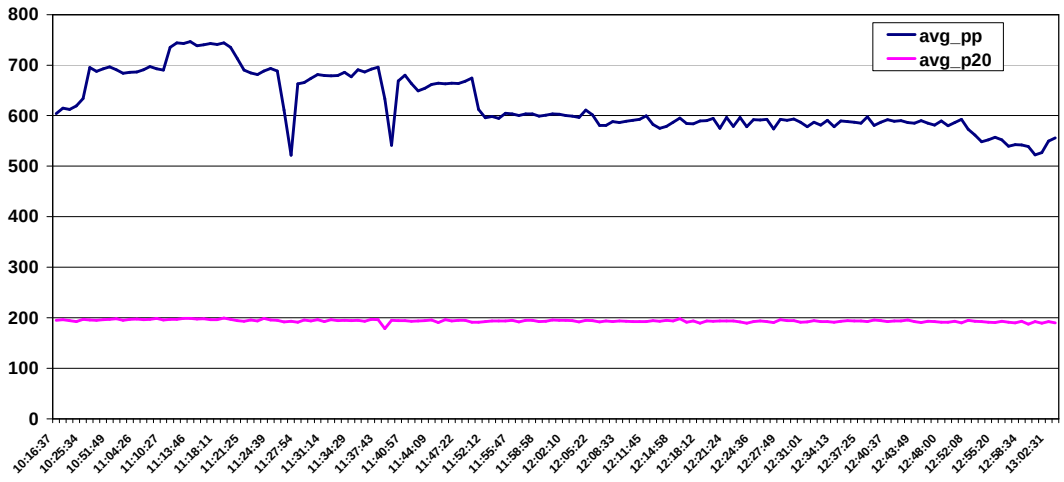

Figure 130. Peak-Firing Pressure and Compression Pressure (20° BTDC); Day #2

Figure 131 shows the variation of P20 for individual cylinders; the consistency of individual P20's, and their spread is apparent.

Figure 132 presents average standard deviation for cycle-to-cycle variation in peak-firing pressure, together with CPR (ratio of peak-firing pressure to P20). The peak-firing pressure standard deviation starts day #2 in the range 30 to 40 PSI, but increases to lie in the range 40 to 50 PSI for the second half of the test day, when the conditions were mainly steady running with 6 degrees timing. Based on Station 40 results, this standard deviation is expected to increase to 50 or 60, after the conversion to high-pressure fuel injection.

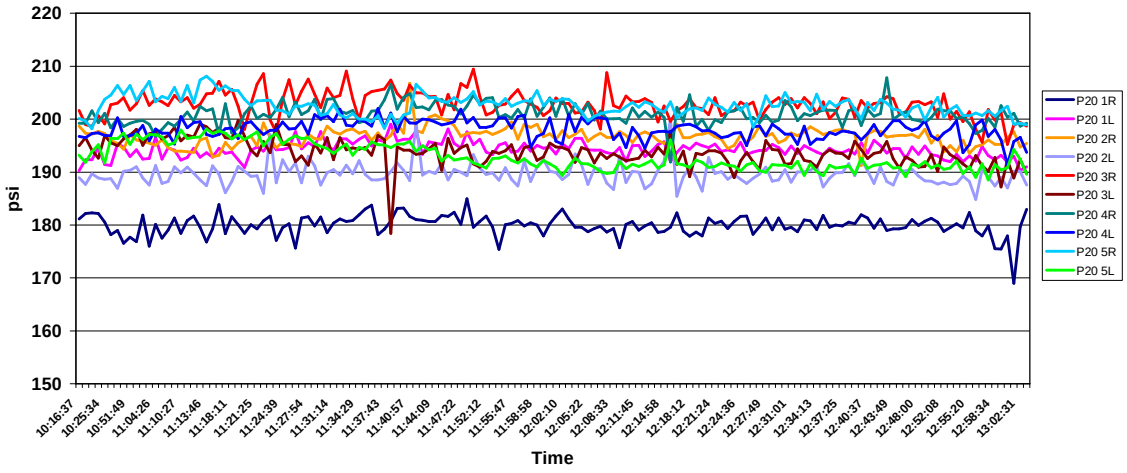

Figure 131. Individual Cylinder Compression Pressure; Day #2

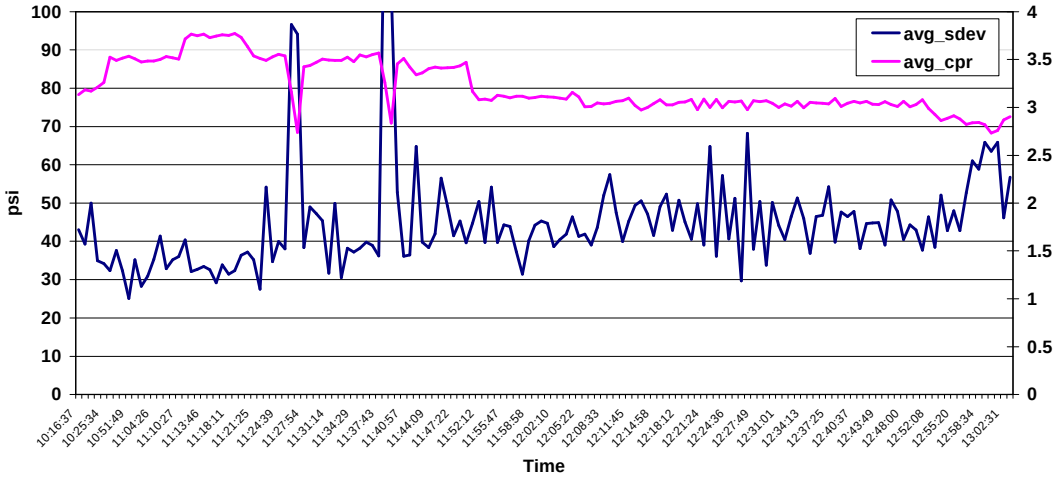

Figure 132. Engine Average Cycle-to-Cycle Standard Deviation Estimate; Ratio of Peak-Firing Pressure to Compression Pressure (CPR); Day #2

With the timing advances early in the day, combustion pressure ration, CPR starts off at about 3.8, but once timing is back at 6 degrees, the CPR remains steady at just about 3, just as for the previous day.

Figure 133 shows the mean value and standard deviation for CPR in each of the 10 cylinders. The values obtained for these quantities, when averaged over the day, were exactly the same for every cylinder on day #2, as for the same cylinders on day #1.

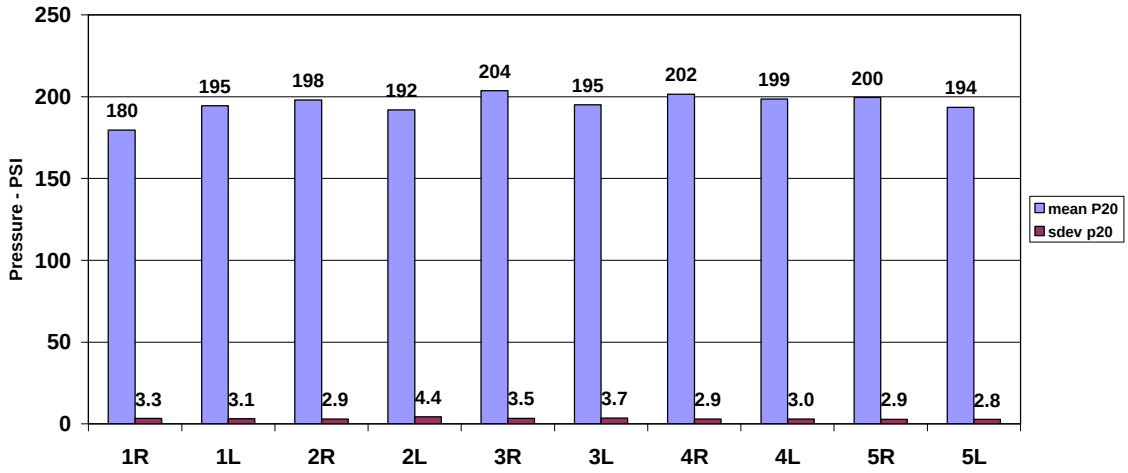

Figure 133. Mean and Standard Deviation for P20 (Pressure 20 DBTDC) as a Function of Cylinder

Figure 134 shows the average and instantaneous spread in PSI for day #2. As already discussed, these values are higher for day #2 than for day #1. The average spread starts at 200 PSI and drops to 80 PSI after balancing, a 60% reduction. The instantaneous spread starts at 280 PSI and drops to about 200 after balancing – a 28% reduction. This instantaneous spread after balancing is not much different from the instantaneous spread of the previous day.

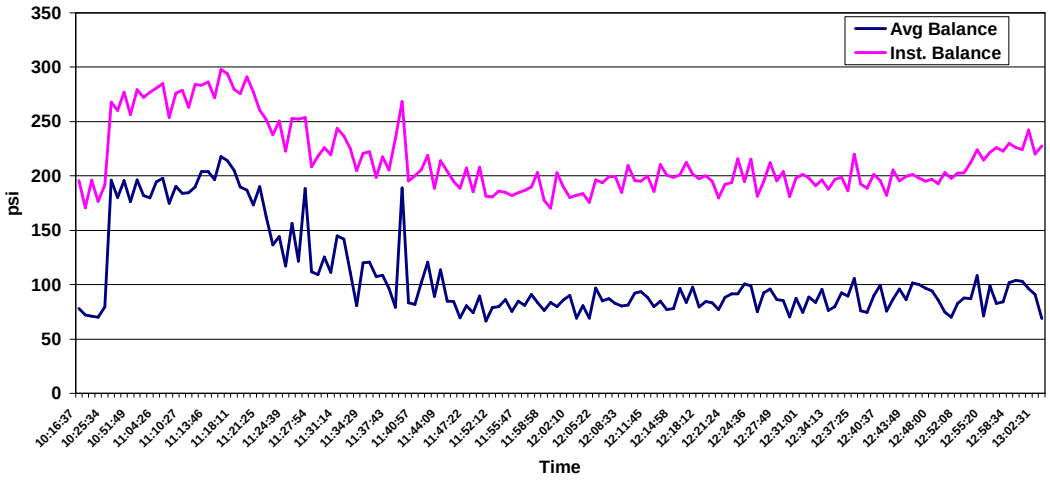

Figure 134. Average and Instantaneous Spread in Peak-Firing Pressure; Day #2

Figure 135 shows the estimate for COV of CPR variation across the cylinders. This drops from almost 9% prior to any balancing to about 3.7%, and maintains this level quite closely during the second half of the day's testing. This is also approximately a 60% reduction.

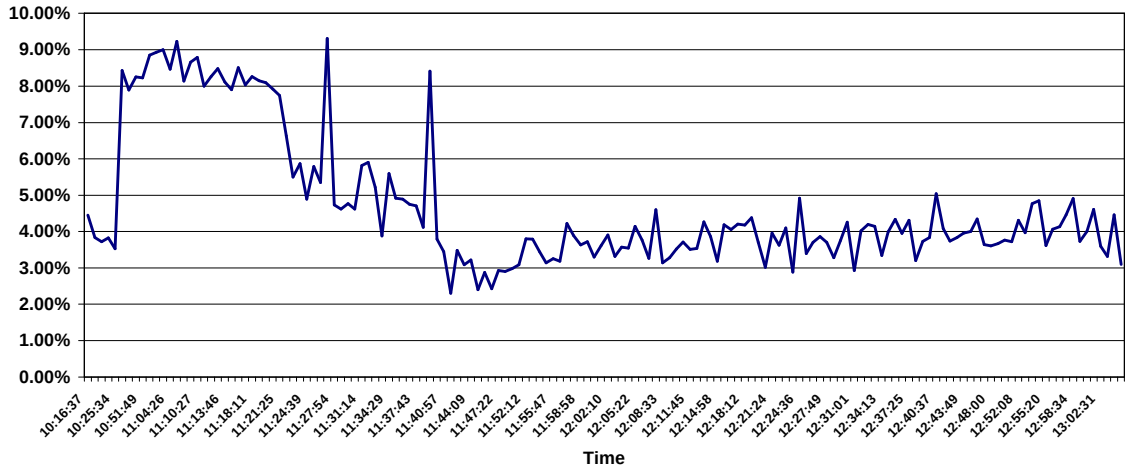

Figure 135. Estimate for Coefficient of Variation in CPR; Day #2

Figure 136 shows the variation in location of peak-firing pressure through the day. It varies from average values of 15 to 20 as timing is changed. It exhibits extremes from 11.25 degrees to 29.5 degrees, indicating wide variance in this quantity. The low of 11.25 degrees does correspond to the time soon after timing was advanced from 6 to 8 degrees.

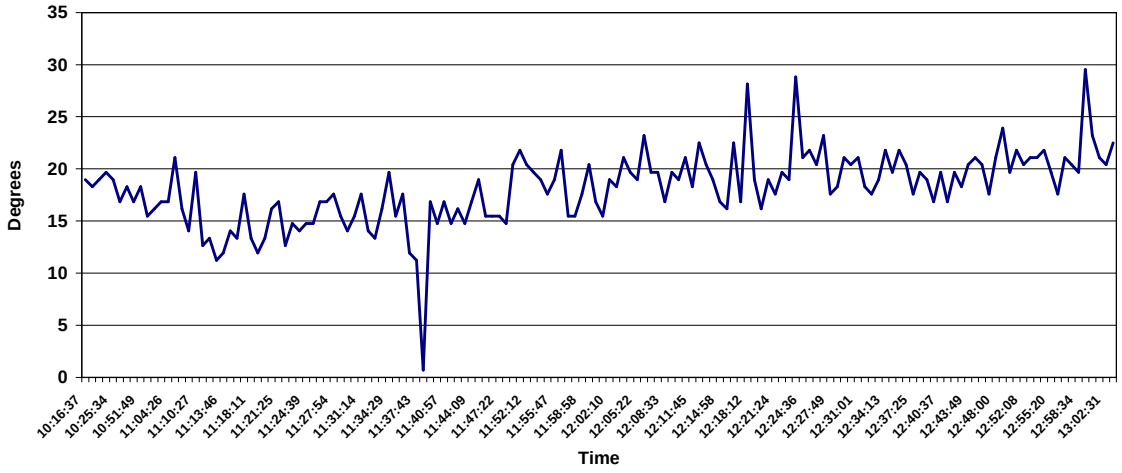

Figure 136. Average Location of Peak-Firing Pressure in Degrees after TDC; Day #2

Vibration data for day #2 is similar to day #1, and is not replotted.

Figure 137 shows a waterfall plot; as on day #1, the first four orders are noticeably higher than the remainder, with the second order dominating.

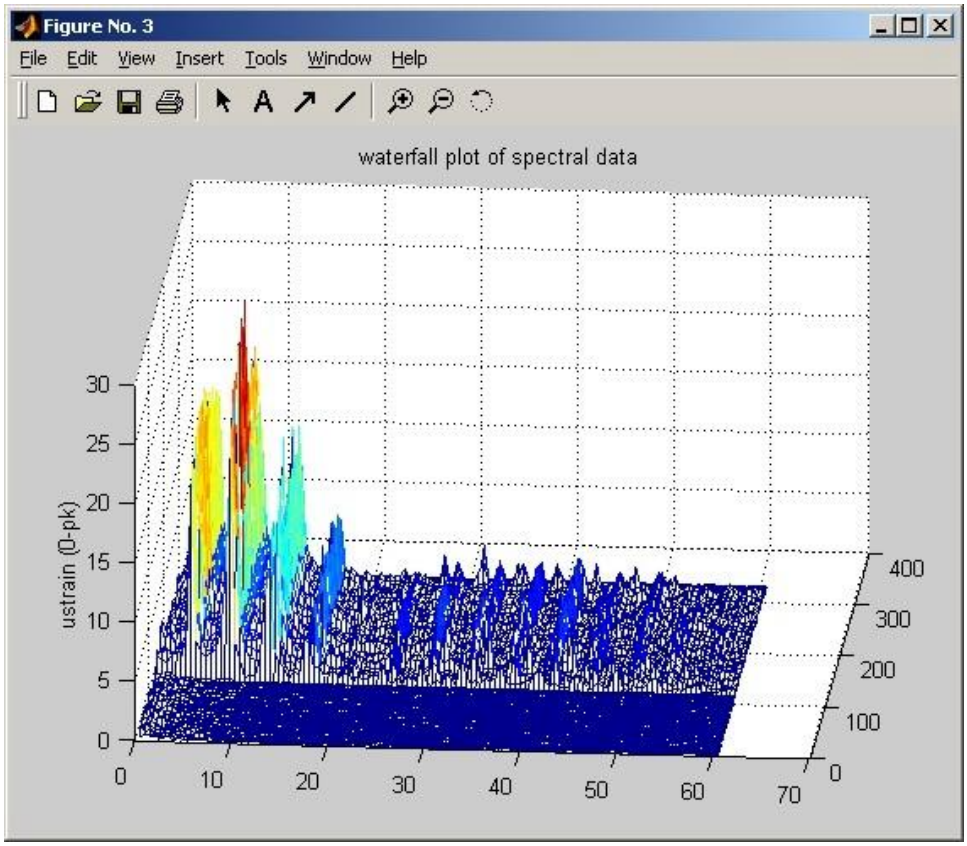

Figure 137. Waterfall Plot of Crankshaft Strain

Figure 138 shows that on day #2 once the unit starts, the strains rapidly set in at 118 microstrain as an average. When the timing is advanced to 8 degrees about 50 minutes after the start, the peak-to-peak microstrains increase to about 140 as a maximum, they start to fall rapidly back to 118 microstrain, after the timing is set back to 6 degrees. Reducing the torque to 94% is followed by a further reduction in peak-to-peak micro-strain to about 110 microstrain. Thus, the impact of timing advance, in addition to its influence on reducing heat rate, is to increase the dynamic load on the crankshaft with possible increase in damage accumulation rate.

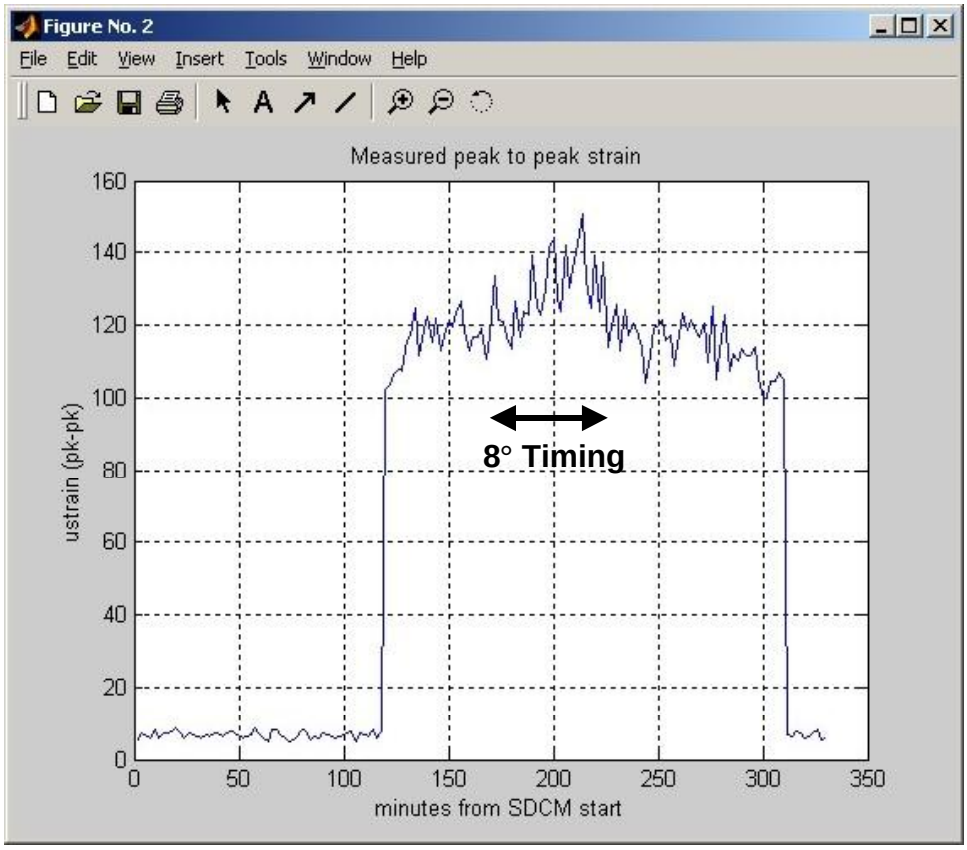

Figure 138. Crankshaft Peak-to-Peak Strain; Day #2

4.8.1 Supplementary Data

Figures 139 and 140 present normalized NOx concentration and global equivalence ratio. (Note this normalized NOx is not brake specific NOx.) In Figure 139, the equivalence ratio stays around 0.375, with small changes. It appears to respond to timing changes. The day #1 normalized NOx is in the range of 1.85; it follows some of the equivalence ratio change. Figure 140 for day #2 shows a lower equivalence ratio of about 0.36. The normalized NOx generally runs between 1.6 and 1.8, and follows the changes in equivalence ratio. Both equivalence ratio and NOx drop at the end of the day when torque was cut to 94%.

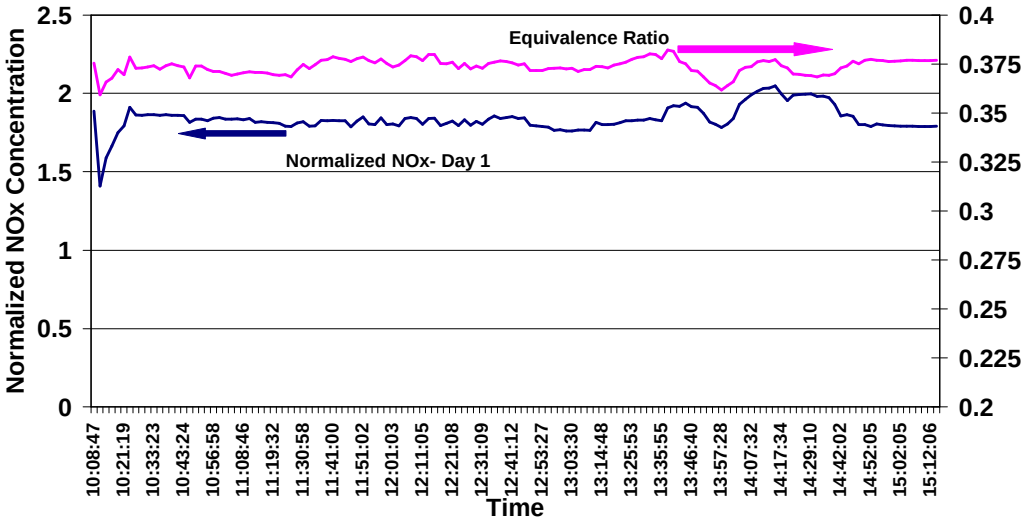

Figure 139. Normalized NOx Concentration and Equivalence Ratio; Day #1

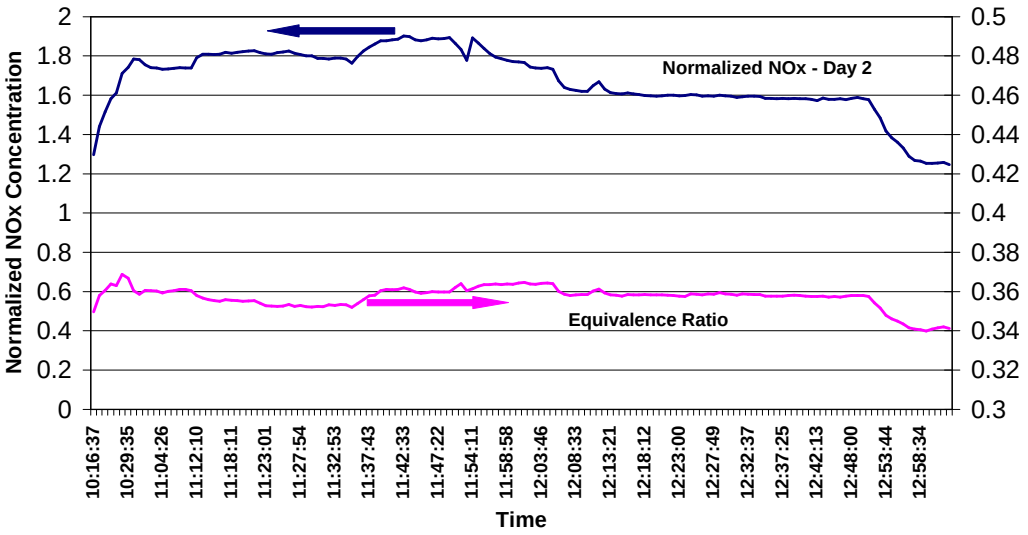

Figure 140. Normalized NOx Concentration and Equivalence Ratio; Day #2

Figure 141 provides some additional data — actually obtained during the first tests at El Paso Station 823. It compares normalized NOx concentration from the NGK sensor with a portable emissions analyzer (ECOMA+). The results track very closely (although they are not time coherent) giving confidence in the accuracy of the NGK sensor.

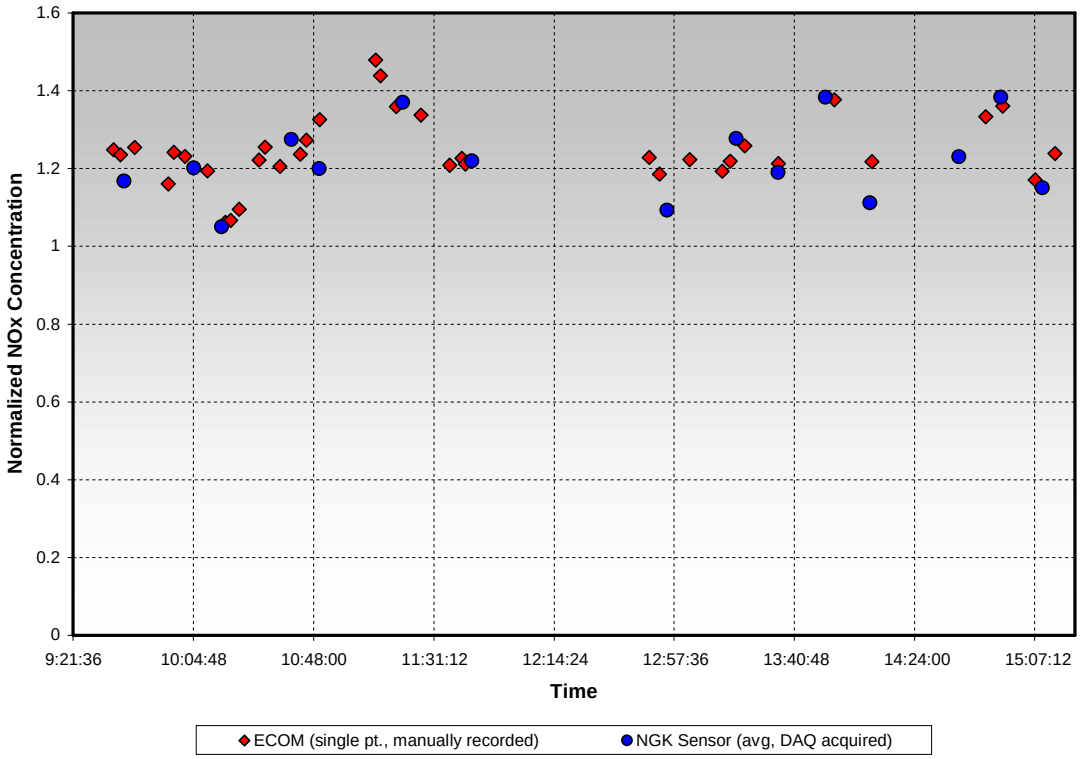

Figure 141. Comparison of ECOM and NGK Values for Normalized NOx

Table 4. Summary of Baseline Data; GMW10 - Unmodified

Day	Speed, RPM	Torque, %	Timing	AMP	AMT	Heat Rate BTU/HP-Hr.	Normalized NOx	System Thermal Efficiency, %
1	250	102%	6°	3.5" Hg	102°F	7477 ± 14	1.818 ± 0.019	27.31 ± 0.0005
2	250	102%	6°	3.5" Hg	96°F	7526 ± 11	1.660 ± 0.091	27.11 ± 0.04
2	250	101%	8°	3.5" Hg	96°F	7418 ± 16	1.825 ± 0.036	27.53 ± 0.06
2	250	96%	6°	3.5" Hg	95°F	7566 ± 35	1.395 ± 0.140	26.99 ± 0.13

Figure 142 presents the typical variation of air manifold pressure with crank angle. The peak-to-peak variation by almost 2 PSI is clearly higher than the average of about 1.5. The specific analysis in the lower part of the figure shows "action" to at least 67 orders.

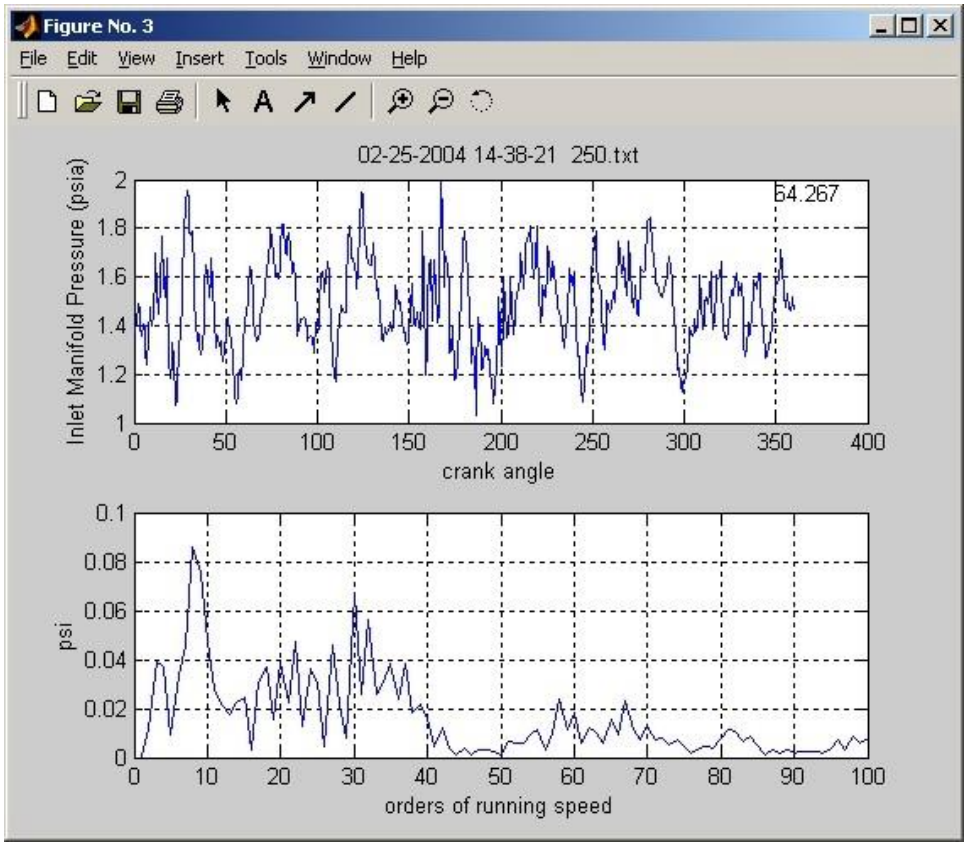

Figure 142. Inlet Manifold Pressure; Time Wave and Order Spectrum

Figure 143 presents results from the knock detector on day #2, after the knock detector had been moved to power cylinder #4L. The output increased substantially after timing was advanced to detonation. Both the audible and detected detonation went away after timing was retarded again to 6 degrees.

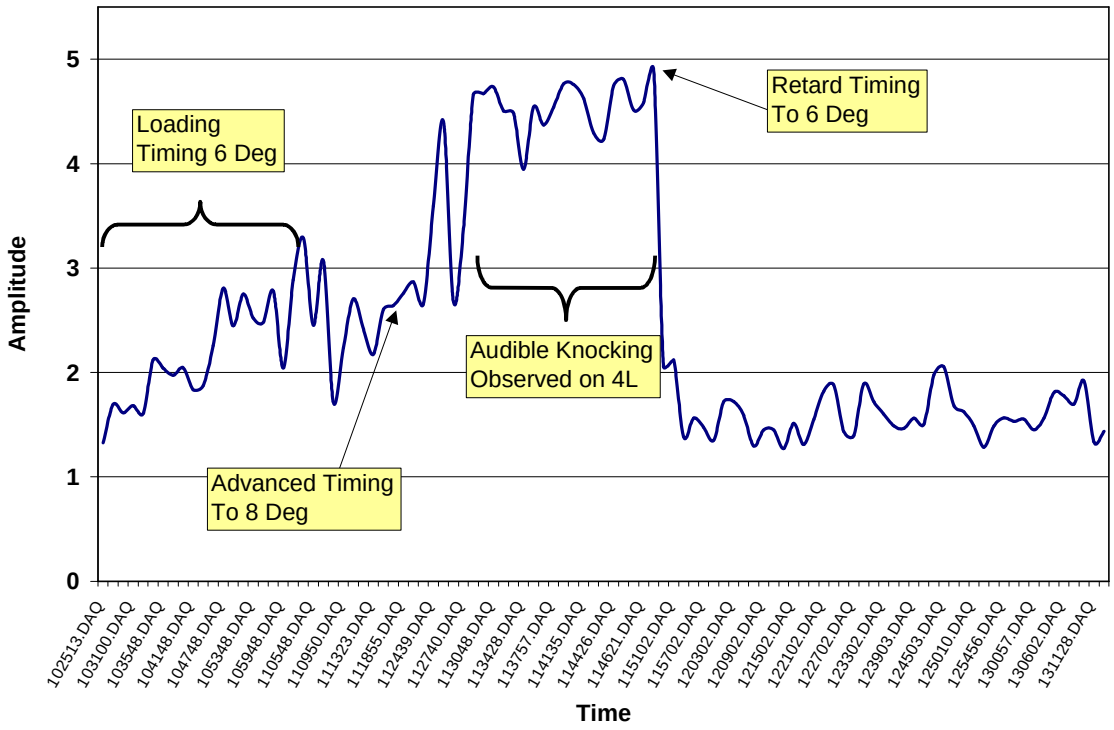

Figure 143. Knock Detector Output on Cylinder #4L

5. CONCLUSIONS

1. There is a need for low cost control of equivalence ratio in turbocharged engines. Use of a Universal Exhaust Gas Oxygen (UEGO) sensor, calibrated to read equivalence ratio, and integrated with a waste-gate controller to maintain an equivalence ratio set point, is a promising approach to be evaluated during the second test at El Paso Station 823 (Kinder, Louisiana).

2. Air imbalance which shows up as unequal compression pressure between cylinders causes a natural imbalance in peak-firing pressure. If compensated for by adjusting fuel to equalize peak-firing pressure, air imbalance will cause imbalance in equivalence ratio. Extra tasks have been proposed to evaluate manifold redesign as an approach to air balancing.

3. Air manifold pressure modulations have been documented at 20 to 25% of average. Exhaust manifold pressure modulations have been documented at 50% of average and above. There is a need to define the contribution of these variations to air imbalance and incorporate this knowledge in the manifold redesign.

4. Adjusting fuel to equalize the ratio of peak-firing pressure to compression pressure offers an alternative to directly equalizing peak-firing pressure, which should reduce the variation of equivalence ratio between cylinders. A balancing method entitled “Combustion Pressure Ratio” (CPR) has been invented. In conjunction with power cylinder pressure data, acquired and displayed during the tests, CPR balancing has proved quick, easy, and effective to implement.

5. Directly monitoring rod load will improve the accuracy and consistency of engine torque load assessment, and will lead to more effective adjustment of load steps to load of the engine up to, but not over 100%. Project data shows varying inaccuracies in torque inferred from normally available station data. The project

has provided test sites for the Rod Load Monitor (RLM), and RLM data has guided evolving changes to enhance telemetry data consistency and self-powering of this device.

6. The Strain Data Capture Module (SDCM) has indicated its sensitivity to changes in engine load. Timing advance has been shown to increase crankshaft strain on the GMW10, which must be considered in conjunction with the reduced heat rate and increase in NOx, which have also been observed as a result of timing advance.

7. The benefit of efforts to equalize combustion between cylinders by Peak-Firing Pressure (PFP) balancing, or by Combustion Pressure Ratio (CPR) balancing, are limited by the cycle-to-cycle combustion instability which shows up as high instantaneous spread. Further efforts to define the distribution of peak-firing pressure and its deviation from Gaussion are planned for the next series of tests at El Paso's Station 823.

8. Test data shows a reasonably consistent reduction in power transmission losses between power cylinders and compression cylinders following engine cold start, which correlates (at least circumstantially) with increasing oil temperature and associated viscosity reduction.

9. High-pressure fuel injection, coupled with a turbocharger and automatic balancing, allows very lean combustion. These technologies achieve a significant reduction in heat rate (to under 7000 BTU/HP-hr.) and NOx compared to a similar engine without these modifications. Further direct comparison testing on the same engine after modifications (including automated CPR balancing) is planned for work under Tasks 10 through 15.

10. System thermal efficiency (engine brake thermal efficiency * compressor mechanical efficiency * compressor thermal efficiency) of over 31% has been observed. This system thermal efficiency represents the conversion of fuel energy to useful compression of the transported gas.

11. Compressor thermal efficiencies ranging from 84 to 91% have been observed.

12. Project data has shown the consistency of a knock detector output with observations of audible knock. Further tests at El Paso's Station 823 will seek to define the warning provided by this knock detector before audible knock occurs.

6. REFERENCES

[1] Smalley, A.J., Mauney, D.A., and Ash, D.I., (1997) Final Report PR-15-9529, "Compressor Station Maintenance Cost Analysis," prepared for the Compressor Research Supervisory Committee of PRC *I*nternational, SwRI Project No. 04-7424.

[2] Harris, R.E., Edlund, C.E., Smalley, A.J., and Weilbacher, G., (2000) "Dynamic Crank Web Strain Measurements for Reciprocating Compressors," presented at the GMRC Gas Machinery Conference (GMC), Colorado Springs, Colorado.

[3] Wood, C.D. and Kubesh, J.K., (1995) "Evaluation of Emissions Control Technology for Reciprocating Integral Engine-Compressor Units," SwRI Report for Tenneco Gas Environmental and Technology Department.

[4] Smalley, A.J. "Topical Report: Misalignment and Temperature Measurements on a Fully Grouted Reciprocating Compressor," prepared for the Pipeline Research Committee of the American Gas Association, Project PR15-174, SwRI Project 04-7564, May 1985.

[5] Transmission, Book T-2: Compressor Station Operations, GEOP - Gas Engineering and Operating Practices, The American Gas Association Operating Section, Vol. II, A.G.A. Catalog No. XY0185.

[6] Harris, R.E. and Beeson, C.M. (1990) "Channel Resonance Correction for Improved Cylinder Performance and Diagnostic Analyses," Proceedings, PCRC Fifth Annual Reciprocating Machinery Conference, Nashville, Tennessee.

[7] Harris, R.E. and Edlund, C.E. (1998) "Performance Measurement of High Speed/High Ratio Reciprocating Compressors," presented at the GMRC Gas Machinery Conference (GMC), Denver, Colorado.

7. LIST OF ACRONYMS AND ABBREVIATIONS

A/F	Air/Fuel Ratio
AGA	American Gas Association
AMP	Air Manifold Pressure
BEI	Manufacturer's Trade Name
BHP	Brake Horsepower
BTDC	Before Top Dead Center
BTU	British Thermal Unit
CES	Cooper Energy Services
CO	Carbon Monoxide
COV	Coefficient of Variance
CPR	Compression Pressure Ratio
DAS	Data Acquisition System
DOE	U.S. Department of Energy
ECOM A+	An Emissions Analyzer Model
EQ	Equivalence Ratio
FHP	Fuel Header Pressure
FIFO	First In, First Out
GMC	Gas Machinery Conference
GMRC	Gas Machinery Research Council
GMW10	Pipeline Engine Model
HBA-6	Clark Engine Model
HBA-6T	Clark Engine Model
HBA8	Clark Engine Model
HP	Horsepower
HPFI^{TM}	Enginuity's High Pressure Fuel Injection System
I/P	Current-to-Pressure Converter
IAC	Industry Advisory Committee
IMEP	Indicated Mean Effective Pressure
IRV	Instantaneous Rotational Velocity
LBSI	Lean-Burn Spark-Ignited
LHV	Lower Heating Value
mAmp	Milliamp
MMSCFD	Million of Standard Cubic Feet Per Day
MW	Megawatts
NGK	Manufacturer's Trade Name
NO	Nitric Oxide
NO_2	Nitrous Oxide
NOx	Oxides of Nitrogen
O_2	Oxygen Molecule
OEM	Original Equipment Manufacturer
PCB	Manufacturer's Trade Name

LIST OF ACRONYMS AND ABBREVIATIONS *(CONTINUED)*

PFP	Peak-Firing Pressure
PID	Proportional-Integral-Differential
PPM	Parts Per Million
PSI	Pounds Per Square Inch
PSIA	Lb./Sq. Inch Absolute
PV	Pressure-Volume
RLM	Rod Load Monitor
RPM	Revolutions Per Minute
SCF	Standard Cubic Feet
SDCM	Strain Data Capture Module
Sdev	Standard Deviation
SwRI®	Southwest Research Institute®
TDC	Top Dead Center
TGP	Tennessee Gas Pipeline
UEGO	Universal Exhaust Gas Oxygen